Technische Universiteit Delft

Flapping-wing aerodynamics study on the wake of DelFly II

by means of Robotic Volumetric Particle Tracking Velocimetry

Blanca Martínez Gallar

TU Delft

Flapping-wing aerodynamics study on the wake of DelFly II

by means of Robotic Volumetric Particle Tracking Velocimetry

by

Blanca Martínez Gallar

to obtain the degree of Master of Science
at the Delft University of Technology,
to be defended publicly on Friday May 1, 2019 at 14:00.

Student number:	4630572	
Project duration:	September 18, 2017 – May 01, 2019	
Thesis committee:	Dr. ir. B.W. van Oudheusden,	TU Delft, supervisor and chair of committee
	Dr. A. Sciacchitano,	TU Delft, supervisor
	Ir. C. de Wagter,	TU Delft, committee member
	Ir. C. Jux,	TU Delft, committee member

An electronic version of this thesis is available at http://repository.tudelft.nl/.

TU Delft

People, we have perfectly ordinary plumbing.
Steven Vogel

Learn to sit back and observe. Not everything needs a reaction.
Unknown

If you want to know the truth of who you are, walk until not a person knows your name. [...] A long stretch of road will teach you more about yourself than a hundred years of quiet introspection.
Patrick Rothfuss

When everything seems to be going against you, remember that the airplane takes off against the wind, not with it.
Henry Ford

If you can't explain it simply, you don't understand it well enough.
Albert Einstein

Preface

The moment has finally come. After approximately one and a half years of work, passion and struggle; I have finished my master thesis. As a consequence, I also finish a very important chapter of my life. I have been a student for as long as I can remember and I cannot dare but say that it has been a long and beautiful ride. This, of course, does not mean that I am going to stop learning, not a chance! The work of an engineer comes with challenges and regular re-innovation of one's self knowledge. And I hope that, during the next chapter that is about to start, I will bring all the motivation and encouragement to "*challenge the future*" as I have lived during my years at TU Delft.

The two people I need to thank the most during this project are Bas and Andrea. As my supervisors, they have helped me during the complete process. From day one, I have learned a lot at their side. Our interesting discussions have been a key aspect for the development of my work. I also had the privilege to go to a conference with the two of them and learn (even) more about flow visualization techniques. I am extremely grateful for their support even when I decided to join Airbus and move back to Spain. This project has been a collaboration in between the Aerodynamics department and the MAVlab group of TU Delft. Without all the care and help Matej, Diana and Aadi this project would not have been possible. As part for the team to make this possible, I want to recollect the help of Peter, Frits, Nico, Dennis and Colette.

Delft would not have been the same without the hours of company of the inhabitants of the basement. We all shares a common objective and we help each other during the way. I have to especially give thanks to Mitro for managing to keep a cheerful spark in the room in the coldest days ever in the wind tunnel and for his awesome photographing skills. And also to Edo who has been a hidden tutor and a great friend all at the same time. All the laughs spent with Arun is something that I will never forget, even if has chosen the dark path of aerodynamics, CFD. Thanks also to all the rest of the team with whom I shared many many good moments: Jaime, Giggi, Corrado, Javi, Jordi, Sumedh, Derek and Ventsilav. During my master I also had the pleasure to hang out with Rober, Dorian, Jorge and Stelios. I wish you the best of luck finishing your respective missions.

Back at home, I had the amazing encouragement of Belén. Even if she does not understand what I was doing she always asked me about my work and spent with me a lot of hours in the library. My family of course has been an incredible pillar all this time. My always loving mother Blanca, my energetic father Jose Manuel and my dear little (not so little anymore) brother Jorge have been there for me all the time, no matter what. I know sometimes I have not been the most enjoyable person to be around and yet they have been by my side every step of the way.

Last but not least, I cannot end this section without mentioning a very especial man in my life. Oscar you are a source of joy and peace, no matter if we are close to each other or living in different countries. You remind me every day of the important things in my life and give me confidence to accept all the challenges that lie ahead.

Blanca Martínez Gallar
Delft, February 2019

Abstract

The aim of this investigation is to provide an experimental volumetric visualization of the near wake topology of the vortex structures generated by a flapping-wing Micro Air Vehicle (MAV) by means of large-scale Robotic PIV. This novel technique implements coaxial illumination and imaging in combination with the use of Helium Filled Soap Bubbles (HFSB) as tracing particles to achieve large measurement volumes of the order of 10 liters. Information of different phases throughout the flapping cycle is obtained by means of a phase-locked averaging procedure. The MAV used for this study is called DelFly II. It is a platform composed a two pairs of wings attached to a slip body with horizontal and vertical tailplanes for stability and maneuverability. Measurements are performed at regular free-flight scenarios within the DelFly flying envelope. The configurations selected have different reduces frequencies which allows to analyze the effect of this important parameter. Same configurations are also measured with and without the presence of the tails to see their influence of the wake topology. In addition, experiments in both tethered and free-flight conditions have been performed, yielding an unprecedented comparison between the aerodynamics of the two conditions.

The significance of the proposed project lies on the ability of assess the complete three-dimensional wake of the DelFly II. This is the first experimental study performed that can achieve such measuring volumes for any flapping-wing platform, to the knowledge of the present author. Another major benefit of this study is the use of standard flight configuration to observe the wake structures when the MAV is able to sustain level flight. Therefore, the proposed work is expected to be a relevant addition to the understanding of the flapping-wing mechanism.

Contents

List of Figures

List of Tables

Nomenclature

α_b	Angle of attack of the DelFly body	$[^o]$
β	Camera aperture	$[^o]$
Δt	Period between successive pairs of images	$[s]$
ΔX	Particle distance in X-direction	$[px]$
ΔY	Particle distance in Y-direction	$[px]$
ϵ_u	Uncertainty of velocity	$[-]$
Φ	Stroke amplitude	$[^o]$
ϕ	Stroke angle	$[^o]$
$\dot{\phi}$	Angular velocity	$[rad/s]$
λ	Characteristic wavelength of laser light	$[nm]$
μ	Dynamic viscosity	$[kg\ m^{-1}\ s^{-1}]$
ρ	Density	$[kg\ m^{-3}]$
σ_u	Standard deviation of velocity	$[-]$
τ_R	Response time of a particle	$[s]$
Ω	Antisymmetric part of Q-criterion	$[s^{-2}]$
ω	Angular frequency	$[rad/s]$
ω_x	Vorticity component in X-direction	$[rad/s]$
ω_y	Vorticity component in Y-direction	$[rad/s]$
ω_z	Vorticity component in Z-direction	$[rad/s]$
A	Cross-sectional area of the seeding rake	$[m^2]$
$A*$	Dimensionless stroke amplitude	$[-]$
b	Span of a single wing	$[m]$
C	Particle concentration	$[bubbles/cm^3]$
C_L	Lift coefficient	$[-]$
c	Mean chord of a flapping wing	$[m]$
dt	Pulse separation times	$[s]$
d_p	Diameter of the particle	$[m]$
d_{px}	Distance travelled by particle	$[px]$
f	Focal length	$[mm]$
f	Flapping frequency	$[Hz]$
f_{flap}	Flapping frequency	$[Hz]$
$f_\#$	Lens relative aperture	$[-]$
I_{min}	Minimum light intensity	$[counts]$
k	Reduced frequency	$[-]$
L_{ref}	Characteristic length	$[m]$
M_0	Magnification factor	$[-]$
N	Number of samples	$[-]$
$\dot{N}$	Production rate of the bubbles	$[bubbles/s]$
ppp	Particles per pixel	$[-]$
Q	Q-criterion	$[s^{-2}]$

R	Radius of gyration of a wing	$[m]$
Re	Reynolds number	$[-]$
Ro	Rossby number	$[-]$
S	Symmetric part of Q-criterion	$[s^{-2}]$
Str	Strouhal number	$[-]$
U_∞	Freestream velocity	$[m/s]$
$U_{b_{MAX}}$	Maximum velocity of jet	$[m/s]$
U_{ref}	Characteristic velocity	$[m/s]$
U_s	Slip velocity	$[m/s]$
u	Velocity component in X direction	$[m/s]$
Vz_{rot}	Rotational velocity	$[m/s]$
v	Mean lateral velocity	$[m/s]$
v	Velocity component in Y direction	$[m/s]$
v_{He}	Volume rates of helium	$[l/s]$
XYZ_{tool}	Tool reference frame	$[mm]$
XYZ_{camera}	Camera reference frame	$[mm]$
y_b	Y axis in the body coordinate system of the DelFly	$[mm]$
z_0	Minimum depth measured	$[mm]$
z_{MAX}	Maximum depth measured	$[mm]$

1

Introduction

An increasing interest in the development of Micro Air Vehicles (MAVs) has been seen in recent years due to the wide range of missions where they can be employed: from searching and rescuing activities to security and surveillance applications. These MAVs typically fly at low speeds or even in hovering conditions, but high maneuverability and flight efficiency is desirable for wind gusts rejection and increased flight endurance, respectively. Different classes of MAVs can be distinguished: fixed wings, rotatory wings and flapping wings [57]. Well-established aircraft design concepts apply to fixed and rotatory wing configurations, but these vehicle types suffer a detrimental effect on performance when scaled down in size (see figure 1.1). On the other hand, natural fliers, serving as an inspiration to flapping-wing designs, have shown extraordinary flight capabilities at low Reynolds numbers [16, 58] . Thanks to new flow visualizations techniques that have become available (Particle Image Velocimetry in particular), the characteristics of the flow of flapping wings has been better understood, identifying several unsteady mechanisms [66, 78] . These unsteady mechanisms help enhancing the lift production like for example clap-and-peel [4]. The understanding of the flow characteristics of flapping wings and their relation to force generation has been investigated extensively on both natural fliers and Flapping-Wing MAVs (FWMAVs). Nevertheless, there are still no general models or theories that completely describe the aerodynamics of flapping wings.

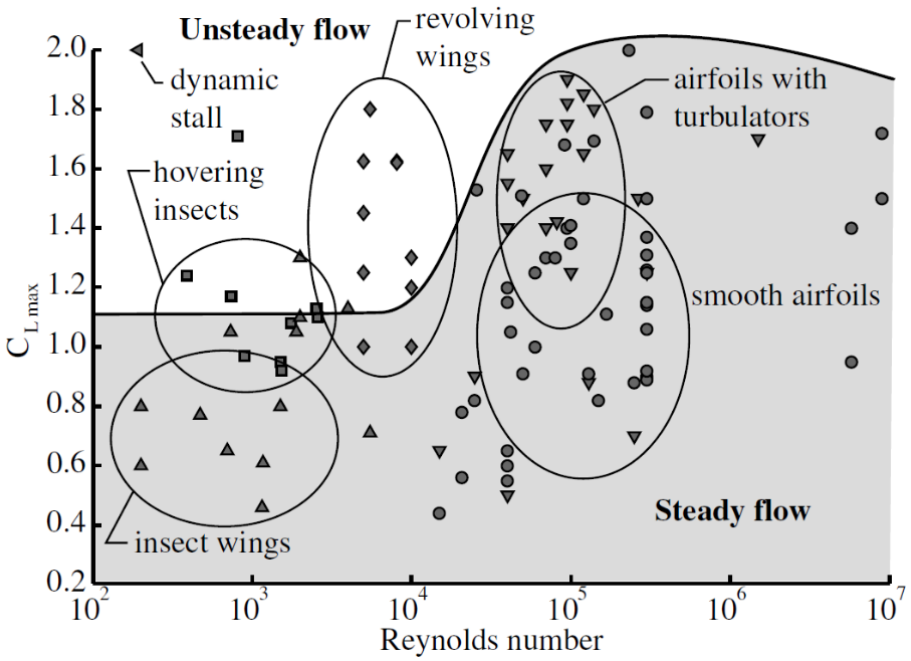

Figure 1.1: Maximum lift coefficient vs. Reynolds number for different flying mechanisms. [62]

The main objective of the project is to acquire a deeper fundamental understanding of aerodynamic behavior of the flapping-wing mechanism by performing quantitative measurements on the wake of a FWMAV. The specific flapping-wing MAV investigated in this study is the DelFly II, which has been design by TU Delft [21]. The main features of this MAV can be seen in figure 1.2. The DelFly consist on a slim fuselage where two pairs of wings are attached as well as a vertical and horizontal tail for stability and maneuverability. For further information about the DelFly characteristics, please refer to section 2.3.

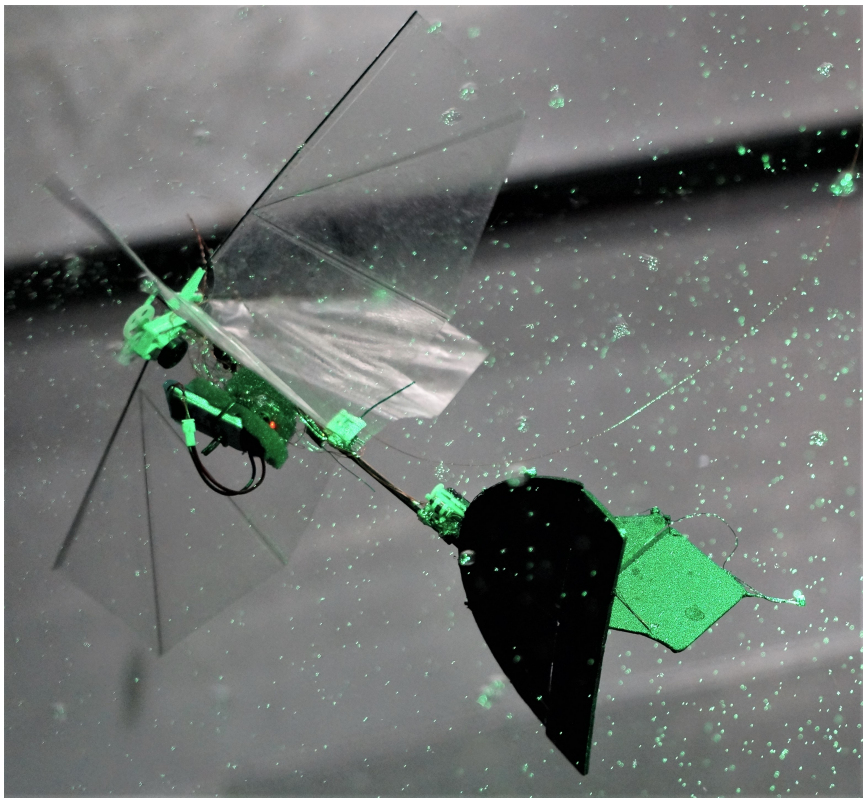

Figure 1.2: DelFly II in free-flight conditions

Nowadays experiments are the most precise way to obtain information about the behaviour of the flow around flapping wings. The PIV research done in the last years on the DelFly II has always been limited to planar and stereo PIV [60], so information is restricted to planes and special effort is required to reconstruct a three-dimensional flow representation. With the information from 2D measurements, the basic evolution of the vortices generated during a flapping cycle can be understood like in the case of figure 1.3 were the leading and trailing edge vortices can be clearly seen.

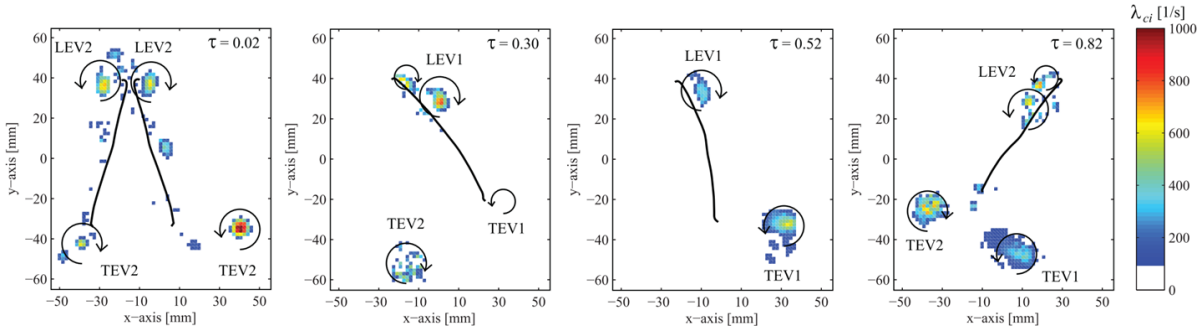

Figure 1.3: Swirling strength at various moments during the flap cycle, showing leading edge vortices (LEV) and trailing edge vortices (TEV) during out-stroke (1) and during in-stroke (2) of the wing positioned on the left at the first time instant, figure adapted from Groen et al. [38]

Nevertheless, due to the highly complex three-dimensional behaviour of flapping wings, a significant part of the mechanism cannot be analyzed. Several studies have attempted to reconstruct the three-dimensional wake from measurements performed on a limited space. One option for the reconstruction is to assume the the wake is frozen, called Taylor's hypothesis. The assumption implies that the vortex structures shed by the flapping mechanism convect with a velocity equal to the freestream velocity. In this way, the evolution of the vortex structures can be represented. However only the information of structures seen by in the planar measurements is used so no other structures in the out of plane direction can be found. This approach has been followed by Percin et al. [60], as shown in figure 2.12. However it has been shown that the Taylor's hypothesis is not for the wake of flapping wings as the induced velocities generated by the vortex structures themselves have a great influence on the evolution of such structures along time and space [11].

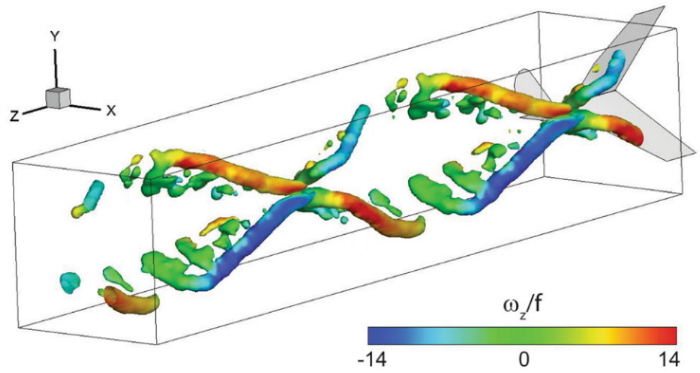

Figure 1.4: Perspective view of the wake structures visualized by isosurfaces of $Q/f^2 = 10$ and colored by ω_x/f for two periods of the flapping motion (flow is the positive z-direction) for the case of $k = 0.47$ ($U_\infty = 3$ m/s and $f = 5.7$ Hz) [60].

Another approach that was successfully implemented by Henningsson et al. is the use of using MLOS-MART (multiplicative line of sight—multiplicative algebraic reconstruction technique) [40]. This method allows to extent the information volume from $200 \times 240 \times 50\ mm^3$ (streamwise, spanwise, vertical) to $200 \times 240 \times 58\ mm^3$. This increase in the volume cover is still insufficient. To characterize the near-wake flow topology in a more appropriate and direct way, a volumetric flow measurement is required of the complete wake.

Having into account the growing interest in flapping wings, the proposed research objective is:

"*Investigate the flow behaviour in regular flight scenarios by means of volumetric flow measurements of a Flapping-Wing Micro Air Vehicle along its complete wake in a wind tunnel environment*"

In order to tackle this project, a literature study has been performed to explore the existing knowledge on the subject of flapping wings and present an overview of noteworthy studies related to flapping wing aerodynamics. Both a general perspective of the topic and a more detailed explanation of the FW-MAV used are exposed in chapter 2. The methodology to be employed to perform the volumetric flow measurements is called Robotic Volumetric Velocimetry. The main advantage of this innovative measuring technique is the ability of computing the three components of velocity of the particles embedded in the flow in a volume of dimensions that are comparable to the dimensions of the DelFly II. The main aspects of PIV and an extensive description of the methodology to be used in this study will be explained in chapter 3.

To fulfill the proposed research objective successfully, two experimental campaigns are arranged and carried out. The set-up of both campaigns are presented in chapter 4. Afterwards, chapter 5 walks through the complete process to follow from the data collected by the cameras and the final velocity field on the complete volume. However, before any experimental campaigns could be accomplished, a test to prove the capacity of the large-scale 3D PTV measurement technique to successfully capture the studied unsteady flow is required. The results of such preliminary tests are exposed in chapter 6. Once the feasibility of the experiments is confirmed, the experimental campaigns took place. The first campaign related to the measurement of the wake of the DelFly in tethered conditions. As the

DelFly was attached to a support structure, experiments with and without tail were achieved. The DelFly is placed in the wind tunnel stream resembling regular flight conditions of the FWMAV. This is accomplished by setting three parameters: free-stream velocity, angle of attack of the body of the DelFly and the flapping frequency of its wings. Three different configurations are tested and presented in chapter 7. On the second experimental campaign, the DelFly is set to fly within the wind tunnel stream, aiming to position itself, by means of an optical control system, at a certain location so measurements can be taken. These second campaign allows to observe the difference between tethered and free-flight conditions. Finally in chapter 8, conclusions of the obtained results are drawn and recommendations are provided if this line of investigation should be further evaluated.

2

Literature review

2.1. Flapping wing aerodynamics

The main characteristics of flapping wing aerodynamics will be discussed to have an overview of the main phenomena that occur during a flapping cycle. The flapping wings of the DelFly follow the same principles for force generation, specifically lift and thrust, as flapping wing insects. Research related to insect flight have been performed since many years, however the understanding of the basic aerodynamic behaviour that comes with it has only been achieved in the last decades. The second part of this section discusses specific terms and definitions commonly used when talking about flapping wings. A summary of the specific aerodynamic phenomena that are observed in the unsteady flow generated by flapping wings will follow in section 2.1.3. And to finalize this chapter, the most important parameters that affect the flapping wings will be described in section 2.1.4.

2.1.1. Introduction to flapping flight

The wonders of the flow dynamics of flapping wings have been subject of research pursued from both a biological and an engineering perspective. The interest from an engineering point of view is motivated by the involvement of flapping wings in the development of Micro Air Vehicles (MAVs) in recent years, using bio-inspired designs. In today's society, there is a growing demand for autonomous unmanned aerial vehicles. This kind of vehicles has a miniature size and they are able to fly at significant low velocities which raises the question if the same procedures and theories applied to the design and analysis of more conventional aircraft of larger dimensions can be applied. The interest in this kind of devices is due to the great range of different activities where they can be employed. For example, MAVs can be used as an identification platform for search and rescue missions as well as exploration of areas of difficult access or even for security applications. These MAVs should be able to fly at low speeds or even in hovering conditions, they should also have high maneuverability and of course they should be efficient. In this range of capabilities different classes of MAVs can be found depending on the force generation mechanism: fixed wings, rotatory wings and flapping wings [57]. Fixed and rotatory wings concepts have been developed greatly, as already well-established aircraft design theories can be applied to these kind of models. However, it has been seen that these design suffer a detrimental effect of their aerodynamic performance when the models are scaled down [7]. On the other hand, bio-inspired flapping wing designs have shown extraordinary flight capabilities at low Reynolds numbers.

The French entomologist Antoine Magnan published in 1934 his book titled 'Le Vol des Insectes' [53]. In this publication he stated that when the conventional laws related to the aerodynamics of fixed-wings were applied to flapping wings, there was no explanation about how insects were able to fly.This shows the lack of understanding of the flapping wing mechanism not far in the past. In order to tackle this problem, different approaches were followed. Flapping wings aerodynamics is often related to revolving propeller blades as both generate lift by pushing air downwards. Successful theories for the far-field wake of flapping wings were elaborated based on the extensive work already available on rotor aerodynamics [31, 65]. However researches, like those of Sanjay Sane and Nathaniel Jacobson [67], have not been able yet to derive near-field theories in this subject that can be applied to different wing shapes, flight conditions, etc. Thanks to new flow visualizations techniques that have become

available (Particle Image Velocimetry in particular), the characteristics of the flow of flapping wings can be investigated in much more detail, supporting the identification of several unsteady flow mechanisms [66, 78]. The improved understanding of the flow characteristics of flapping wings and their relation to force generation has been investigated extensively on both natural fliers and flapping mechanisms. This is possible due to the opportunity with these new technologies to measure the instantaneous flow field around the moving wings combined with the increase in computational power which enables to make more detailed and more reliable numerical flow simulations. Nevertheless, there are still no general models or theories that completely describe the aerodynamics of flapping wings.

2.1.2. Terms and definitions

As a first introduction the main features of flapping wing motion are presented. The wings have several degrees of freedom. It is usually considered that the wings are constricted to move in a plane, referred to as the stroke plane. The stroke plane, for simplicity, is shown as perpendicular to the body but it could also be placed at an angle. For the case of the DelFly the stroke plane is indeed perpendicular to the direction of the body so this angle will not be taken into account in this explanation.The wings move forwards and backwards on this stroke plane. This motion is called **sweep**. When the ventral side of the wing is the one leading the motion that it is called the instroke while when the dorsal fin is leading it is called the downstroke (see figure 2.1). When talking about the DelFly, the instroke is equal to the part of the cycle when the two wings on each side (see figure 1.2) are coming towards each other and the outstroke starts when they move apart. The stroke angle (ϕ) is defined as the instantaneous angle between the leading edge of the wing and the y axis in the body coordinate system (y_b), whereas the stroke amplitude (Φ), is the total angular displacement of the wing in the stroke plane.

The wings can also rotate with respect to their leading, which is called **pitch**. Pitching motion is most prominent during the change from one stroke to another in order to have always a positive angle of attack of the wing surface with respect to the relative flow motion. When the pitch occurs in the transitions from the upstroke to the downstroke, the motion is called pronation while viceversa is called supination. The additional motion of the wings in the direction normal to the stroke plane is known as **heaving**. The leading edge of the wings usually form an eight shape along a flapping cycle due to the combination of the sweeping and heaving motions. This has a significant effect on the force generation of flapping wings [68] .

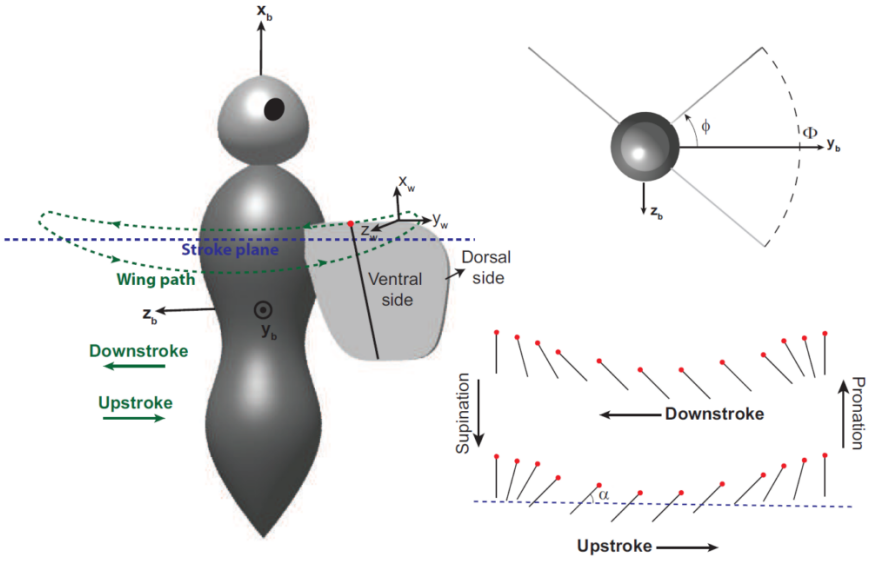

Figure 2.1: Schematic diagrams of body and wing coordinate systems and kinematics of flapping wing motion depicted on a generic flapping wing entity [60]

Looking now into non-dimensional analysis of the flapping motion, three parameters need to be defined as they are relevant to the flapping wing behaviour. The first well know parameter is the **Reynolds number**. The Reynolds number is a dimensionless number that indicates the ratio between inertial and

viscous forces, which means that it determines the importance of one effect with respect to the other. The Reynolds number is usually defined as follows:

$$Re = \frac{\rho L_{ref} U_{ref}}{\mu} \tag{2.1}$$

The density and dynamic viscosity of the fluid (ρ and μ) correspond to air. The characteristic length (L_{ref}), as in the case of fixed wing, is defined as the mean chord of the flapping wing ($\bar{c}$). The characteristic velocity (U_{ref}) of the flow is not straightforward to define in the case of flapping wing flight. Depending on the flight conditions to be studied, a certain reference velocity can be more suitable than another. For example in forward flight it is reasonable to use the forward flight speed as reference. However, for slow forward flight or hovering conditions it can be more appropriate to use the mean wing (tip) velocity instead, as the flapping wing motion can generate higher speeds than the forward flight velocity.

Another important nondimensional parameter for flapping wing flight is the **Strouhal number** that is the ratio of the two inertia forces, the unsteady and the steady components. This leads to the ration between the flapping velocity and the forward flight velocity as seen in equation 2.2. This parameter is relevant when looking at the vortex shedding and vortex dynamics of the flow. The Strouhal number is a function of the flapping frequency (f), the stroke amplitude (Φ), the span of a single wing (b) and the forward velocity of the body (U_∞).

$$Str = \frac{f \Phi b}{U_\infty} \tag{2.2}$$

The final important dimensionless parameter to be considered is the **reduced frequency**, that gives a measure of the unsteadiness motion of a flapping wing. The reference length is also defined as the chord of the wing but the reference velocity considered depends again on the flight conditions to be analyzed. Either the forward flight velocity ($U_{ref} = U_\infty$) or the mean wing tip speed ($U_{ref} = 2\Phi f b$) can be used. If we consider forward flight conditions, the reduced frequency is defined as:

$$k = \frac{\pi f \bar{c}}{U_\infty} \tag{2.3}$$

2.1.3. Important phenomena

Different unsteady mechanisms are present in flapping wing flight. Natural fliers take advantage of all these different mechanisms to achieve high performance efficiency. The main mechanisms will be discussed in this section. The five mechanisms listed can be classified in two categories. The first three mechanisms relate to circulatory forces so that these mechanisms influence the circulation along the wings. The last two mechanisms correspond to non-circulatory forces that are generated primarily due to the momentum transfer from the fluid to the wings.

Leading edge vortex (delayed stall)

Flow separation along a wing is generally undesired in fixed wing configurations as it deteriorates the wing performance (lower lift, higher drag). However in the case of flapping wings it leads to an enhancement of force generation. For a thin airfoil, when flow detaches at the leading edge, there is still a period of time duting which the leading edge vortex generated by flow separation reattaches before the leading edge so that Kutta condition is still fulfilled. This leads to an increase of the lift force produced as the leading edge vortex creates a low pressure region on the upper surface of the wing. This process is called ”delayed stall”.

As long as there is a stable attached LEV, this mechanism effectively increases the circulation around the wing and therefore also the forces, lift and drag, that are generated. Nevertheless, at a certain limit the LEV size is so large that reattachment is no longer attainable in 2D flow. When looking at a 3D flow, in several studies a prolonged attachment of the LEV during the sweeping motion of the wings has been seen [6, 28, 32] . This leads to a certain accordance in the presence of at attached 3D structure, even if the mechanism that stabilizes it is not yet fully understood. An sketch for different insect wings was depicted by Bomphrey et al. in 2005 [8], as can be seen in figure 2.2. The shape of the LEV changes significantly depending on the wing shape of the insect, making the behaviour harder to characterize.

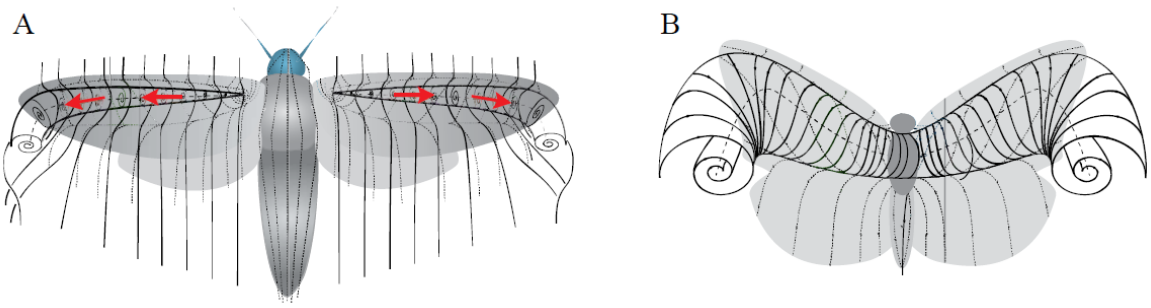

Figure 2.2: Two LEV structures. (A) Structure described by Ellington and van den Berg for a hawkmoth [23, 32], where the LEV is a conical spiral with spanwise flow in the vortex core. (B) Structure found by Srygley and Thomas for a butterfly [80], where a single LEV is extending across the thorax and no significant spanwise flow is present. Adapted from Bomphrey et al. [8]

Rotational forces

Rotational forces are present mainly during the stroke reversal of the wings, when pronation and supination happen. When a wing starts rotating, additional circulation on the wing must be generated to fulfill the Kutta condition. Depending on the direction of the rotation the extra circulation will be added or subtracted to the already existing circulation. The instant at which the rotation happens and the direction of the motion play a key role on the generation of forces. The rotation of the wing can be advanced, to increase the instantaneous angle of attack, or it can be delayed, producing a negative lift during a short time. Experiments in a robotic fly apparatus [29] show the comparison between the translational and rotational forces along a flapping cycle as seen in figure 2.3.

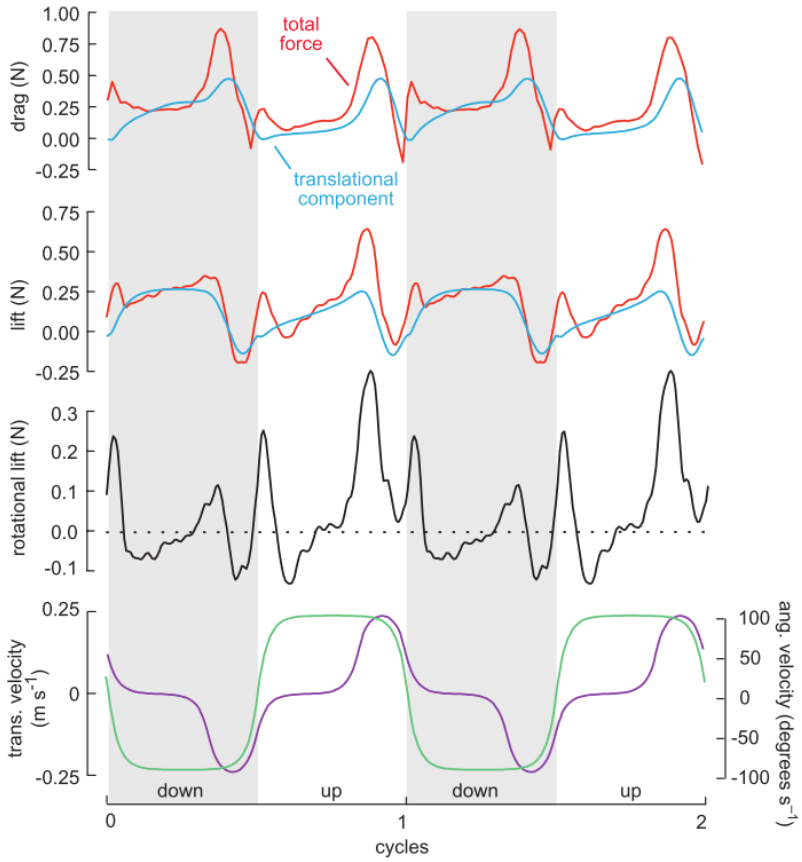

Figure 2.3: Time history of lift and drag forces (measured forces are plotted in red, and forces predicted from translation force coefficients are plotted in blue) in the first two plots. Difference between measured and estimated translational values of lift is shown in the third plot as rotational lift. Last plot shows the translational (green) and rotational (purple) velocities of the wing [29]

The final forces generated along the cycle were also plotted in this study (figure 2.4) to show the evolution of the magnitude and direction of the lift force. This study analyzed advanced, symmetrical and delayed rotation and it seems that the wing rotation is so important that a phase advance of 8 % from delayed rotation to symmetrical can cause an increase in the mean lift generated of approximately 67%. This is important when greater forces are needed than on regular forward flight, such as during maneuvers [29] or when carrying a payload similar to the weight of the body itself [54].

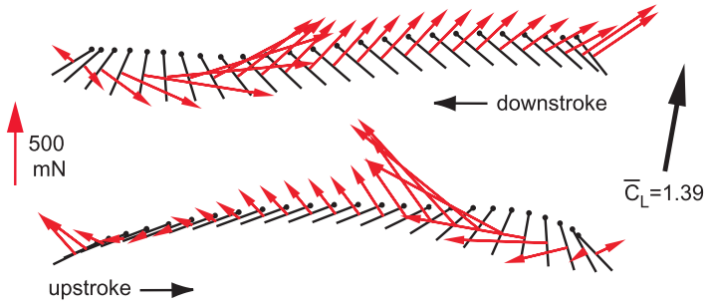

Figure 2.4: Diagram of wing motion indicating magnitude and orientation of force vectors generated throughout the stroke [29]

Clap-and-fling motion

Clap-and-fling mechanism relates to the interaction between the flapping wings. This phenomenon occurs when the wings are closed to each other, during the end of the upstroke, the pronation and the beginning of the subsequent downstroke. When the wings are coming towards each other (A), a v-shaped gap appears that during what is called the clap phase (B). Then when the leading edges are closed together the wing rotates and the trailing edge of the wings come together as well (C). During the fling phase, the leading edges start to move away from each other (D) and the flapping cycle continues (E and F). A summary of the process can be seen in figure 2.5.

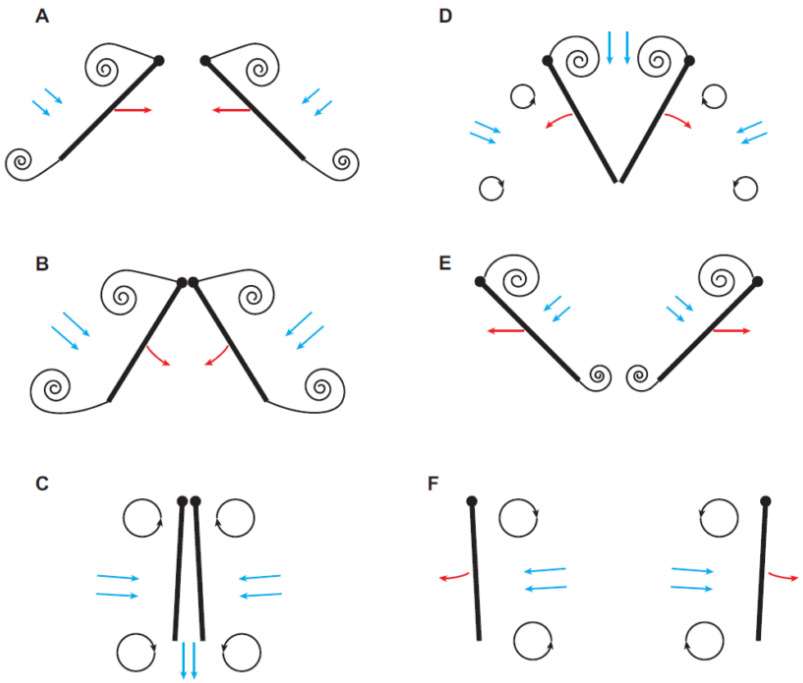

Figure 2.5: Schematic representation of clap-and-fling motion by use of two rigid wing sections with the red arrows indicating the direction of the wing motion and the blue arrows indicating the direction of the induced flow [62]

The additional force generation perceived as a consequence of this unsteady mechanism has several different explanations proposed by several studies [49, 66] . It could be caused by the momentum

jet generated during C were flow is pushed downwards. The fact that a large LEV is formed during the fling (D) can cause an increase in the circulation of the wings. But also the starting vortex formed during the stroke reversal (D and E) is attenuated due to the proximity between wings. When the wings are flexible instead of rigid, they may display a strong deformation especially during the fling phase, and consequently the mechanism is called clap-and-peel. The flexibility of the wings plays a crucial role in the force generation of flapping wings. Lower drag and higher lift forces can be achieved with flexible wings compared to rigid ones [62] . The deformation acts in favor of enhancing the probable causes of force generations explained above.

Wake capture

The motion of flapping wings, as it has been explained, generates a series of vortex structures that are shed into the wake. When the wake structures do not convect fast enough away from the body, the wing passes through the same region on the following cycle and it will encounter areas of high energy content (figure 2.6). A transfer of momentum from the fluid to the wing will take place. The final increase in force generation due to this mechanism is highly variable as it depends on the rate of convection of the wake and on the sign on the vorticity regions that are crossed by the wing. This mechanism becomes more important on hovering conditions as in forward flight the convection of the wake structures does not allow a strong wing-wake interaction.

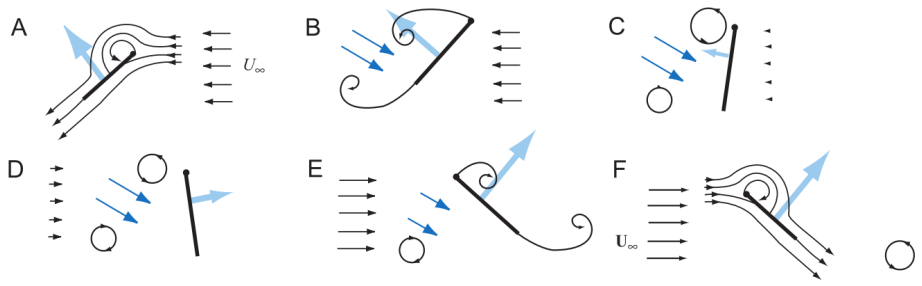

Figure 2.6: Wake capture mechanism evolution sequence indicated from A to F [66]

Added mass

When the flapping wing accelerates during the cycle, the fluid adjacent to the wings is also accelerated. This will lead to an increase in the apparent inertia of the moving wings as the mass of the accelerated fluid should also be considered. This is called added or virtual mass. The contribution of such phenomenon is hard to quantify.

2.1.4. Parameters influencing flapping wing aerodynamics

Flapping wing aerodynamics is a combination of several complex phenomena so many parameters affect the aerodynamic performance. This is the main reason why it is difficult to design an FWMAV that can operate in very different scenarios. The wing deformation has been already established above as one cause for thrust and lift increase. But in the same matter the deformation of the wings depends of the flexibility of the wing structure and also the wing kinematics that depend on the rotational speed of the wings, the free stream velocity and the interaction between the air and the wings [56]. This becomes a problem of fluid-structure interaction [24] that is computationally very expensive to accurately simulate numerically.

Lentink & Dickinson experimentally studied the dynamic scaling parameters of revolving wings that are responsible for the enhanced LEV. The analysis showed the potential stabilizing effect that wing kinematics have on the LEV generated on revolving wings. In addition to the Reynolds number, they chose two further governing non-dimensional numbers for this study: the Rossby number (Ro) that indicates the Corioris acceleration and the dimensionless stroke amplitude ($A*$) which relates to the level of unsteadiness of the flow. The Rossby number in revolving wings is defined as $Ro = R/c$ where R is the radius of gyration of the wing which in this case is set to the wingtip radius and c is the mean aerodynamic chord. The dimensionless stroke amplitude is defined as $A* = \Phi R/c$ where Φ is the stroke amplitude. To determine the effect of these parameters in LEV stabilization, a set of experiments was carried out. Using both flow visualization and force measurements, they concluded that Ro, and not

$A*$, appears to explain LEV stability. In figure 2.7, different flow patterns around a revolving wing can be observed on the left picture, represented by the Reynolds number of the flight, the Rossby number and the dimensionless stroke amplitude.

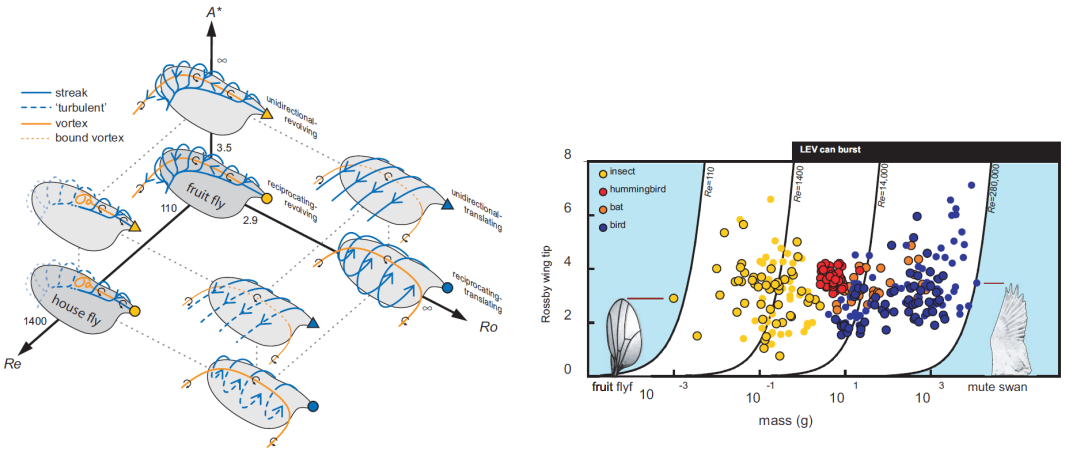

Figure 2.7: Left:Cartoon of basic flow structures for different values of $A*$, Ro and Re (left) and Rossby number based on wing tip radius for natural flyers (right) [50]

Force augmentation decreased with increasing Ro, which is consistent with the general prediction that the LEV is stabilized at low Ro. In the plot on the right a large set of data is presented where the Rossby number of animal wings assuming zero advance ratio is plotted as a function of body mass of the animal. It can be seen that the Rossby number does relate strongly to the size of the weight of the animal. Apart from the freestream velocity and wing kinematics, the direction at which the flapping wings are facing the flow. This means that the body angle of attack can affect the aerodynamics forces and this parameter is probably coupled with the other flight parameters already explained. This coupling of different parameters has been verified to occur in the DelFly [46].

Other factors that can affect the behaviour of flapping wings are the dynamics of the animal or MAV, that lead to non-stationary flight conditions. Different maneouver such as turns change greatly the force generation as well for example an external phenomena such as gusts. However this kind of conditions are difficult to simulate both numerically and experimentally and the force measurement or flow visualization becomes even more complex. This is out of the scope of this study.

2.2. Numerical vs. Experimental approach

From the previous section, it is clearly noticed that the study of flapping flight is very complex and it depends on many different factors. In order to tackle this problem in a systematic, different approaches have been followed. Flapping wings aerodynamics is often related to revolving propeller blades as both generate lift by pushing air downwards. The flapping cycle can be simplified if it is divided in two half-strokes and each is assumed to be represented by the motion of a revolving wing. Under high angle of attack, a regular translating wing generates a well know Karman street, however it has been observed that the stable LEV mentioned above is also generated for revolving wings [35]. A leading-edge vortex (LEV) is generated as a consequence of flow separation at high angles of attack which leads to a low pressure region where strong suction forces perpendicular to the wing surface appear. Usherwood and Ellington [81] studied these phenomenon on hawkmoth wings at a Reynolds number of 8,000. A translating wing could sustain a maximum lift coefficient of 0.71 while the revolving wing could go up to 1.75. It can be stated then that a key element for the enhanced aerodynamic force generation is the rotational inertial mechanisms of the flapping wings.

Successful theories for the far-field wake of flapping wings were elaborated based on the extensive work already available on rotor aerodynamics [31, 65]. However researches have not been able yet to derive near-field theories in this subject that can be applied to different wing shapes, flight conditions, etc [67]. Comparisons between the results from experimental campaigns and the widely used quasi-steady lift models have been discussed by Gutierrez [39]. Depending of the quasi-steady model used, different values of lift-based weight support are computed. The final lift calculates also depends to

a great extend on the wake measurement location behind the animal ($x = c$) and the flight speed (U). There is an extensive variety of flight conditions that are covered by natural fliers. The shape of the wings influences as well the aerodynamics of flapping wings. This adds an extra complexity to any model as it does not only have to be dependent on flow conditions but also on the shape and aspect ratio of the wing [77]. The poor performance of these models is confirmed and it also shows the sensitivity of these models to the input parameters. The main conclusion that can be extracted from this study is that the flapping wing mechanism is very complex and thus no general theory has been found to accurately model the aerodynamics of flapping wings.

2.2.1. Numerical studies

Apart from analytical models, CFD simulations of flow around flapping wings have been carried out. CFD provides detailed and complete flow information that can help in the understanding of the flow characteristics near the wing. One of the main limiting factors of CFD simulations is the way the wings are modeled. Real flapping wings are flexible so that their deformation along the flapping cycle cannot be disregarded [12]. The use of fluid-structure interaction methods to study the influence of the flow on the wing shapes should be developed in order to make this approach closer to the real behaviour of the flow and the vortex structures generated. Another option that has been explored is the use of deformation patterns from experimental measurements to take this effect into account and proceed to make numerical simulations with that data [26, 59]. CFD solutions have the advantage of providing information of the velocity field around the flapping wings as well as the pressure distribution along the wing surface, as seen in figure 2.8. The main structures explained previously can be seen in the left side of the figure, structures such as the tip vortex, the leading edge vortex and the trailing edge vortex. With this information, a better link can be made from the aerodynamic behaviour obtained to the forces generated by the wings. Deng at al. measured the deformation of the wings of the DelFly, the same kind of MAV that will be studied in this project [25]. The experiments and simulations carried out showed how the flexibility of the wings are directly related to the force generation. The efficiency and the force generated by the flapping wings of the DelFly increase when the flexibility of the wings increases as well. The main effect influenced by the flexibility of the wings is the clap-and-fling mechanisms which is present in the DelFly aerodynamics. Interesting results can be reached following the combination of experiments and CFD. However, the CFD computations are still dependent on the experimental information from the motion of the wings to be able to analyzed the flow around flapping wings. This leads to the conclusion that experiments are the most direct and accurate way to study the flapping wing mechanism.

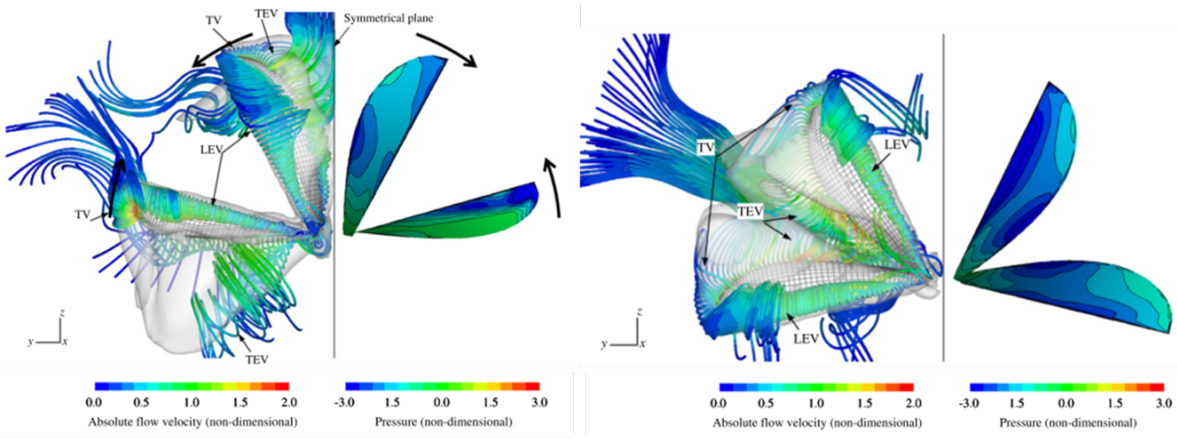

Figure 2.8: Instantaneous streamlines, iso-vorticity surface and pressure contours on the upper surface of flapping wings in biplane configuration at each half stroke. [59]

Experiments have been done using natural fliers such as birds and insects and also using MAVs or simplified models that are not able to fly. There are two main kinds of experiments that can be performed with natural fliers. The first one regards the experiments done with a tethered subject, so the insect for example is rigidly fixed at a certain position resembling the normal flight conditions of the animal [9, 10]. The other possibility is letting the animal fly freely across the measuring space and

measure the footprint of the vortex structures generated during the flapping [13, 39]. This last approach implies quite a complex set up which also includes extensive training as well as the design of protection garment for the animal to be tested in case that laser light illumination is used.

2.2.2. Experiments on natural fliers

Focusing on experiments done in tethered conditions, several experiments lead by Bomphrey can be pointed out. The use of digital PIV measuements allowed the first time ever empirical measurements of the downwash distribution produced by a tethered (restrained) desert locust [8]. Before a factor (k > 1) was added into the actuator disc models to account for efficiency difference (theory assumes uniform downwash accerelation), but this factor had no base. Actuator disk models are the standard model used by the animal flight community. The wing can be thought of as deflecting a circular jet of diameter b (span) downward with velocity 2ω. Lift estimation according to measurements are 10 times higher than theory. With the same digital PIV technique, the first leading-edge vortex was captured in 2D measurement planes of a tethered Tobacco Hawkmoth [9]. The wing length of such insect is approximately 52 mm and it was fixed with a body angle of 28^o from the horizontal plane. The subtraction of the free-stream was performed in order to reveal the focus of the LEV along the wing. The kind of vortex structures that were determined can be seen in figure 2.9. Looking at the velocity profiles of cross sections through the loops shed into the wake it seems that the vortex core of the tip vortices can be well defined as the distance between peaks in rotational velocity (vertical velocity when looking at figure 2.10, part C). The velocity profiles found are similar to the ones that could be found on ideal vortex rings and their cores.

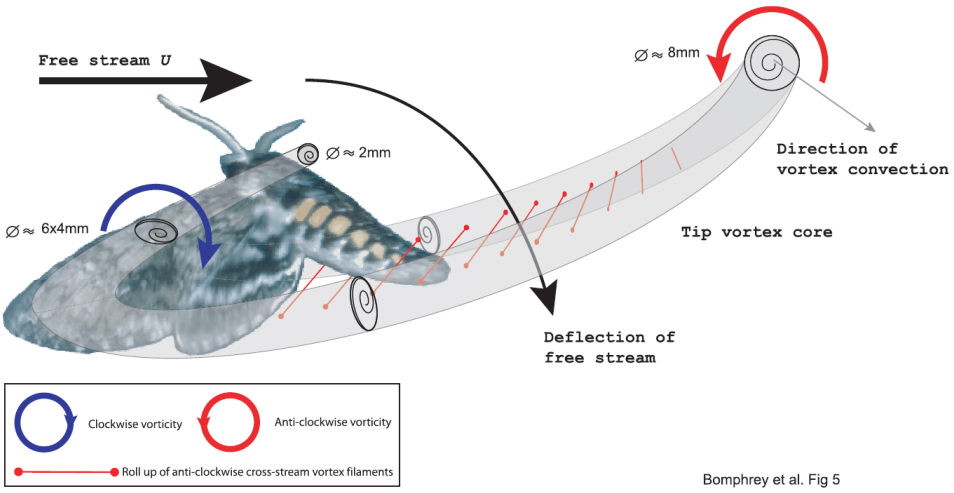

Figure 2.9: Production of a vortex loop with cross-sections of the loop core ($V_\infty = 3.5\ m/s$) of a tethered Tobacco Hawkmoth [9]

Experiments in free flight conditions have been carried out as well in recent years. The quantity of such experiments is smaller compared to the ones performed with tethered conditions due to the increased complexity of the systems involved. For example, Gutierrez et al. performed stereo PIV measurements in still air on the wake of a parrot [39]. Safety garment needed to be designed for the animal to avoid the harmful effect of some equipment such as the laser light. In addition, colorless and odorless fog (size of $1\mu m$) had to be used. The absence of 3D velocity data resolved in time and space leads to the use of simplified quasi-steady lift models in the majority of animal flight studies in order to derive aerodynamic models to estimate forces generated by the wings. A comparison is done in this study between the three commonly used quasy-steady lift models: Kutta-Joukowski theorem, vortex ring model and actuator disk model.Vortex breakdown was found in the measurements which violated the ”frozen turbulence” hypothesis, so the three methods used are not valid or they build up on assumption that is not correct in this case. The quasi-steady lift can be estimated by means of wind tunnel experiments. However when discussing studies in still air, like this one, the estimation of the quasi-steady force can only be performed for the associated stroke phase that is captured by the laser light when the bird flies through the laser sheet. For the case of the parrot, it is observed that lift is mainly created on the downstroke where two large tip vortices are generated.

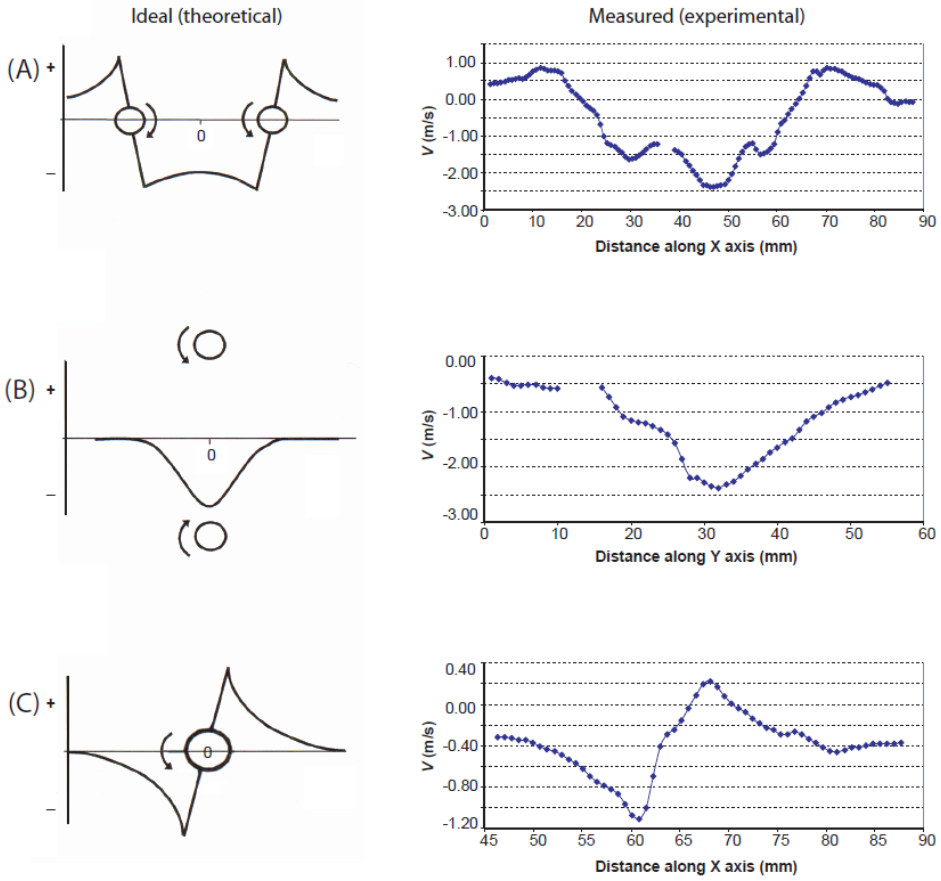

Figure 2.10: Velocity profiles through ideal and measured vortex loops ($V_\infty = 1.2\ m/s$) of a tethered Tobacco Hawkmoth [9]

Apart from planar measurements, some experiments on 3D volumes have been accomplished. This is the case in a study of a desert locust with tomographic PIV measurements, one of the first experiments done with tomo-PIV in flapping wings [11]. The insect is fixed in a position similar to its normal flight conditions. The lack of detail provided by planar or stero PIV lead to a poor visualization of the wake structures, which motivated the use of tomo-PIV instead to be able to observe wake elements undetected until then. The experimental set-up consisted of four high-speed cameras recording at 1 kHz and the seeding particles used are olive oil droplets. The measuring volume that could be achieved by this technique was limited to a thickness of 4 mm, measured in the longitudinal direction, in order to be able to cover all the wake in width and height ($60 \times 80 \times 4\ mm^3$). The small thickness makes the use of Taylor's hypothesis inevitable to propagate the flow information downstream in order to describe the full wake, and the investigation revealed that the use of Taylor's hypothesis introduces errors on wake morphology which can lead to erroneous force calculations based of such information. The Taylor's hypothesis assumes a homogeneous, frozen, turbulent wake so that the wake structures are convected with a constant velocity equal to the free-stream. To correct for this, wake deformation was taken into account in this case by looking at the angle of the Q-criterion [43] iso-surfaces and matching them from one measurement to the next. With wake deformation applied, the shape of the wake structures was found to change significantly. This leads to the conclusion that volumes captured at subsequent time intervals do not allow to reliably compose the actual three-dimensional wake shape and a large volume imaging technique would be desired that can properly capture the longitudinal extent of the wake. This cannot be achieved by regular tomo-PIV as discussed by Scarano et al. [71], however, in view of the volume restrictions. Looking at the results shown in figure 2.11, the vortices generated by the wing during the upstroke have the opposite direction as the one in the downstroke due to the change in the effective angle of attack seen by the wings, generating positive or negative force consequently. As the desert locust has four wings, the period where the final force is negative is very short as when two wings are generated negative lift the others create a positive one.

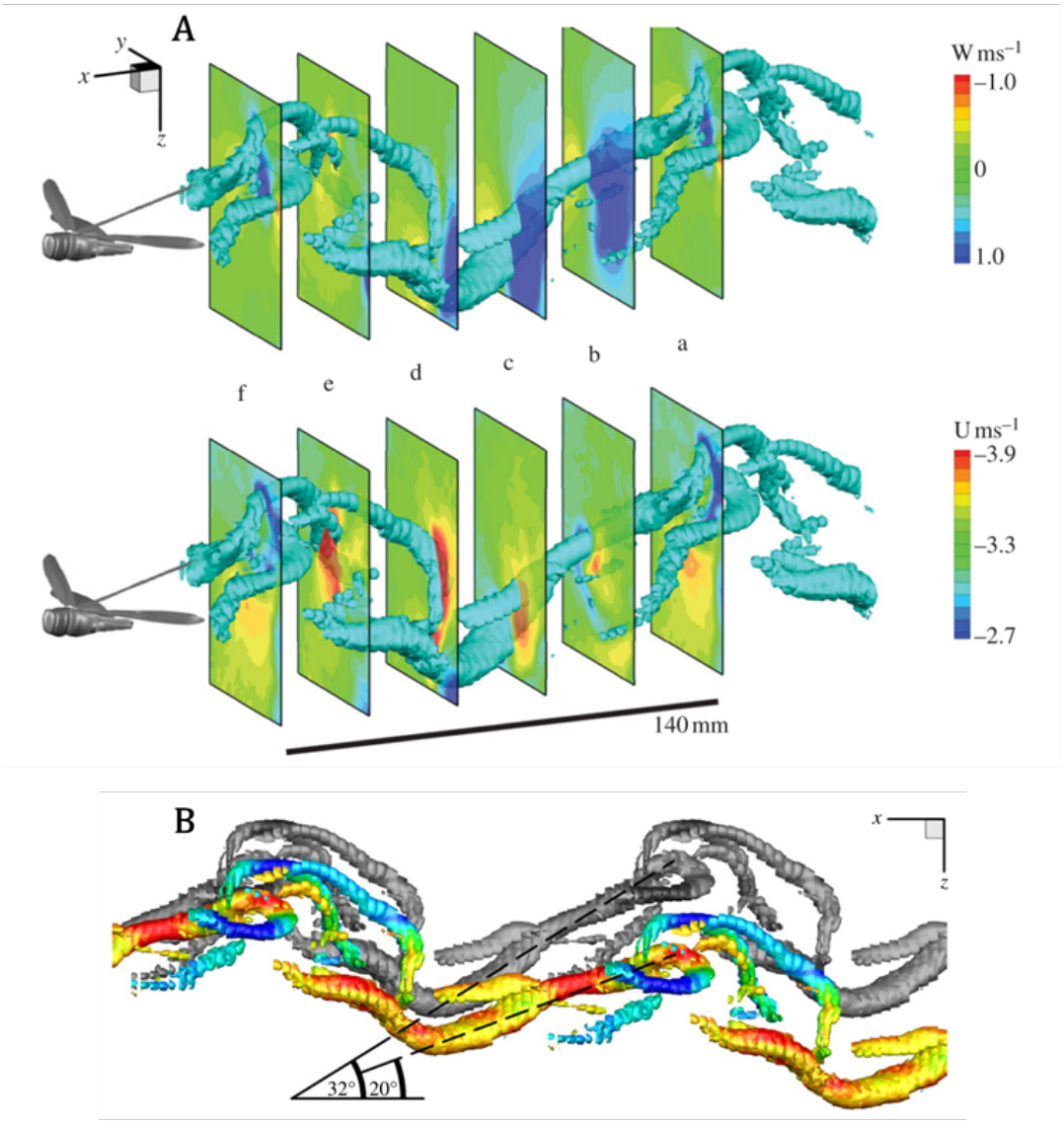

Figure 2.11: **A:** The phase-averaged vortex wake of a representative individual with six planes corresponding to snapshots through the stroke cycle at $t/T = 0,\ 0.2,\ 0.4,\ 0.6,\ 0.8$ and 1.0 (where t represents the current time-step within the wingbeat, and T is the wingbeat period). **B:** Grey vortex wake: phase-averaged vortex wake of a desert locust reconstructed from stacking successive wake volume acquisitions. The coloured wake, coloured by vorticity in the freestream axis, ω_x, has been subjected to vertical (z-axis) realigned of the volumes, based on the largest vortex structures found in each volume to indicate direction of wake deformation. [11]

To overcome the measuring volume limitations, in the current study, large-scale Robotic Volumetric PIV is used, instead of regular stereo or tomo-PIV, to visualize the entire 3D wake structures without necessity to rely on any hypothesis to reconstruct them. Another difficulty of experiments with insects is the difficulty to repeat the measurements at the same conditions, due to the inherent unpredictability of animal behaviour. This can be generalized to all experiments done with natural fliers, which reduces drastically the range of configurations that can be studied and the number of parameters that can be changed. These issues are less critical when mechanical flapping mechanisms or MAVs are used instead. As explained by Cunis et al. [19], the measurements with MAVs have the potential to bring more consistent and repeatable data. This is a crucial step towards a deeper and broad understanding of the flapping wing mechanism. Multiple bio-inspired FWMAV designs have been developed worldwide, designed by different institutes like the RoboBee from Harvard University [17] or the Nano Hummingbird from AeroVironment [48]. Both of these designs are tailless, while others like the DelFly II, made by Delft University of Technology [20], have a conventional tail for stability and controlability.

Nevertheless, due to the highly complex three-dimensional behaviour of flapping wings, a significant part of the mechanism cannot be analyzed. Several studies have attempted to reconstruct the three-dimensional wake from measurements performed on a limited space. One option for the reconstruction is to assume the the wake is frozen, called Taylor's hypothesis. The assumption implies that the vortex structures shed by the flapping mechanism convect with a velocity equal to the freestream velocity. In this way, the evolution of the vortex structures can be represented. However only the information of structures seen by in the planar measurements is used so no other structures in the out of plane direction can be found. This approach has been followed by Percin et al. [60], as shown in figure 2.12. However it has been shown that the Taylor's hypothesis is not for the wake of flapping wings as the induced velocities generated by the vortex structures themselves have a great influence on the evolution of such structures along time and space [11].

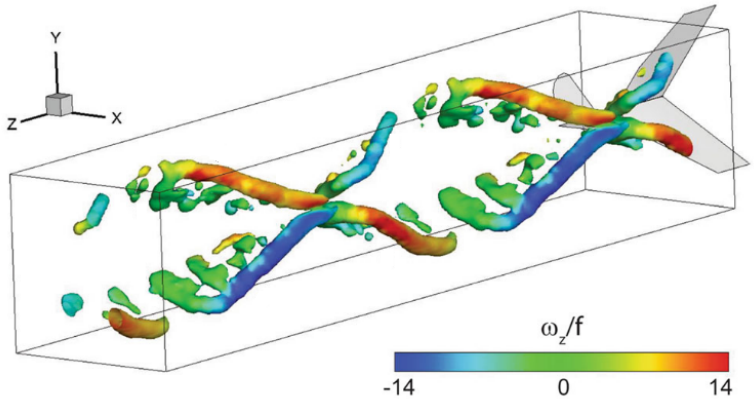

Figure 2.12: Perspective view of the wake structures visualized by isosurfaces of $Q = f^2 = 10$ and colored by ω_x/f for two periods of the flapping motion (flow is the positive z-direction) for the case of $k = 0.47$ ($U_\infty = 3$ m/s and $f = 5.7$ Hz) [60].

2.3. The DelFly II

The DelFly II is a biplane MAV designed and manufactured at TU Delft [21]. The DelFly project was originated in 2005 as a design synthesis project for students. The objective of such project was to '*design a flapping wing UAV of less than 50 grams with on-board camera that will impress the jury of the European Micro Air Vehicle conference and competitions 2005*'. In 2006, the DelFly II project was established. The goal for this second project focused on decreasing the size of the FWMAV. One year later, the DelFly II was presented and succesfully exceeded the project's goals: not only the wing span was reduced to 28 cm, but also there was a significant extensions of the flight envelope. The DelFly II is able to hover, fly forward at 7 m/s and even fly backwards at -1 m/s. It has two full-span wings, arranged in cross configuration, that move alternately towards and away from each other when flapping (see figure 2.13) to generate both thrust and lift, taking advantage of the clap-and-fling wing-interaction effect [4]. The wings of the DelFly are made of 15 micron thin Mylar foil reinforced with carbon fiber stringers that makes the wings highly deformable, a characteristic that was found to enhance significantly the aerodynamic performance of the MAV [61]. It is also equipped with horizontal and vertical tail planes and its corresponding control surfaces, elevator and rudder, which make the DelFly a stable and controllable system relying on tail actuation. The DelFly MAV used in the experiments is the most recent design. The lay-out and dimensions of a half-wing of the MAV can be seen in figure 2.13. The weight of the DelFly is around 25 g and the distance from the leading edge of the wings to the trailing edge of the tail is 21.5 cm approximately. The total span of the wings is 28 cm, while the tail has a span of 17 cm.

2.3.1. Experimental capabilities of DelFly II

As in the case of natural fliers, measurements on MAVs can be done in fixed (tethered) conditions or in free flight conditions. The research done on the DelFly in fixed conditions is quite extensive. These static measurements are less complex to be performed and, with the help of a force balance, the forces generated by the flapping wings can be measured simultaneously to the flow visualization. This allows

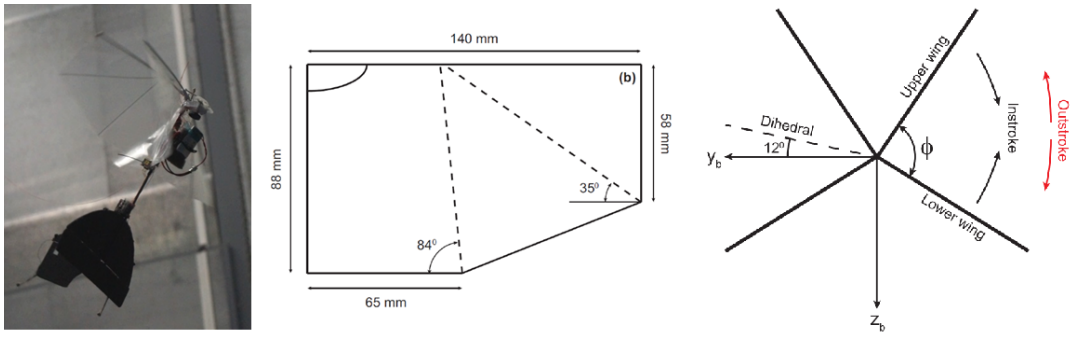

Figure 2.13: The Delfly MAV used in the experiments (left). The dimensions of a single half-wing, including the location of the stiffeners (middle). The location of the leading edges of the wings in front view.

valuable information to be obtained of the possible relation between wing motion, wing deformation, flow behavior and resulting force generation. The complexities encountered when modeling and simulating the interaction between flexible wings and the wake itself contribute to the limited possibilities to use computational approaches for the investigation of flexible biplane flapping wing configurations. This is why predominantly experimental studies have been performed on the DelFly. The PIV research carried out in previous years on the DelFly has always been limited to planar (2C and stereo) PIV [18, 37] , so information is restricted to a plane. In addition, the optical access is limited when looking directly at the flow around the wings. The wings may block or reflect the laser light and a convenient solution for this may be a phase-averaged procedure where the camera or set of cameras used for the PIV measurements are directed in the plane perpendicular to the laser sheet. As the wings also move along time, the images needs to be acquired at the exact time that the wings pass through a certain phase. Such an experimental set-up adopted by the studies of Groen [38] and De Clercq [18] is illustrated in figure 2.14.

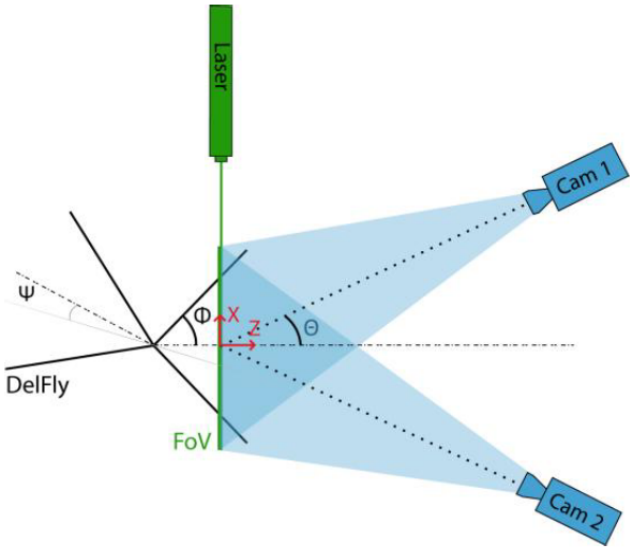

Figure 2.14: Schematic representation of the experiment arrangement [18]

2.3.2. Planar and Stereo PIV measurements

On the experiments performed by Groen [38], a Hall sensor is used to measure the flapping frequency and to generate the triggering pulse for the PIV system. PIV measurements are done in a phase-lock manner (50 phase-lock images per phase location - 34 different locations). To keep the laser sheet oriented perpendicular to the wing for investigating the different phases, the DelFly is rotated along its body axis. The DelFly used has no tail. Only the flow around one wing was measured at

a constant spanwise location. The tracer particles used are fog particles of approximately 1 μm of diameter, like other regular PIV tracer particles. The study focuses on the flapping wing behaviour at the hovering flight regime, which is the most demanding configuration for the DelFly. Two force sensors are used to understand the performance of different wing models and the influence of the stiffness, orientation and shape of the stiffeners that configure the wing (see figure 2.15). Then stereo PIV measurements are made to investigate in more detail what the effect that increases the performance of the DelFly is. An aeroelastic study is also performed by measuring the deformation of the wings at the span location where stereo-PIV is carried out. This study allowed to find an improved wing geometry, which is currently used in the the latest DelFly design. The clap-and-feel mechanism is studied by comparing the thrust produced by a biplane configuration and twice the thrust generated by a single wing. Thrust generated during the out-stroke is higher than during the in-stroke, probably due to the clap-and-peel effect at the beginning of the out-stroke. Improvement of the new wing decreased mainly the power consumption, while maintaining the lift production capacity. The results of the deformation measurements could be used to understand aerodynamic effects, but also as an input for numerical flow simulations (see figure 2.16). The path of the leading edge describes a figure of eight, due to passive wing deformation, which has been assumed to have a positive effect on thrust generation.

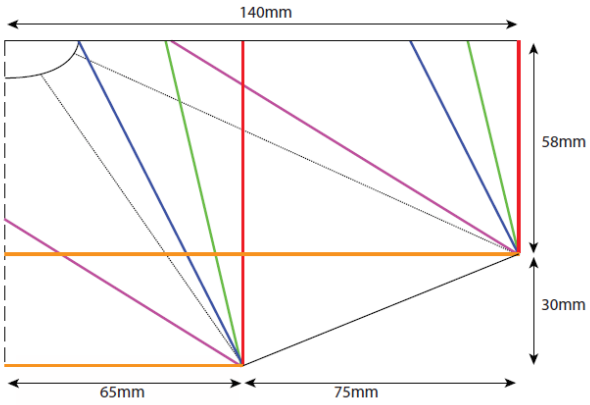

Figure 2.15: DelFly wing schematic representation of different stiffener location [37]

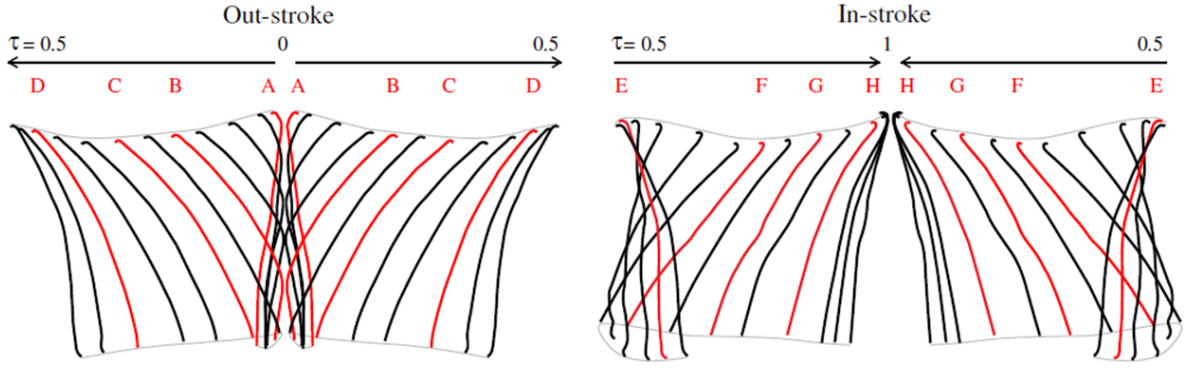

Figure 2.16: DelFly cross-section wing deformation along a flapping cycle at a wing flapping frequency of 11 Hz at a spanwise location of 100 mm from the root ($0.71b$) [37]

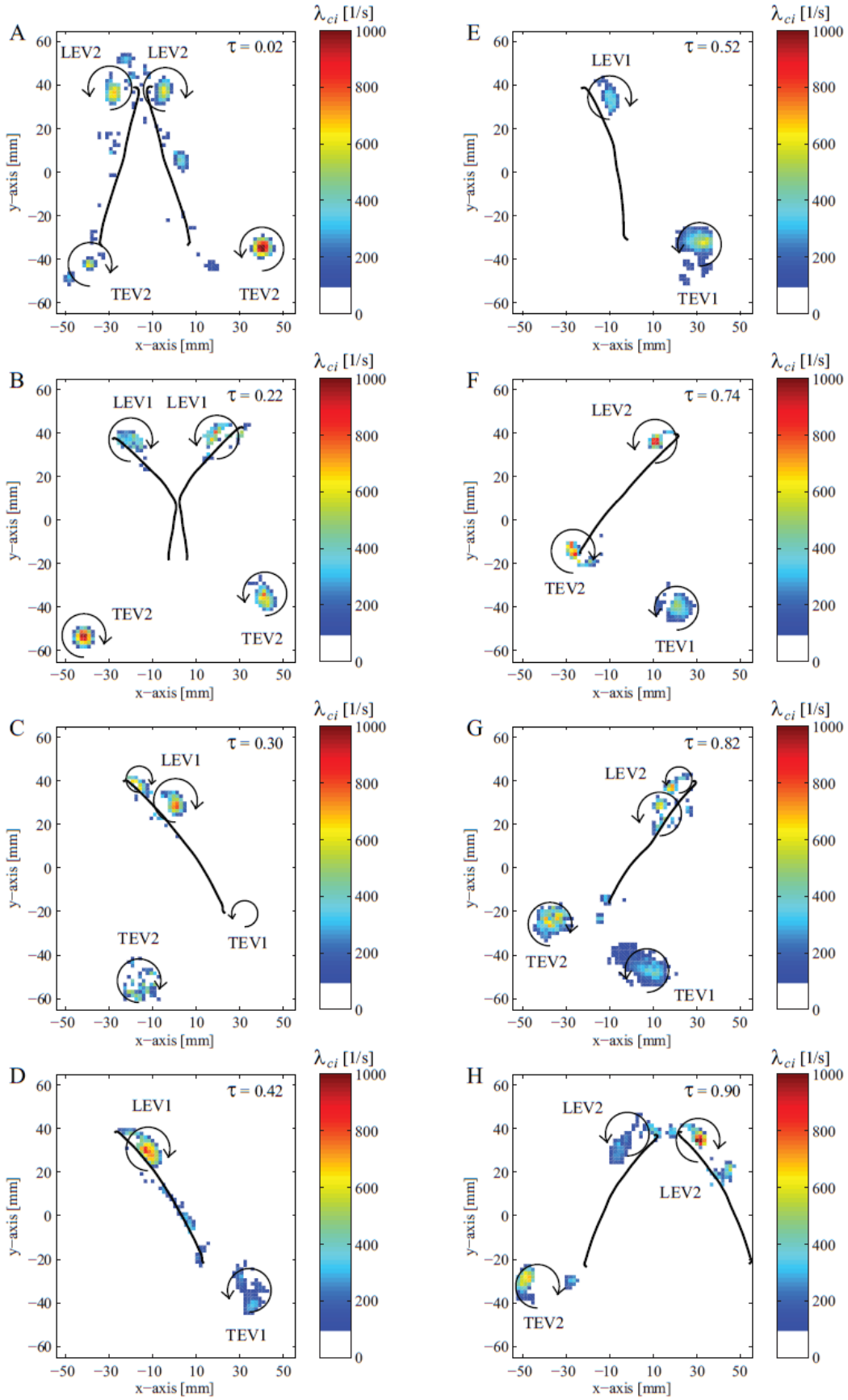

Figure 2.17: Swirling strength at various moments during the flapping cycle, showing leading edge vortices (LEV) and trailing edge vortices (TEV) during out-stroke (1) and during in-stroke (2). The swirling direction is taken from velocity field images. [37]

Investigation of the vortex dynamics in the cross-sectional plane normal to the wing leading edge is shown in figure 2.17. Swirling strength instead of vorticity is used to show the vortex structures as vorticity does not identify vortex cores only but also shearing motion within the flow [2]. Different LEV and TEV can be seen along the flapping cycle in figure 2.17. During the outstroke a LEV is formed but at the beginning of the instroke it dissipates, but a new LEV is again generated halfway through the instroke. When the leading edge of the wings are closed again at the beginning of the outstroke, the leading edges interact and then move apart again. Some vortex shedding is observed which suggests, compared to insect flight, that the LEV of this MAV is not as stable [5, 32]. The growth of the LEV according to measurements at different spanwise locations seems to increase from root to tip fo the wings, such that the LEV develops a conical shape.

2.3.3. 3D wake reconstruction

One option to obtain three-dimensional information on the flow structure is to measure different planes subsequently, and synchronize the data of the different planes with the flapping phase. Evidently such an approach requires extensive measurements to be performed and a careful synchronization and interpolation of the datasets. A simpler but more approximate approach reconstructs the three-dimensional structure of the wake from the time-resolved data obtained in a single wake plane, by using a convection model (Taylor's hypothesis), as has been done for the DelFly by Percin et al. [60] . This approach assumes that the wake structures generated by the flapping wings of the DelFly are convected with a velocity equal to the free stream, neglecting the induced velocities produced by the acceleration generated by the clap-and-fling and the wake vortices themselves. This assumption may be reasonable for a zero angle of attack forward-flight configuration, allowing to visualize the main structures that can be seen in the wake of the MAV. The usual coherent vortical structures around flapping wings are: leading edge vortex (LEV), tip vortex (TV), root vortex (RV) and trailing edge vortex (TEV). The study of Birch and Dickinson [6] showed the importance of the TV for the stabilization of the LEV. Tip vortices are not well captured in 2D as the shape is greatly three-dimensional. In figure 2.18, the resulting wake reconstruction for a forward flight configuration is presented. The tip vortices generated by the four wings and the starting trailing edge vortex connected to the tip vortex are revealed.

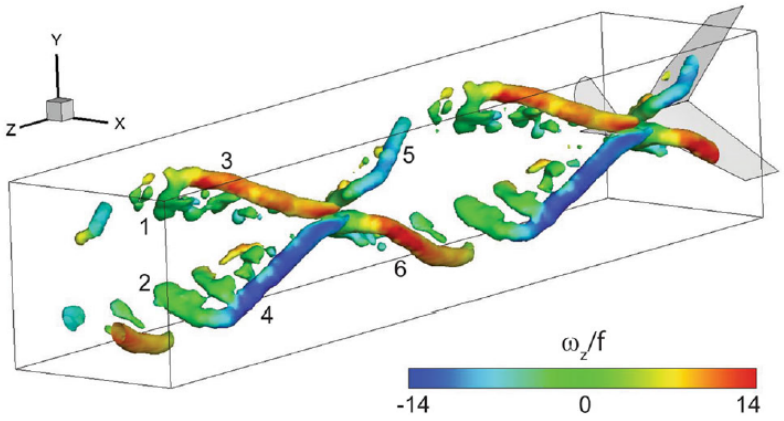

Figure 2.18: Perspective view of the wake structures visualized by isosurfaces of $Q/f^2 = 10$ and colored by ω_z/f for two periods of the flapping motion (flow is the positive z-direction) for the case of $k = 0.47$ ($U_\infty = 3\ m/s$ and $f = 5.7\ Hz$) [60]

With this technique it was also possible to assess the interaction between the vortex structures at different reduced frequencies, when changing the flow velocity and/or flapping frequency (figure 2.19). It was concluded that an increase in reduced frequency will lead to a stronger interaction between the vortices, which is linked as well with the enhancement of the clap-and-fling mechanism. Another variation between the different reduced frequency cases depicted, it is the time lag between the generation of vortical structures along the flapping cycle. It seems that the formation and convection times of the vortical structures generated in the wake differ as the reduced frequency changes and thus a phase shift is appreciated. Therefore the convection time of the spatiotemporal reconstruction is dependent on the free stream and also the induced velocities. As the flapping frequency becomes higher, the circulation along the wing increases as well and the formation of the TEV is delayed. The authors sus-

pects that likely origin of this fact is the wing deformation. The leading edge has a fixed motion but the flexible wing is affected greatly by the wing inertia. This would explain that the freestream velocity and the flapping frequency enhance the amount of deformation of the wings which consequently generates a delay and a time shift on the wake structures.

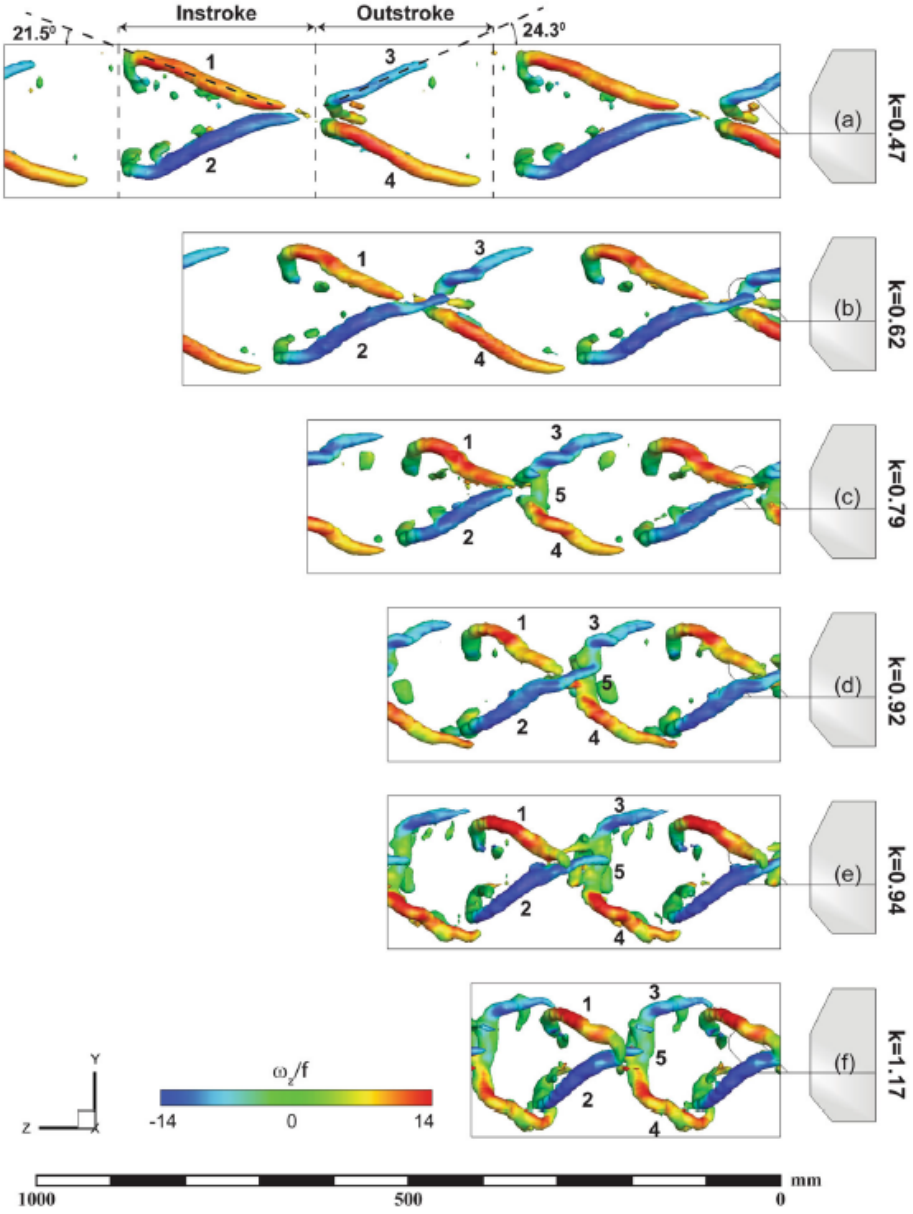

Figure 2.19: Side view of the wake structures visualized by isosurfaces of $Q/f^2 = 15$ and colored by ω_z/f for two periods of the flapping motion (flow is the positive z-direction) for a range of reduced frequencies [60]

However the use of Taylor's hypothesis on which this three-dimensional rendering relies fails to represent the wake at realistic flight conditions where the angle of attack is quite high and so the interaction between the velocities induced by the wing and the free stream is too complex to be accounted for by the simple convection model underlying the Taylor's hypothesis.

Similar experiments have also been performed for another DelFly design, the DelFly Micro. The DelFly Micro has three wing interactions compared to two for the DelFly II. Not only the two pair of wings have a clap-and-peel mechanism, but also the two upper wings of the DelFly meet each other at the end of the outstroke as shown in figure 2.20.

Measuring the motion of the leading edge of the wings, it was concluded that the aerodynamic forces

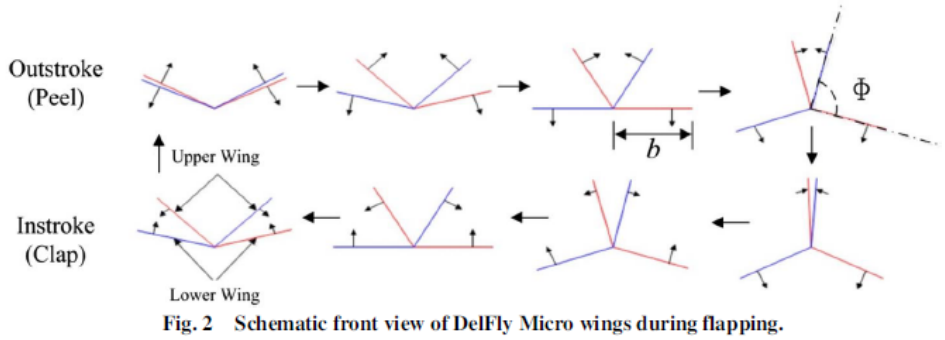

Fig. 2 Schematic front view of DelFly Micro wings during flapping.

Figure 2.20: Schematic front view of DelFly Micro wings during flapping [27]

produce a dampening effect on the wing motion. The experiments showed that thrust (measured by force balance) seems to increases quadratically with flapping frequency, having two peaks though the flapping cycle (figure 2.21). The first one occurs during the middle of the instroke while the second one with higher magnitude happens at the middle of the outstroke. As previously stated, in this experiment was also confirmed that the flexibility of the wings played an important role in the thrust generation. Peel is substantially more effective in creating a circulation around the wings than the rigid movement of the wing. In figure 2.21, the right picture shows the evolution of the vortices generated during a cycle. It can be seen how two counter-rotating vortices are shed on the leading edges of the upper and lower wings. The sign of these vortices changes sign corresponding to the opposite movement of the wings during instroke and outstroke.

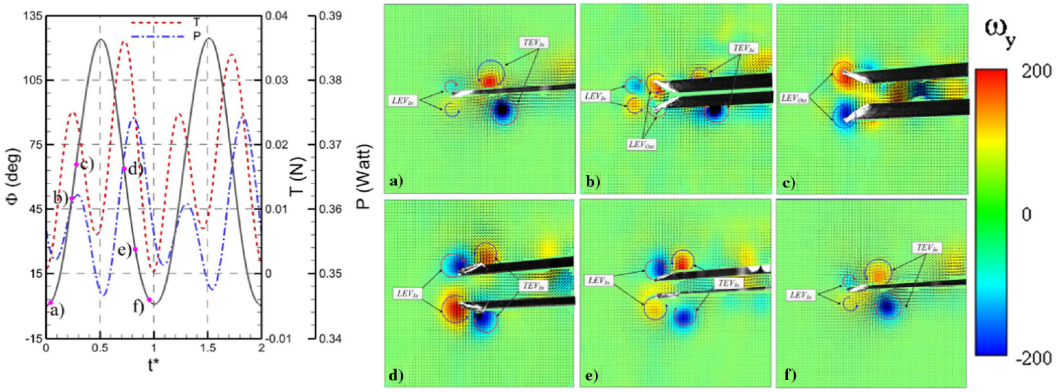

Figure 2.21: Thrust generation and power consumption (left) in two flapping cycles and out-of-plane vorticity (right) on wing at different flapping moments, measurement plane at 4 cm from wing root in spanwise direction, $f = 20\ Hz$, for $t* = \tau = [0.05,\ 0.22,\ 0.32,\ 0.72,\ 0.82,\ 0.95]$ [27]

Talking about wake reconstruction, the same procedure is followed as before, relying on a convection model based on the Taylor's hypothesis. Looking at the reconstruction of figure 2.22, there predominant wake structures are seen. They have a "U" shape that consist of two counter-rotating 3D vortices that interact with each other when the wings come together. The three structures correspond to the three clap-and-peel mechanisms identified in this MAV.

2.3.4. Experiments in free flight conditions

The first flow visualization experiments to be carried out with a freely flying flapping-wing robot have been successfully performed on the DelFly [47] , proving the methodology that will be followed in this study as well. The main characteristic of this methodology is the combination of stereo-PIV and a control system for autonomous flight in a wind tunnel environment. With a set of 13 cameras, an OptiTrack system is placed in the hall of the wind tunnel which has an open test section of $2.45 \times 2.45\ m^2$. LED markers are placed on the PIV cameras and other equipment, such as the calibration plate, to know their position in space. The DelFly is also located through markers around the wings and body. This

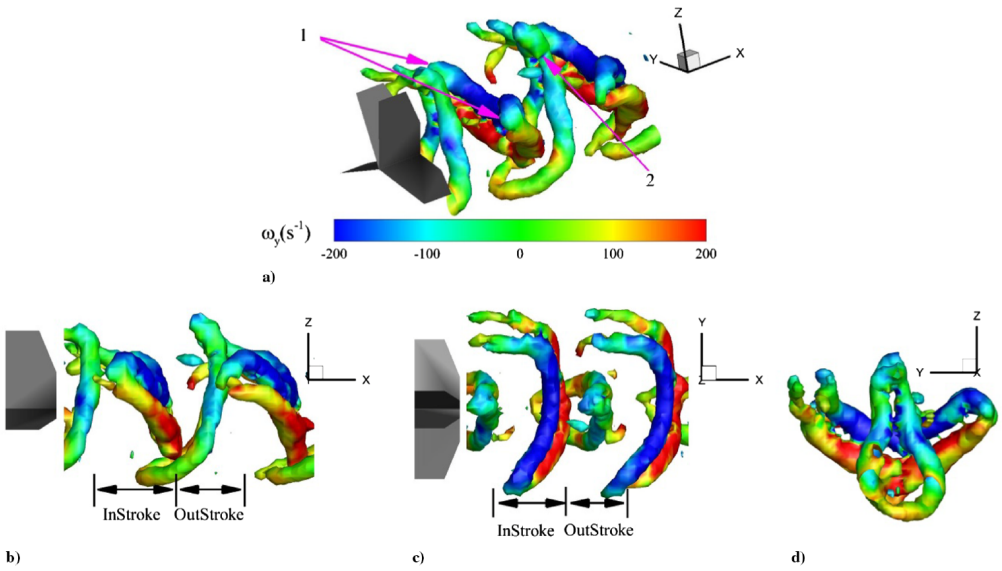

Figure 2.22: Spatial temporal reconstruction of wake of the DelFly Micro wings, $f = 20\ Hz$, $Q = 1600s^{-2}$: $a)perspectiveview, b)sideview, c)topview, and d)frontview.$

visual system is used to control the DelFly motion through an on-board autopilot. The DelFly is set to hover at a certain location while a certain free stream velocity is blown from the wind tunnel. This effectively will represent the flight conditions obtain as when the DelFly would fly at that same velocity through space. When the free stream velocity is set to a determined value, two other important flight parameters are also directly fixed, as they are dependent on each other, such relations can be found in figure 2.23 [46]. These parameters are the flapping frequency of the wings and the angle of attack of the body with respect to the free stream. Stereo-PIV measurements at an acquisition frequency of 5 kHz are performed in the wake of the DelFly, at 150 mm from the tail, to avoid reflections and shadows. Taylor hypothesis is used to reconstruct the spatio-temporal evolution of the wake as it was previously explained [62].

The variation in the position of the DelFly increases with increasing free stream velocity as the DelFly becomes more difficult to control. At low speeds, the pitch angle is larger ($50.5^o - 68.6^o$) and so the wake goes downwards and it is not captured by the PIV system. Thus, the need to use higher velocities appears so the pitch is decreased ($33.8^o - 28.7^o$). For low speeds, PIV measurements could be triggered for 49-65 % of the attempts while at high speeds only 3-4.8 %. Roll and yaw angles are present in the experiments due to imperfections on the hand made DelFly. Figure 2.24 shows the experimental results of the 3D representation of the wake vortex structures at a reduced frequency $k = 1.25$ ($U = 2.4m/s$ at $f = 12Hz$). 12 cycles are captured with 400 frames per cycle. Helicity is used for the detection of the vortex cores. There is a very prominent red structure (positive helicity) which is the tip vortex on the top wing and then a blue one (negative helicity) which is the tip vortex of the bottom wing. Both are structures formed during the instroke, while the outstroke is not well captured. Good qualitative agreement is found between the free-flight and the tethered wake flow structures.

Another way to performed free flight experiments is to make the FWMAV pass through the measuring space. This philosophy has been used successfully to measured the wake of a cyclist [79], called the 'ring of fire' concept. Research performed by del Estal et al. used the same idea for the DelFly, aiming to visualize the unsteady flow structures around the MAV in true free flight [22]. The DelFly II is driven by an automatic flight control system in a trajectory through the test space. Flow visualization was achieved with particle image velocimetry (PIV) using helium-filled soap bubbles (HFSB) as tracer particles [72]. The flight speed used for the experiments was around $1m/s$, with the pitch angle and the flapping frequency being around 60^o and $14Hz$, respectively. The automatic control system used for this free-flight investigation consists of an optical tracking system and an onboard autopilot system. The test area was enclosed at the sides with a net to contain the bubbles so as to maintain a sufficient tracer concentration. Two different PIV configurations were used: planar PIV measurements were performed in a streamwise (i.e., chordwise) aligned plane and stereo PIV measurements took place in a

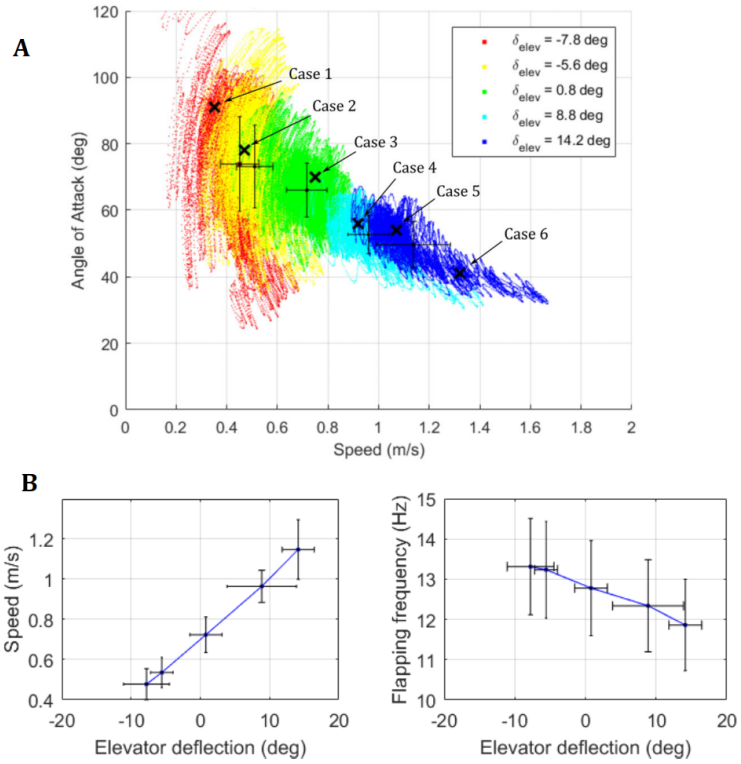

Figure 2.23: A) Observed combinations of speed and angle of attack for various elevator deflections (colour coded). The black dots and the error-bars represent the mean values and standard deviations for each elevator setting. B) Variation of body speed (left) and flapping frequency (right) with elevator deflection. Both relationships are approximately linear. The error- bars represent the standard deviation from the mean values [46]

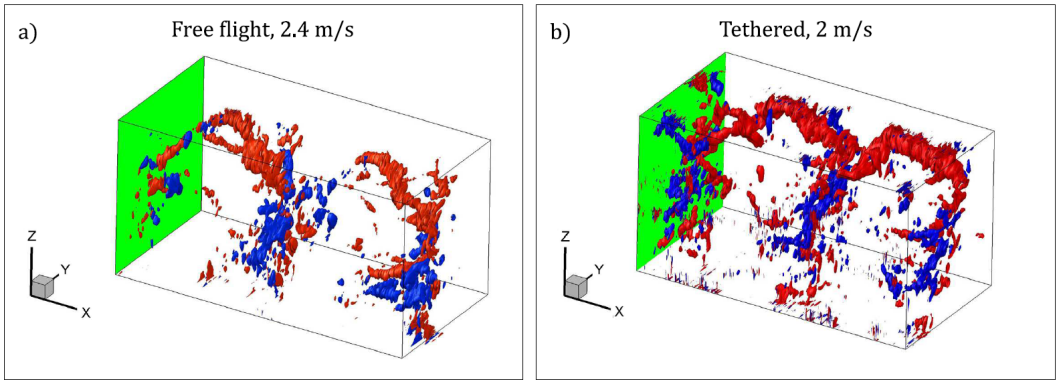

Figure 2.24: Comparison of three-dimensional wake structure of the DelFly II for (a) free-flight and (b) tethered condition; colour coding is for helicity (red: $+0.6\ m/s^2$; blue: $-0.6\ m/s^2$) [47]

spanwise-aligned measurement plane.

The position and cross-sectional shape of the two wings are clearly visible in figure 2.25, while in the shaded area the illumination is obstructed by the tail surface. At this instant, the flow structures around the two wings display a symmetric pattern with respect to the DelFly body, the lower (on the right) wing is shedding a trailing-edge vortex while the upper wing is generating a leading-edge vortex. This may be attributed to decreased effective velocity of the lower wing due to the forward (rightwards) motion of the DelFly, which also decreases the effective angle of attack. It may be hypothesized that most of the lift (vertical force in y direction) is hence generated by the upper wing during the instroke.

Virtual pathlines are plotted in figure 2.26, which were generated by applying a time-filter algorithm (with a filter length of seven time-steps). This process enables visualization of prominent rotational flow

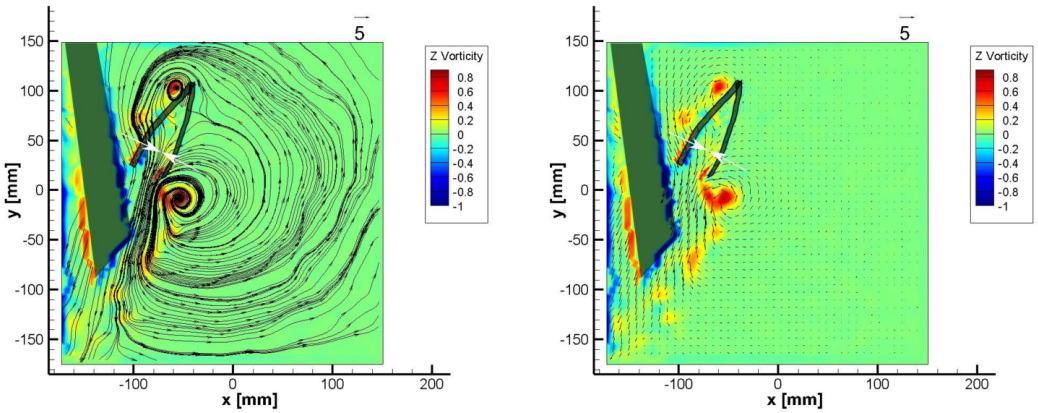

Figure 2.25: Out-of-plane vorticity [1/s] colored contours, displaying streamlines (left) and velocity field (right) around the DelFly at the end of the instroke [22]

structures, notably the tip vortices of the upper wings and the tail. Contours of out-of-plane vorticity at the end of the instroke also reveal the occurrence of wing root vortices, which have an opposite rotational direction compared to the tip vortices of the corresponding wings. Due to pitch angle, the dihedral of the wings and their deformation, the laser sheet is ”cutting” the wings in diagonal directions when the laser sheet is in span-wise direction. It is hard to define the flapping wing behaviour when the information is not measured for the four wings at the same flapping cycle stage.

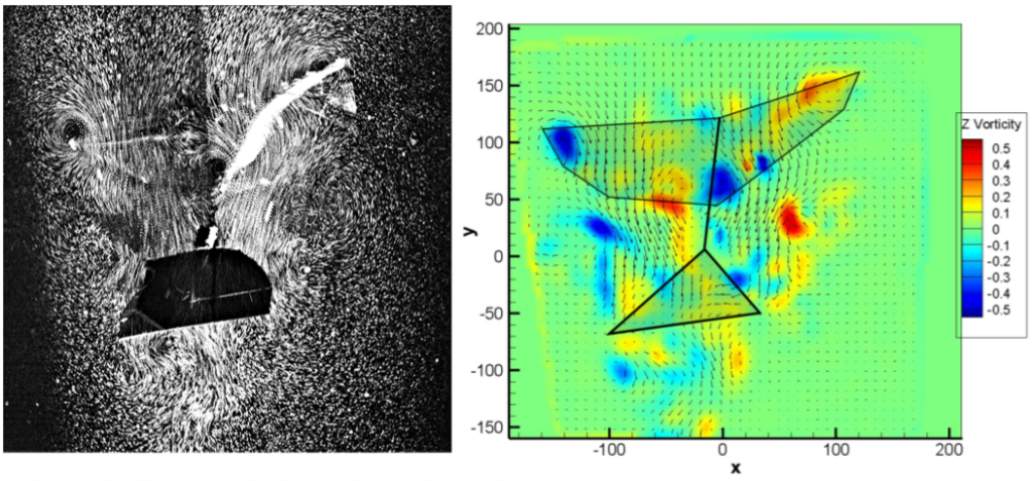

Figure 2.26: Time-filtered stereoscopic-PIV image (left) and contours of out-of-plane vorticity in a spanwise-oriented plane (right) at the end of the instroke [22]

3

Robotic Volumetric Velocimetry

In this chapter, the main developments on the field of Particle Image Velocimetry (PIV) are going to be presented. the chapter starts with a review of the basic working principles of this measuring technique to follow with the evolution from 2D to 3D and the rise of an innovative branch of PIV that includes robotic actuation.

3.1. 2D Particle Image Velocimetry

PIV is a novel flow measurement technique that has become very popular on the last decades compare to other techniques. The main principle behind it is to track and quantify the displacement of the tracer particles embedded in the fluid. With the displacement information. The name PIV was introduced by Adrian in 1984 [1], even if some years before this technique was alredy used by Meynart by the name *laser speckle velocimetry* [55]. Nowadays PIV is the most used flow measurement technique not only on research activities but also for industrial applications [45]. PIV has many advantages compared to other measurement techniques. It is a quantitative technique that measures the whole field in a non-intrusive manner and it also does not require a calibration based on other measuring instruments to achieve the desired calibration. On the other hand it needs optical access for the camera system and it involves a highly complex setup that needs a certain expertise to be correctly arranged. The measurements performed are indirect as the velocity of the tracker particles is the one measured, not the flow itself. The temporal resolution is low although several studies have worked towards improving this issue [69].

3.1.1. Planar Particle Image Velocimetry

The first form of PIV is called planar as it only enables to measure the velocities in a plane. This is a two-dimensional measurement providing information of two components of velocity (2D2C). The main challenge when performing measurements on a moving flow is the fact that the fluid is invisible. For this reason, tracer particles need to be added into the flow stream so that the flow behaviour becomes visible and therefore traceable. But in order to be able to follow the flow accurately, the tracer particles cannot be very heavy which leads to the diameter of such particles to usually be of the order of $1\ \mu m$. The area of interest, usually called the field of view (FOV), needs to be illuminated so that the particles of that specific region are clearly distinguishable. As the tracer particles are small, the light source necessary to scatter enough light needs to be very powerful. Most researches chose to use laser light as their light source due to the characteristics of the light beam that can be produced. Lasers produce a pulsed, collimated and monochromatic light beam that can be easily shaped into a sheet. Once the tracer particles are homogeneously introduced, the FOV is illuminated by a laser sheet. The tracer particles scatter the light provided by the laser and in this way the camera, set perpendicular to the field of view, captures images of the illuminated particles. The laser needs to be synchronized with the cameras for a successful experiment. The images are usually taken in pairs where the time between one and the other (dt) is very small. The period between successive pairs of images in called Δt and it provides the temporal resolution of the measurement. Each pair of images needs to be processed to compute the instantaneous flow velocity in the short time dt. Regular PIV applies cross-correlation

between the two images to find the best match between them. The cross-correlation peak provides the displacement in X and Y coordinates of the particles. To apply this procedure, the complete FOV is divided into several small areas called interrogation windows and the cross-correlation then provides the mean displacement of the particles contained in the windows. This process in explained in figure 3.1.

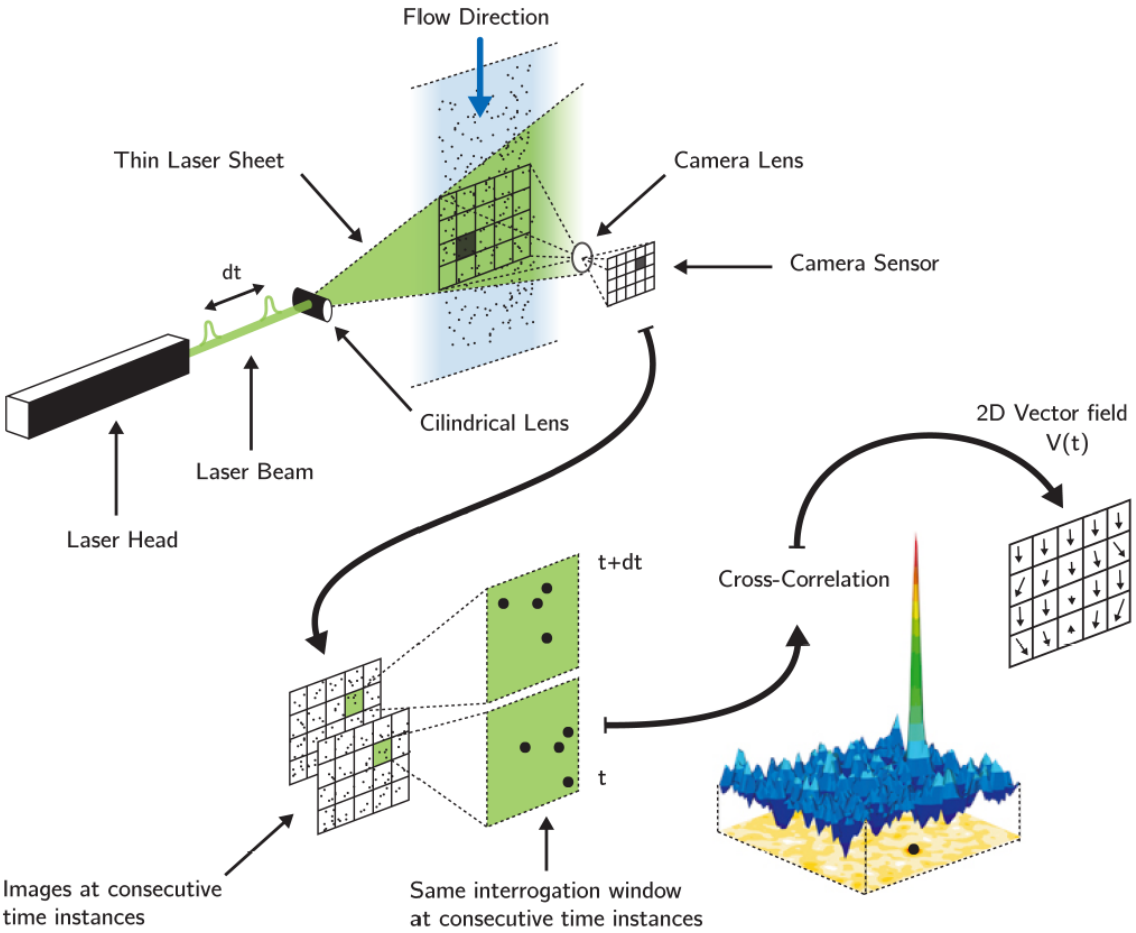

Figure 3.1: Working principle of Planar PIV [36]

The interrogation windows can change in size and they can also be overlapped to increase the resolution of the vector field. The velocities on X and Y are computed as follows:

$$u = \frac{\Delta X}{M_0 \Delta t} \tag{3.1}$$

$$v = \frac{\Delta Y}{M_0 \Delta t} \tag{3.2}$$

Where ΔX and ΔY are the measured displacements on the image and M_0 is the magnification factor which relates the displacement on the images to the physical displacement of the particles.

Another parameter that is useful to characterize a PIV system is the dynamic velocity range (DVR) which is defined as the ratio between the maximum and the minimum velocity magnitudes that can be measured. The minimum velocity is affected by the uncertainty of the displacement measurement due to the resolution of the particles in the images. The maximum velocity is limited by the time delay between the paired images and the size of the interrogation window. A trade-off appears for the definition of the interrogation window dimensions. The larger the interrogation window, the larger the maximum velocity that can be measured. However this also leads to a lower resolution of the measurement domain. Usually the DVR is required to be as high as possible, but on the case of flapping wings the

velocities at which the flow evolves are not considerably high so this is not a major concern for this study.

3.1.2. Stereoscopic Particle Image Velocimetry

One of the main drawback of planar PIV is the velocity in the out of plane direction as it is not measured. The camera is not able to recognize if the particles, apart from moving up and down and left and right, are also moving towards or away from the FOV. Stereo PIV tackles this problem. With a system of two (or more) cameras, the flow can be measured from different angles and then the sets of data are combined. As the cameras measure from different directions, the out of plane velocity can also be computed. Therefore stereo PIV is a 2D3C measurement technique. This method has been used extensively in industrial and research applications [60, 79].

3.2. 3D Particle Image Velocimetry

As stereo PIV is still a measurement on a plane, lack of understanding of 3D flow behaviour made it necessary to go a step further. Measurements in a volume become crucial in order to understand the full topology and temporal evolution of 3D coherent flow structures.

3.2.1. Tomographic PIV

Following the basic principles of PIV, a volumetric measurement can be performed with a system of three or more cameras. Apart from the regular particle identification as in planar PIV, there is a further step to be followed in this approach that consists of reconstructing the 3D domain from the 2D information from the cameras (see figure 3.2). The volume is therefore divided into three-dimensional interrogation elements to compute a vector field along the entire measuring volume. In 2006, the first 3C velocity measurement was successfully performed on the investigated volume by Elsinga [33].

The 3D reconstruction of the measuring volume from the 2D information is a computationally intensive process which becomes one of the limiting factor for application of this technique. In the past, the most widely used method to perform the tomographic reconstruction has been the Multiplicative Algebraic Reconstruction Technique (MART) [41]. This method relies on an iterative process, due to the undetermination of the problem, to obtain the distribution of the light intensity in the 3D space starting from the intensities of the plane images. The MART method has proven to have a good accuracy and it is still used for validation processed against other novel reconstruction methods. The new reconstructions methods attempt to improve the computational cost of the process. One approach to be acknowledged is the Iterative Particle Reconstruction technique which was presented by Wieneke [83]. The algorithm consist of a first 3D reconstruction of the particles that are on a second step projected back onto the images to compute the residuals. From this information the first step can be refined until the best match is found iteratively. Apart from the high accuracy of the methods, the IPR algorithm can also successfully triangulate particles in highly dense populated flows. The more particles you have in the measurement the more information that can be achieved, which makes this characteristic of the method very interesting.

Even though tomographic PIV is regarded as a state-of-the-art technique, it has important drawbacks that makes it hard for this approach to expand significantly. Due to the large amount of equipment needed, the setup of a experiment becomes very complex and a proper optical access is not always possible for such a system. It was also discussed by Scarano [71] that the maximum feasible dimensions of the measurement volume with PIV do not surpass $50\ cm^3$ and $160\ cm^3$ in air and water flows, respectively. This reduces quite drastically the kind of applications where this technique can be used, nevertheless in the research environment it is still employed [11].

3.2.2. 3D Particle Tracking Velocimetry

As explained previously the complete volume reconstruction performed in tomo PIV is excessively computationally expensive. So new approaches have appeared that focus on triangulating individual particles that are then tracked through the images with the information provided by all the cameras according to triangulation procedures. This process to follow the particles from one instant to the next is called Particle Tracking Velocimetry (PTV). As individual particles are tracked, it gives the opportunity to achieve a higher spatial resolution due to the fact that the information is not averaged in a certain volume. On the other hand, the maximum particle density that can be used before the images are

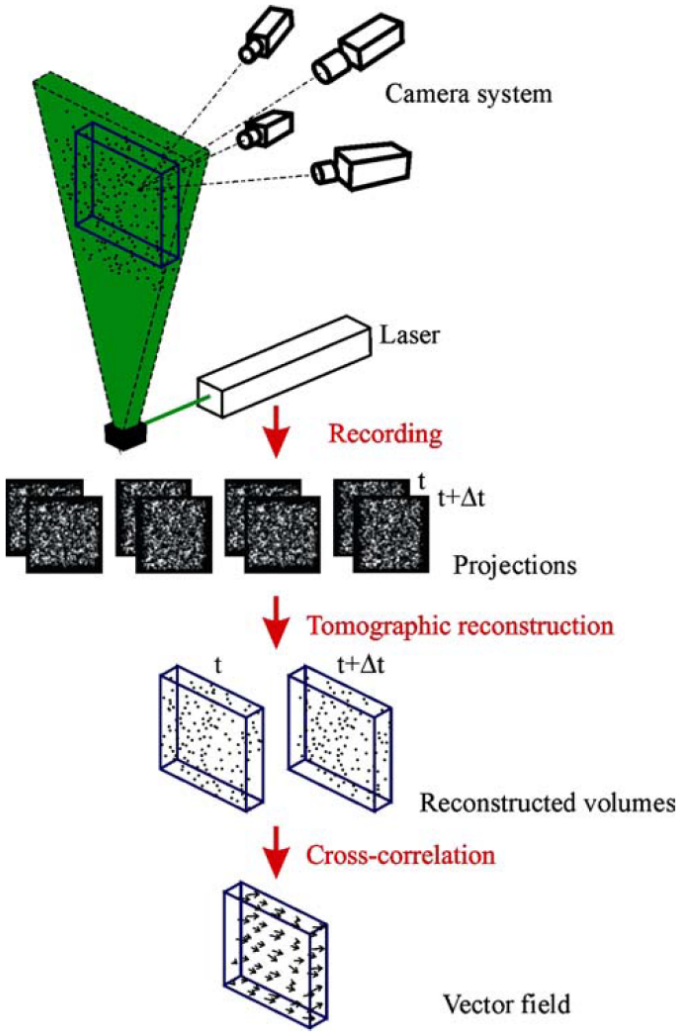

Figure 3.2: Working principle of Tomo PIV [33]

saturated and particle-pairing becomes unreliable is an order of magnitude smaller that with tomo PIV. Looking at the captured images, the highest particles per pixel ratio that can be supported by tomo PIV is approximately 0.05 [71]. In the case of PTV, the ppp value reduced to 0.005 [52] to keep a robust process that does not compute a large amount of ghost particles. This was indeed the case before 2013, when the IPR method appeared which raise the acceptable ppp to 0.05 [83].

The main difference between PIV and PTV, as the name implies, is that the algorithm used to compute the velocity of the flow, instead of discretizing the measuring volume into several interrogation windows, detects each particles individually and follows its path from one image to the next. So the reconstruction of the flow is particle-based instead of voxel-based. The information about the location of each particle is saved through time in a Lagrarian way. Most of the methods created following this approach have obtained an increase in computational efficiency [63]. However the majority take each instant separately instead of taking the information from previous time-steps to search for the particle on the sequential time-step. This idea has been implemented in the tracking algorithm called Shake-The-Box (STB) that is highly reliable and efficient. With the information of the location of the particles along time, a second order polynomial fit is used inside the algorithm to compute the velocities of the particles [74]. This technique is several orders of magnitude less demanding in terms of computational time than the regular tomographic PIV technique. It was introduced by Schanz et al. in 2013 [73] and it is currently considered the cutting edge technology in its field. The STB algorithm will be used during the present work.

3.2.3. Large scale PIV - helium filled soap bubbles

Regular tomo PIV is a technique limited by its high computational cost and its inability to measure large volumes. The first aspect has been outperformed by PTV algorithms such as STB. In the case of the second issue, the size of the volume is restricted by the high intensity light source that needs to be used to collect enough scattered light from the tracer particles so the particles can be distinguished by the cameras [72]. With the current hardware technology the intensity of the light that can be provided by a laser head has reached a limit. This implies that if the light needs to be spread to a larger volume, the intensity of the light will decrease. The only way therefore to be able to capture the particles with the cameras is by increasing the scattering factor of the particles. This can be achieved by enlarging the particles.

However, if the particles are larger, then it may be possible that they do not follow as accurately the flow anymore. The main requirement of any tracer particle in PIV is the ability to follow correctly the flow. This means that the particles need to be able to adapt to drastic changes of flow conditions with a smaller reaction time that the physical behaviour that is being studied. To evaluate such capability, the slip velocity or velocity lag is computed. Assuming that the particles are small and spherical and that viscous forces are more influential than inertial forces (creeping flow, $Re << 1$), then the slip velocity is defined as [64]:

$$U_s = d_p^2 \frac{(\rho_p - \rho_f)}{18\mu} \frac{dU}{dt} \tag{3.3}$$

where d_p represents the diameter of the particle, the dynamic viscosity is expresed as μ and the densities of the particle and the fluid are ρ_p and ρ_f, respectively.

It can be easily concluded from the formula that the larger the particles, the larger the slip velocity and therefore the reaction time of the particles becomes larger. However, there is another term in the expression which relates to the density of the particle with respect to the one of the fluid it is moving with. If the particle has a density close to the one of the fluid, the slip velocity will decrease. A trade-off can be found between density and size of the particle.

Following this path of reasoning, the Helium Filled Soap Bubbles (HFSB) were introduced [72]. These particles have a density very close to the one of air. The soap used is indeed heavier than air. It is composed by water, glycerine and soap, this mixture is called bubble fluid solution (BFS). But if inside the bubble the fluid is lighter than air (such as helium) then the overall density remains near the target value. These bubbles are therefore nearly neutrally buoyant in air. The response time of the HFSB has been observed to be approximately $\tau_R = 10\ \mu s$ [72]. In figure 3.3, the study of the reliability of the HFSB to follow the flow around a cylinder is compared to the use of micro-sized fog droplets, which are the regular particles used for PIV. Several different proportions of helium and soap are analyzed. It can be seen how the HFSB follow closely the path of the droplets validating in such a way their traceability.

The bubbles are generated through a nozzle, creating a small jet stream of particles. The bubbles are generated by injecting the soap with pressurized helium. When the bubbles have been formed, the pressurized air pushes the bubbles outside of the nozzle. Several of these nozzles are placed in an aerodynamic rake to be able to seed a large volume. Depending on the flow rates that are selected for the three quantities: air, helium and BFS, the bubbles will vary in size and number. Their capacity to follow the flow can be slightly altered as seen in figure 3.3. The average diameter of these bubbles is approximately $300\mu m$, which means 300 times larger that regular PIV particles such as droplets. As a consequence, these particles scatter of the order of $10^4 - 10^5$ more amount of light that regular PIV particles [15].

3.3. Robotic Volumetric Velocimetry

Robotic Volumetric Velocimetry exploits a combination of the previous state-of-the-art approaches that have been mentioned. It allows measurements of the three components of velocity in a large volume of the order of several liters [45]. The measurement system (Coaxial Volumetric Velocimeter, CVV [75]) makes use of a coaxial arrangement between imaging and illumination. The use of sub-millimetre diameter Helium Filled Soap Bubbles [72] as tracers instead of micron-size droplets is motivated by the large amount of scattered light, enabling larger scale three-dimensional experiments by quantitative velocimetry techniques. The velocity is computed by means of a PTV algorithm and the complete system relies as well on robotic actuation to position the measurement system.

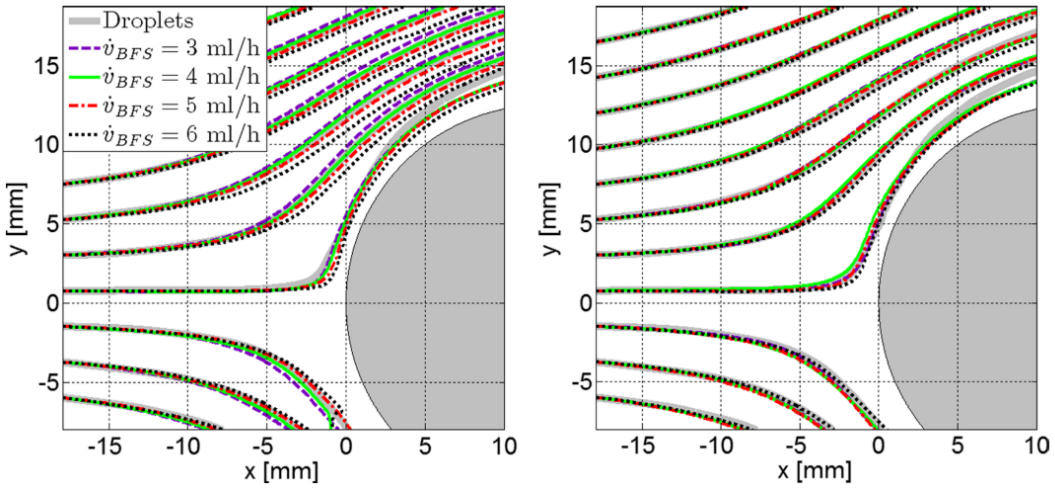

Figure 3.3: Time averaged streamlines determined by cross-correlation analysis at $U_\infty = 30\ m/s$ obtained with micron-size droplets and HFSB with four different volume rates of BFS and two volume rates of helium: $v_{He} = 4\ l/h$ (left), $v_{He} = 5\ l/h$ (right) [72]

3.3.1. Coaxial Volumetric Velocimetry

Another point in question arising in the use of tomographic PIV is the complexity of the set up of an experiment and the visual access that is needed in order to carry it out, which has not been discussed yet. The Coaxial Volumetric Velocimetry approach aims at solving this issue by reducing the camera aperture (β) quite drastically. The difference between the two set up arrangements can be seen in figure 3.4. The optimal tomographic PIV setup has a camera aperture of approximately 60^o [71], while for CVV it is decreased to 4.3^o [76].

The main principles of CVV become clear when looking at figure 3.4. The four cameras are placed close to each other in a 2 by 2 arrangement. The cameras are tilted with respect to the axis of the probe to achieve the aperture angle along the coaxial direction. In between the cameras, an optical fiber is positioned. The laser light is transported by this fiber optic from the laser head until the end of the optic fiber where the laser light is expanded by means of a spherical micro-lens forming a conical illuminated volume. Apart from the lens at the end of the fiber, the laser light is also expanded by means of a combination of lenses at the beginning of the optic fiber. Apart from the low aperture angle, another main modification with respect to tomographic PIV is the large depth of field (distance between the minimum and maximum depth measured, $z_{MAX} - z_0$).

In dash red lines the final measurement volume for the two techniques can be appreciated. The CVV encounters some challenges compared to tomo PIV due to the low aperture angle and the coaxial illumination. To be able to obtain in-focus images with such deep illuminated volume, small imaging apertures need to be used [76]. This implies that the overall amount of light that is collected by the cameras is reduced. The laser light cone that is formed in this approach has a variable intensity along its path compare to the homogeneous distribution obtained in tomo PIV. The variability of particle intensity throughout the volume increases [76]. This is resolved by the use of HFSB which scatter very efficiently the light. A second issue that needs to be address is the accuracy of the particle positioning. Due to the small camera aperture, the displacement in the depth direction, i.e. along the line of sight, is not well captured (see figure 3.5).

To avoid a large error on the in-depth component, the solution is to increase the sample rate of the measurement. In this way the number of measurements of the same particles is higher and the trajectory is based on more information points. According to Schneiders [76], the CVV approach needs to use ”high-speed CMOS cameras and diode-pumped solid-state lasers operating in the kilohertz range” so that time-resolved measurements can be successfully performed with which the position uncertainty can be compensated.

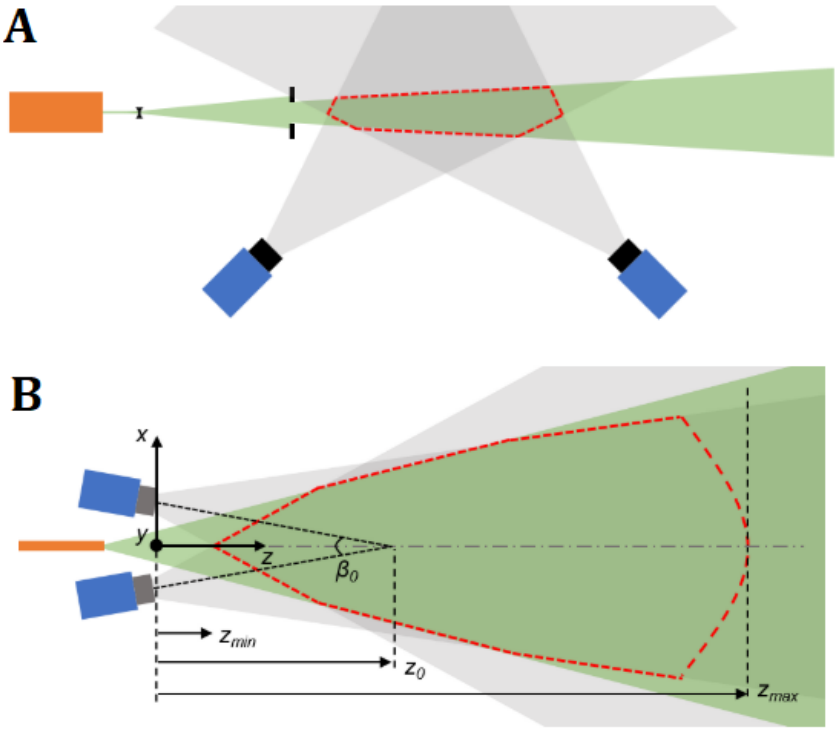

Figure 3.4: Measurement setup for tomographic PIV (image A) and for Coaxial Volumetric Velocimetry (image B), showing the cameras (blue), field of view (grey) and laser illumination (green). In the case of CVV the laser illumination is provided from an optical fiber (orange) [75]

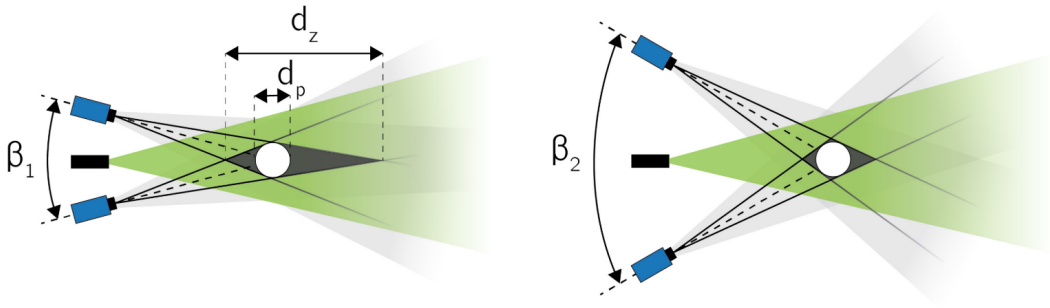

(a) Small tomographic angle β_1. (b) Large tomographic angle β_2.

Figure 3.5: In-depth uncertainty due to tomographic angle β. Reference particle (white) and reconstructed particle (black) [36]

3.3.2. Particle tracking algorithm

The algorithm used is called Shake-the-Box [74] that has been already introduced in section 3.2.2. With the information of the location of the particles along time a second order polynomial fit is used inside the algorithm to compute the velocities of the particles, and potentially also their accelerations. The main advantage of such an approach lies in the considerably less demanding data processing time. Especially for volumetric reconstruction, PTV can outperform conventional tomographic PIV by several orders of magnitude when the computational time needed for obtaining the final velocity field is considered. This allows the user to inspect preliminary results almost in real time while performing the experiment.

The STB algorithm can be divided into three different steps: *initialization*, *convergence* and *converged state* that are shown in figure 3.6. In the first phase, no information of the flow is known so a complete volume reconstruction of the particles in the measurement volume is needed. On the first

time-steps, the particles are then tracked by the IPR method applying a nearest neighbour algorithm which generates the first set of tracks of the complete calculation. The validity of a certain track occurs when it can be tracked for at least n time-steps. So these first n time-steps are the ones that constitute the *initialization* phase. Once there is information about the first tracks of the flow, the *convergence* phase starts. The tracks information from a time-step (i) is used to predict the location of the particles on the following time-step $(i+1)$. The predicted particles are compared to the images from the time-step $i+1$. The particle is then ”shaken” around until the particle predicted and the real one match. Once a particle is paired, it is removed from the frames by means of the residual image so that the rest of the particles can be easily found. At the end from the residual images, the new particles that have entered the measurement domain on that time-step can be determined. As time proceeds, the matching of the images becomes easier to make due to the fact that there is more information in the predictor as the number of particles in each track increases. This is one of the main advantages of the technique. For the last step, when the number of tracks remains relatively constant throughout the time-steps, the $converged\ stage$ is reached. This last phase follows the same steps as the previous one.

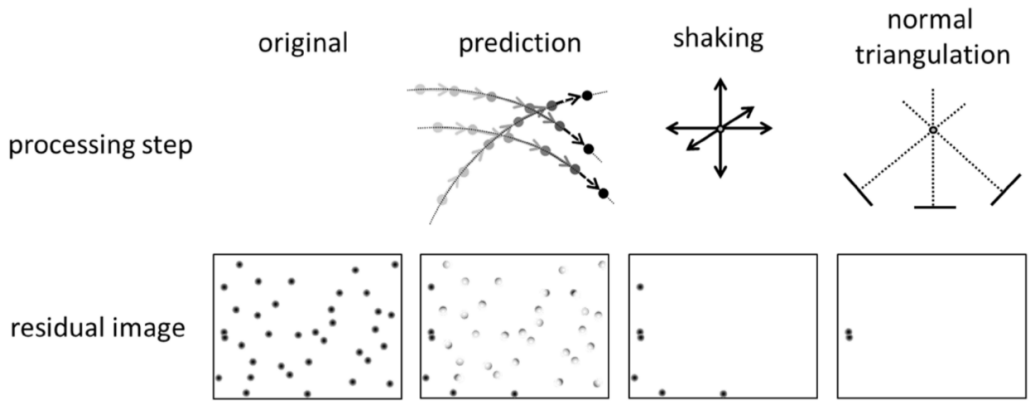

Figure 3.6: Schematic description of the STB procedure in its converged state. Effects of the different computational steps on the residual image of a single camera. [74]

3.3.3. Robotic actuation

In the case of these experiments, the illumination and the coaxial imaging are contained in the same device called the CVV probe. A robotic arm is used to move this device through space. The advantages of this compact and robotically actuated device are mainly the improvement in optical access, the saving in time as only one calibration is needed and the fact that several measuring volumes can be done close to each other in space to have at the end a larger volume. In doing so, significantly large domains can be conveniently studied.

A Universal Robots - UR5 robotic arm is employed to position the CVV probe in space with millimetric precision. It has a maximum reach of 85 cm. The arm has 6 degrees of freedom provided by the six joints that the robot has which can rotate 360 degrees. The robot can be controlled with its own table device or through a computer program where pre-programmed motions can be tested before actually moving the robot.

4

Experimental Set-Up and Procedures

A DelFly vehicle was used as the experimental object in the present study. Wind tunnel experiments were performed in two different campaigns, one with the DelFly model in tethered conditions and another with the complete DelFly vehicle in actual free flight. For the first set of experiments, the selected configurations aim to represent the same conditions as the DelFly would have in free flight, by setting appropriate values of three relevant parameters, which are: the flight speed (U_∞), the flapping frequency (f_{flap}) and the angle of attack (α_b) of the body with respect to the free-stream. The complete setup of the experimental campaign is presented in the following sections, starting with the MAV (Sec 4.1) that has been used and continuing with the different facilities where experiments were performed in section 4.2. To finalize, the complete Robotic PIV system will be presented (Sec 4.3).

4.1. Full-scale DelFly system

The DelFly is a passively stable platform. It relies on its tail for stability and maneuverability. It was primarily design for slow forward flight and it has been seen that there is an important coupling between the vertical motion of the platform due to gliding effect and the pitch angle at which it flies. The fact that the platform is stable and controllable comes with the cost of a large tail which makes the complete system quite sensitive to gusts and it reduces the maneuverability that can be achieved. The effect of the tail will be studied in this project by performing experiments with and without tail. This can be a step forward to the design of tailless FWMAV. For detailed information about the DelFly, please refer to the published book about it [21].

4.1.1. General characteristics

The DelFly MAV used in the experiments is the most recent design. The lay-out and dimensions of the average MAV can be seen in figure 4.1. This MAV consists of a body frame made of a carbon fiber rod. All the other components are attached to this body. At the beginning of the body, the brushless motor that moves the four leading edges of the wings can be found, sustained by the injection model main hinge. The leading edge of the wing is the only part of the wings that is actively moved, the rest of the wing surface moves along with the leading edged made also from carbon fiber. Each wing comes with two stiffeners as shown in section 2.3, that affect the deformation of the wings made otherwise by Mylar foil, $15\mu m$ thick. Linked to the body and the motor, the speed controller is found. All of this electronic components are also bound to the 220 mAh battery. It needs to be taken into account that the center of mass of the DelFly can be extremely sensitive to the position of these components, which makes it almost impossible to have exactly the same DelFly for two different experiments. The manufacturing method has improved during the years in order to make the manufacturing process more accurate and repeatable [37], but it is still prone to errors and discrepancies.

The weight of the DelFly is approximately 25 g and the distance from the leading edge of the wings to the trailing edge of the tail is 21.5 cm roughly. The total span of the wings is 28 cm, while the tail has a span of 17 cm. The tail is painted black for the experiments to avoid unwanted reflections from its surfaces. Unfortunately, this could not be done for the wings of the DelFly as the paint could change considerably the stiffness and the weight of the wings. The laser light reflections from the wings would

present an obstacle in the processing of the images, for this reason the flow around the wings has not been studied.

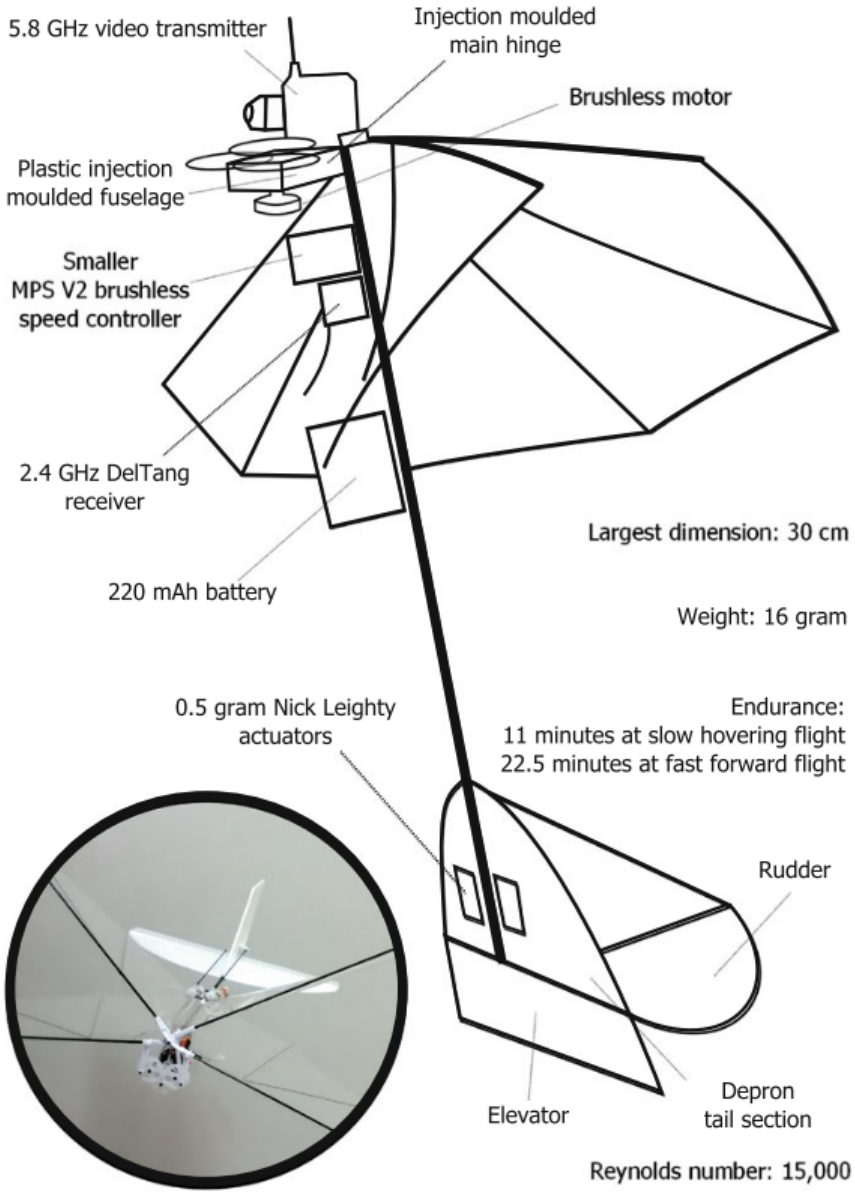

Figure 4.1: DelFly II average specifications for newest design, provided in 2009 [21].

4.1.2. Tethered conditions

The DelFly that was built for the first set of experiments is a simplified version of the regular design. As it can be seen in figure 4.2, the tail can be easily detached from the body in order to perform experiment with and without tail. The tail itself is completely rigid, it does not have control surfaces (rudder and elevator). The DelFly was only meant to be used for the experiments at fixed conditions. It was beneficial to reduce the number of moving surfaces and the complexity of the system too, as no actuators are needed.

The DelFly is positioned in the middle of the wind tunnel, supported by a structure that allows to set the desired body angle of attack (it will be shown in figure 4.4). A Hall-effect switch, installed next to the magnet-equipped output gear of the DelFly gearbox, gave the necessary information about the wing position by providing a pulse signal every flapping cycle. By means of high-speed camera recording, the system was calibrated to know the position of the wings, and hence the phase in the flapping cycle,

when the pulse signal was sent. The power input for the DelFly is controlled to achieve a constant flapping frequency, which is varied from 10 to 13 Hz.

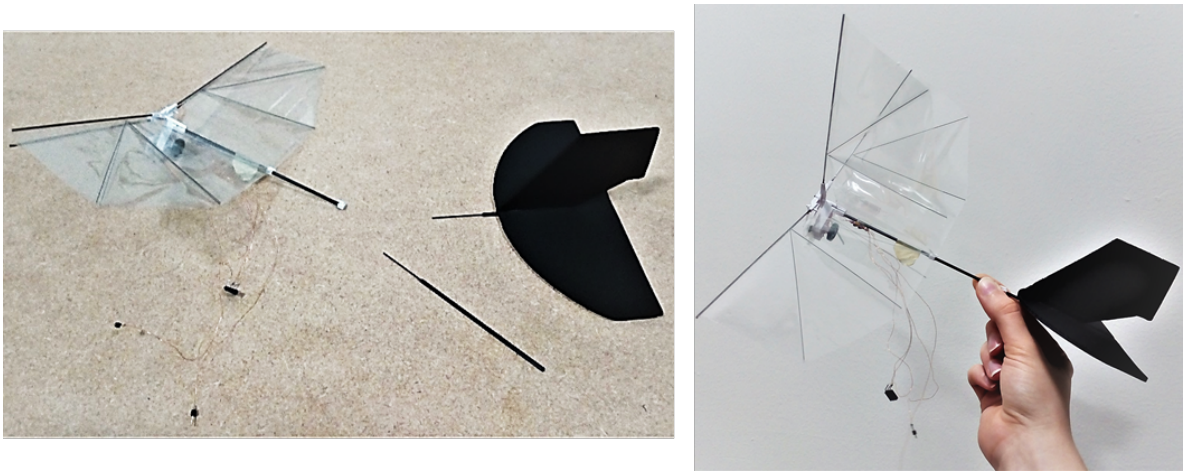

Figure 4.2: DelFly II manufactured for first experimental campaign in tethered conditions.

4.1.3. Free-Flight conditions

The DelFly used in this experiments is the complete system. The same DelFly had been previously used in Del Estal's experiments [22]. Apart from all the electronics needed to achieve control flight, the DelFly is equipped with markers that can be seen in figure 4.3. These markers can be tracked by the optical system used, called $OptiTrack$. This is the approach followed to situate the MAV in space and to be able to control it. The DelFly is not flown manually for this experiment but it relies on an autopilot scheme that corrects the position of the DelFly and aims to keep it in a certain location so that experiments can be performed with the least dynamic effect possible. Markers are also placed in the surface of the wings to obtain information about the flapping motion.

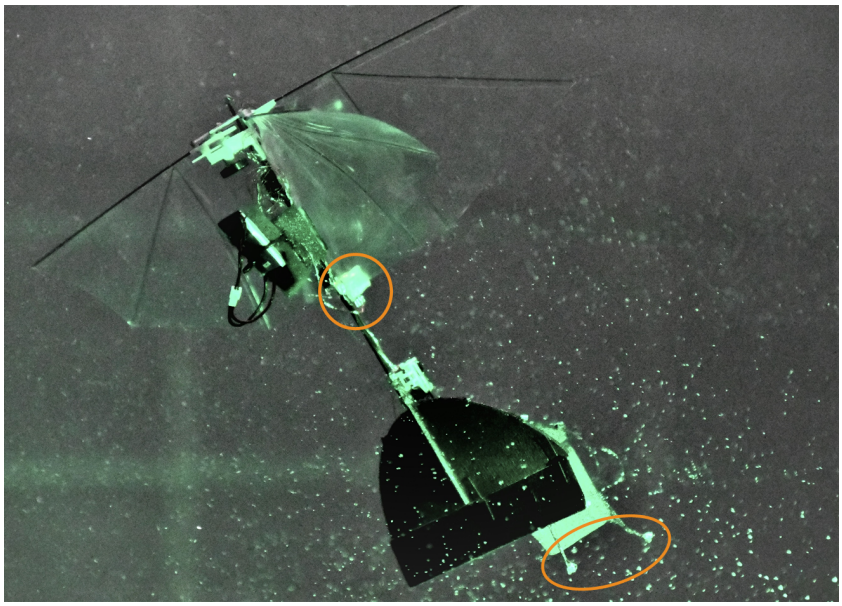

Figure 4.3: DelFly II used for second experimental campaign in free-flight conditions. The circles indicate the position markers places in the DelFly.

The DelFly position is controlled by an on-board autopilot, which steers the vehicle based on feedback from the on-board IMU (used for attitude estimation) and from an external motion tracking system that provides position and heading information (with respect to ground) [10]. The external motion track-

ing system employs 12 OptiTrack Flex 13 cameras (NaturalPoint, Inc., resolution 1280 px × 1024 px, 120 fps). The tracking system data is collected to determine the wing position and the location of the DelFly throughout the measurement with millimeter accuracy. This provides the information on the flapping phase of the wings required in the phase-averaging procedure, while also allowing to apply corrections on the measured data to account for the dynamic motion of the DelFly. More information on the DelFly control system and the data synchronization with the PIV dataset can be found in [47].

4.2. Wind tunnel setup

One of the challenges found when performing the experiments was related to the high turbulence of the flow at low speeds. The wind tunnels used at such low speeds, raging from $0.5 - 2\ m/s$ for this study, are not completely reliable. In order to perform the experiments at the speed desired, preceding PIV measurements were done on the free stream alone to characterize the wind tunnels at low speeds. The work done on this topic is explained with detail in appendix A.

4.2.1. Wind tunnel setup for tethered experiments

The tethered experiments were performed in a low-speed wind tunnel (W-tunnel) at the Aerodynamic Laboratory of TU Delft, which has an open test section with cross-sectional dimensions of $60\ cm \times 60\ cm$ and a contraction ratio of 3.62. The contraction of the wind tunnel with this dimensions was built specifically for a set of experiments of the DelFly in 2012 [30]. The wind tunnel specifications for the new contraction were computed and can be found as well in appendix A. The generator providing the HFSB seeding particles was placed in the settling chamber, upstream of the test section. The measurements were performed at freestream velocities (U_∞) in the range of 0.5–2 m/s. With the mean wing chord length being c = 80 mm, the corresponding Reynolds number (Re) ranges from 2,800 to 11,300. The setup for the tethered experiments is presented in figure 4.4.

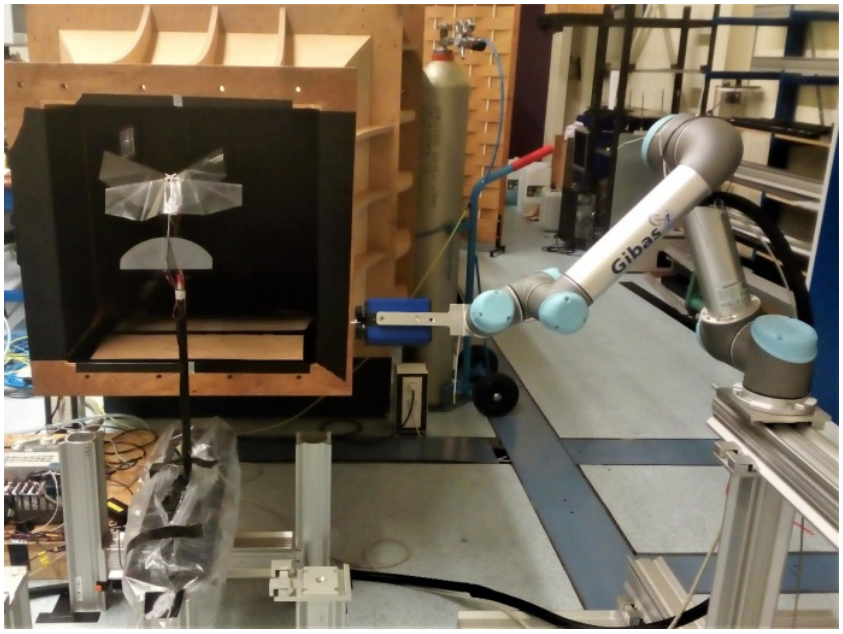

Figure 4.4: Experimental setup tethered conditions.

4.2.2. Wind tunnel setup for free-flight experiments

The second experimental campaign was performed in the Open Jet Facility (OJF) of TU Delft, which is a relatively large-size wind tunnel with an open test section of $2.85 \times 2.85 m^2$ cross section, and a contraction ratio of 3 (horizontal contraction of 1.88 and vertical one of 1.62). The test section leads to an open room that is 8 m high and it extends from 13 m until the flow goes through a cooling mesh at the end of the room and continues the cycle along the closed wind tunnel. The cooling mesh was not used for the experiments. The fan is powered by an electrical motor reaching 500 kW which allows a maximum freestream velocity of 35 m/s. For the OJF facility, the nominal turbulence intensity is

approximately 0.5% [51]. When introducing the seeding rake inside the stream, the turbulence intensity increases to 2% according to Jux [44]. The seeding generator is in this case placed directly after the wind tunnel contraction as can be appreciated in figure 4.5. In the picture it can be observed that the setup of the Coaxial Volumetric Velocimeter (CVV) and the robotic arm is very similar to the one used in the first campaign. The main difference is encountered with respect to the positioning of the DelFly, which in this case is flying in the open test section of the wind tunnel without any support.

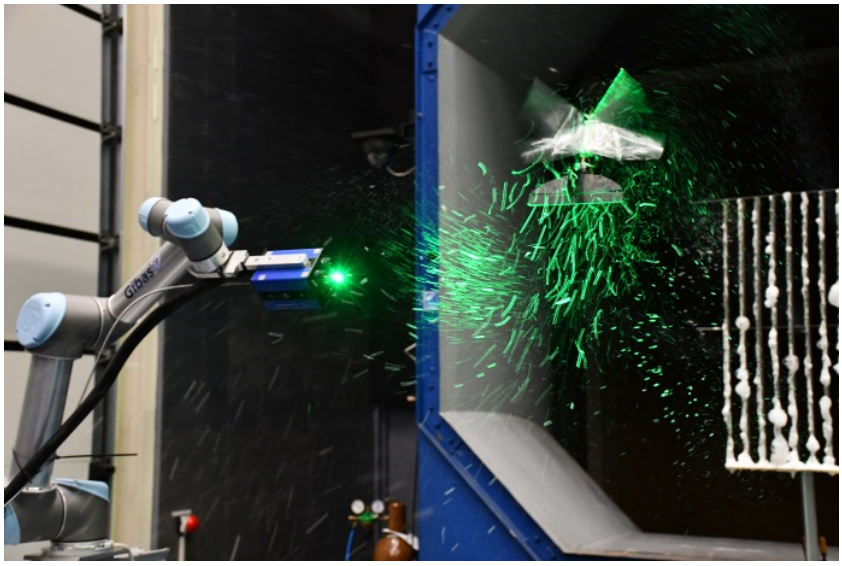

Figure 4.5: Experimental setup free-flight conditions.

4.3. Robotic PIV equipment

The Robotic PIV system is composed of three major parts: the HFSB seeding generator, the Coaxial Volumetric Velocimeter (CVV) [75] and the robotic arm.

4.3.1. Seeding particles

The seeding generator is composed of 10 wings with 20 seeding nozzles each, with a total cross section of $50 \times 100\ cm^2$ and a nozzle pitch between generators of 5 cm in both directions. For the tethered experiments, the seeding generator is placed in the settling chamber of the wind tunnel to minimize the increase of freestream turbulence. After the wind tunnel contraction, the seeded stream-tube covers a region of about $30 \times 55\ cm^2$ all around the DelFly. In the case of free-flight experiments, the seeding generator is placed after the contraction, so the seeded stream tube has a cross-section of $50 \times 100\ cm^2$. Air, Helium and soap are combined together within the nozzles to produce the HFSB. The theoretical maximum rate of production of an individual nozzle is approximately 30,000 bubbles per second [14]. Nevertheless, when working intermediately, the production of a nozzle is close to one order of magnitude less. The three elements: air, Helium and soap, are provided to the seeding rake by means of a system called LaVision Fluid Supply Unit (FSU). The FSU controls the pressure values of the three components which indirectly indicate the mass flow of each component.

In figure 4.6, the two setups of the seeding rake can be appreciated. One of the issues when using the HFSB and the seeding rake is the pollution of the nearby areas due to the adhesion of soap to every surface it comes in contact with. To not damage the inside of the W-tunnel for the tethered experimental campaign, the lower part of the settling chamber was covered with a plastic film and, right under the seeder, a patch of carpet can be seen that absorbed most of the soap coming from the foam production in the seeding rake. The same foam generation problem was expected for the second experimental campaign and so a bucket was placed in between the seeder holding structure and the floor.

One of the particularities of the usage of the seeding rake for these experiments is the low speeds at which it needed to be operated. The nozzles on the seeder produce an approximately constant amount of bubbles per second. If the flow speed is high, then the flow will have the particles quite dispersed and the images taken will not be saturated with particles, usually the problem is that not enough particles can

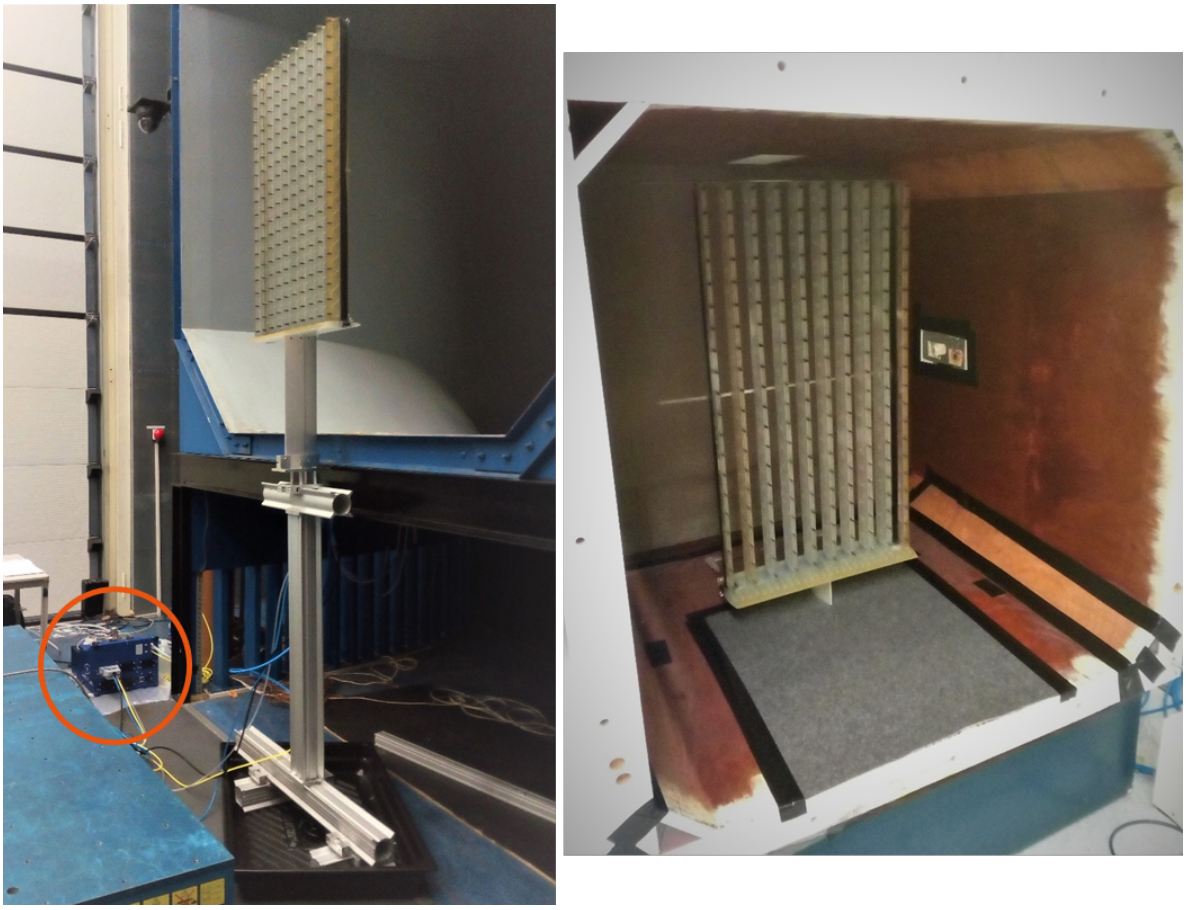

Figure 4.6: Seeding rake setup for free-flight (left) and tethered (right) experimental campaigns. The FSU can be seen in the left figure.

be seen. However in the case of these experiments, the problem is the opposite. Too many particles were generated by the seeder, especially on the first experimental campaign. The approach followed to solve the problem was to tune the pressures imputed on the FSU. The parameter that can be easily played with is the pressure of air. This parameter had a range limitation and its values should vary in between $1 - 4\ bar$. The higher the air pressure provided, the larger the amount of particles generated as the air pressure will push the HFSB away from the nozzle quickly [34]. This also means that the particles are slightly smaller, as they are not ”allowed” enough time to grow larger before leaving the nozzle. If the air pressure is set to a low level, less particles will be generated and they will be bigger. This last one is a good combination for the experiments at hand. But, as not everything could be good, an issue arises when using a low air pressure. The particles are not propelled away from the nozzle which means that part of them will collide with the nozzle itself or with the rest of the structure before it can continue is course on the free stream. The ”failed”bubbles start to accumulate and foam is generated. This phenomenon is enhanced as well by the low freestream velocity that does not help to a great extend to drive the particles away from the seeding rake.

The values of the pressures therefore vary with change in the freestream velocity, but the values used for the two experimental campaign are quite similar. The air pressure ranges from 1.05 to 1.3 bars, while the pressures for Helium and soap remain approximately constant along the experiments with a value of 2 bars for both components.

An attempt is made to calculate the theoretical concentration provided by the seeding generator for the different experimental campaigns. The experiments carried out at the lowest velocity are selected for this computations as they are the most critical cases to check the high concentration of particles in

the measurement volume. The particle concentration as defined by Caridi [14] is:

$$C = \frac{\dot{N}}{A\ U_\infty} \tag{4.1}$$

where the production rate of the bubbles ($\dot{N}$) can be considered as $30000\ bubbles/cm^3$. The cross-sectional area of the seeding rake (A) is potentially the same for both experiments. However, the contraction of the flow before the test section that happens in the first experimental campaign leaves a cross-section area of the seeding volume of $55 \times 30\ cm^2$, while for the second experimental campaign it is $100 \times 50\ cm^2$. Finally the concentration of tracer particles depends of the freestream of the flow as has been pointed out previously. This quantity is defined as $U_\infty = 0.5\ m/s$ and $U_\infty = 1\ m/s$ for tethered and free-flight conditions respectively.

The resultant theoretical concentrations that are achieved are $C_{TC} \approx 73\ bubbles/s$ and $C_{FC} \approx 24\ bubbles/s$ for tethered and free-flight conditions respectively. The theoretical concentration for tethered conditions is quite significant compared to the one at free-flight conditions. The production rate assumed for these calculations is significantly higher than what will occur in reality. This is true for the seeding rake working in standard conditions but this is also enhance by the efforts taken to try to produce less bubbles. Another fact that should be taken into account is the working status of the seeding rake. The seeding rake is composed of 200 nozzles, but only 175 of those were working properly for the experiments.

4.3.2. Camera system and illumination

The CVV system, called *LaVision MiniShaker S*, is composed of four CMOS cameras arranged close together at low tomographic aperture ($\beta_0 = 4^o$). The system is shown in figure 4.7. The dimensions of the CVV probe are: $w \times h \times d = 13 \times 9 \times 8\ cm^3$. The cameras have a characteristic focal length of $f = 4$. The aperture of the lenses ($f_\#$) can vary from 1.8 to 16, however they are usually used with an aperture $f_\# = 8$. The CVV probe is attached to the robotic arm by means of a metallic extension to avoid as much as possible the intrusiveness of the complete system into the flow. It was shown by Giaquinta [36] that the presence of the probe and the robotic arm can alter the freestream and therefore the flow measurement will not be representative of the case of study. However, when positioned properly, the CVV is not supposed to alter the flow in the measurement region.

Figure 4.7: Measurement setup of the CVV probe.

The cameras recorded 8000 images per cone acquired at a rate of 471 Hz at full sensor in continuous mode for all the measurements performed. This is the maximum rate that can be achieved by the system at full sensor which means an image of $800 \times 600\ px$. The images need to be pre-processed

before the particle tracking algorithm can be applied due to the reflections generated by the body and wings of the DelFly. The measuring time per sequence is 17 seconds which corresponds to approximately 200 wingbeats, with 40 images recorded for each wingbeat, assuming a flapping frequency of 12 Hz. The CVV system records images in a conical volume of about 20 cm in height and width, and 30 cm in depth. Five repeated measurements were taken for each conical volume (resulting in 40,000 images in total).

The illumination is provided by a Quantronix Darwin Duo Nd:YLF laser via an optical fiber located in the middle of the cameras which can be seen in figure 4.7. The optic fiber that goes through the entire CVV probe and is connect to the laser head is 4 m long. This means that the laser head can be positioned far away from the freestream to avoid any contamination of the equipment with the HFSB. The light generated by the laser head has a characteristic wavelength of $\lambda = 527\ nm$ and it can emit at a maximum pulse energy of approximately 25 mJ. This can be achieved by the use of the two cavities of the laser at the same time. The usual current setting for these experiments is 21 Amp.

4.3.3. Robotic actuation and robot control

A Universal Robots - UR5 robotic arm is employed to move the CVV position in space with millimetric precision. The robot is depicted in figure 4.8, together with the tablet that controls it. The robot has six joints and it can move freely within an sphere of radius $85\ cm$. It has six degrees of freedom (three translations and three rotations). The end of the robotic arm is called *tool* and it is where the CVV probe structure is placed. The robot is able to know precisely the position of the tool reference frame compared to the base of the robot (the other extremity). The positioning error made by the robotic arm does not surpass $\pm 0.01\ mm$ in translation and $\pm 0.01^o$ in rotation. The base is able to rotate in two directions: in the perpendicular axis to the base plate and in the horizontal direction to rotate the part of the arm attached to the base. The first part of the arm is linked to the second one by another joint that simulated an ”elbow” and that can only rotate in one direction to bring the two components of the arm close or apart from each other. At the end of the second part of the arm, the ”wrist” that is composed by two small elements is found. The first element rotates with respect to the second part of the arm and the other element of the wrist can rotate with respect to the first one.

Figure 4.8: Universal Robot UR5 with control tablet.

In order to measure the entire wake of the DelFly wings, several conical volumes were taken for the same configuration at different locations; the information obtained for the different cones is then combined together with an in-house Matlab code. Four different conical volumes are taken in total which can be seen in the graphical representation in figure 4.9, the volumes are not accurately scaled with the DelFly. The depth direction of the cameras was placed in the spanwise direction of the DelFly, as shown in figures 4.4 and 4.5. The CVV was moved in the longitudinal plane, i.e. normal to the

spanwise direction. One pair of cones was needed to visualize the upper and lower parts of the Delfy. In addition, two consecutive pairs of cones were taken along the body direction of the DelFly to capture the length of the wake. The dimensions of the total measuring volume amounted to $50\ cm \times 30\ cm \times 40\ cm$ (in x, y and z-direction, respectively).

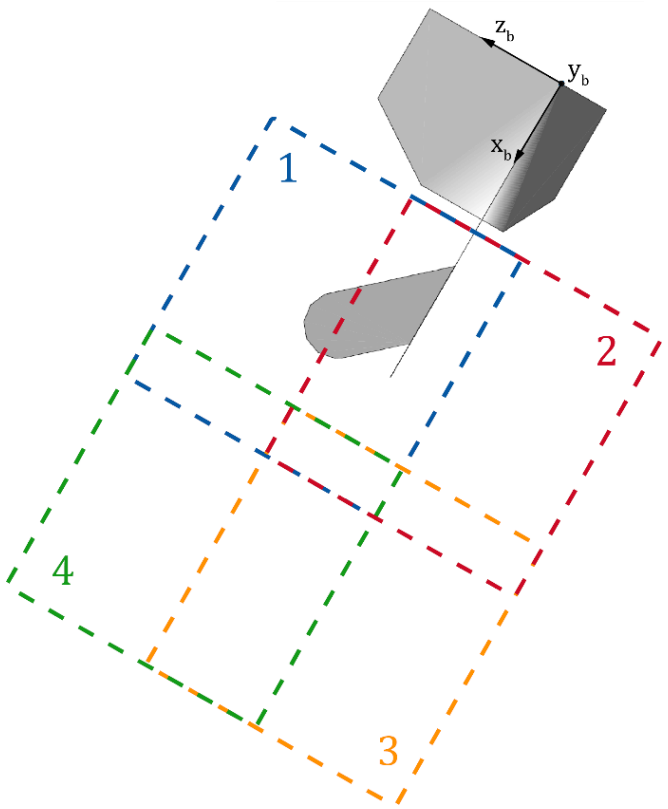

Figure 4.9: Set of volumes that are combined to create the total measuring volume of the experiment.

4.4. System Calibration

4.4.1. Geometrical Optical Calibration

Any PIV system needs to be calibrated before the particles can be measured by it. The calibration to be performed is done by the user once the system is set-up. It is required to perform an optical calibration so that the measurement domain can be mapped from the images taken by the set of cameras. Therefore a geometrical optical calibration needs to be performed with the use of a calibration plate. The one used for this study is a *LaVision - Type 30 calibration plate*, which can be appreciated in figure 4.10. To perform the geometrical calibration, images of the calibration plate are taken and then the points located on the calibration plate are triangulated by the *DaVis* software used (see figure 4.10). The distance between the points is exactly known so the process to map the points back into the images can be performed. Robotic Volumetric Velocimetry takes measurements in a 3D domain so the calibration process needs to be performed at different depth distances from the cameras to map the particles precisely not only for a certain plane, but through out a volume. Once the optical calibration is performed, the system should not be manipulated other than my moving the robotic arm so that nothing inside the CVV probe moves and the optical calibration is not valid any more.

Thus, the CVV probe is place almost touching the center of the calibration plate to mark the distance $z = 0$ from the plate. Then with the use of the robotic arm and the control tablet, the CVV probe is brought backward to the distance $z = 150\ mm$, $z = 350\ mm$ and $z = 550\ mm$ (see figure 4.11). The final maximum positioning error of the camera system after the geometrical calibration is approximately of 0.4 px. An Optical Transfer Function (OTF) is generated to pat the particles from images to the volume [73]. The positioning error quantity in then improved by the used of optical volume self-calibration, starting from the OTF [82]. After the geometrical calibration the system does not need to be recalibrated

anymore and it can be moved by the robotic arm without any issue. Volume self-calibration can always be used to check if the calibration is still good after several days of usage but this is rarely necessary. The calibration error achieved after the volume self-calibration is reduced to 0.1 px.

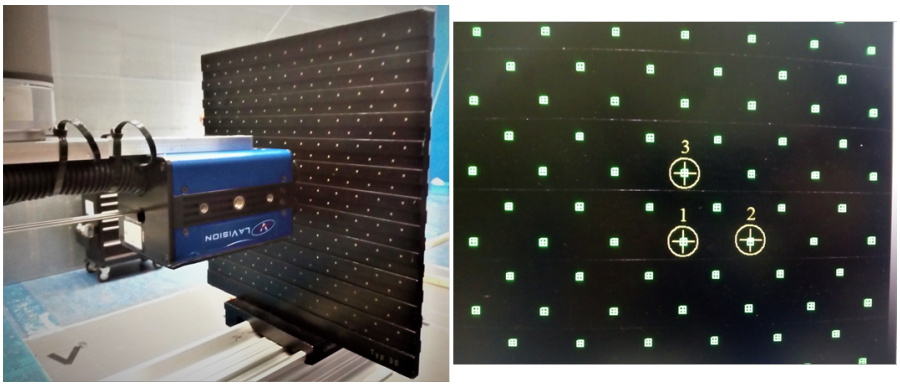

Figure 4.10: Calibration plate attached to a beam to perform geometrical calibration (left) and the detection of the calibrated points of the plate by the software (right).

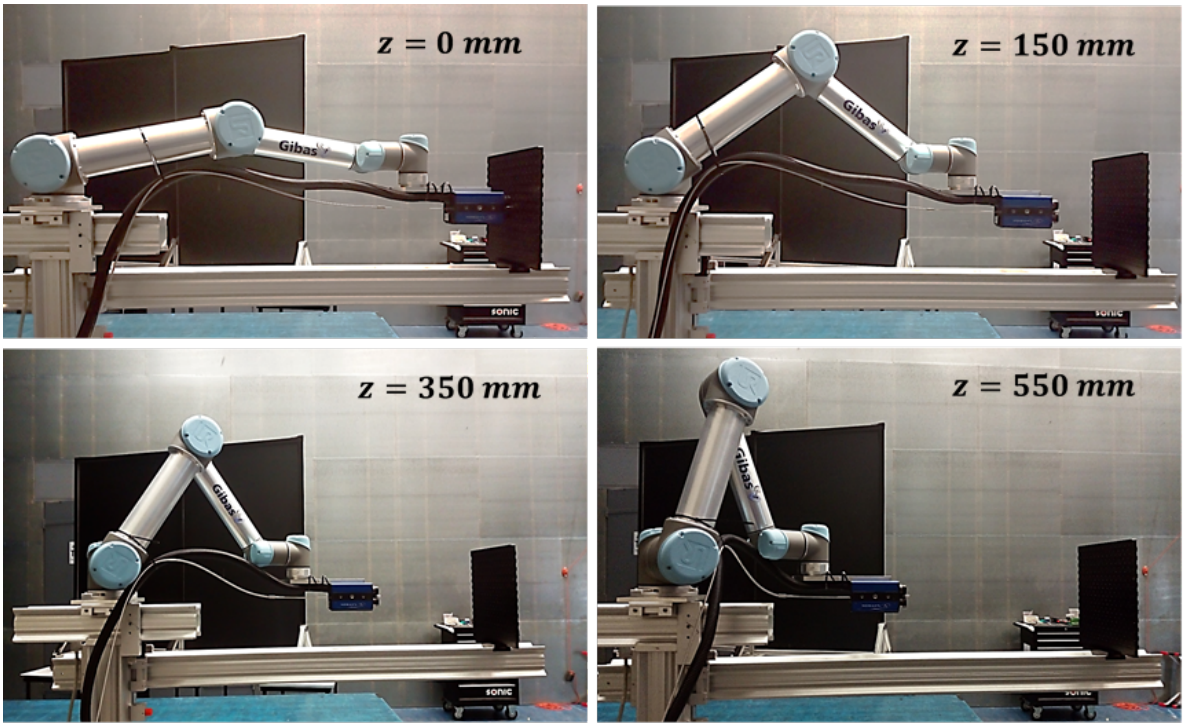

Figure 4.11: Position of robotic arm with mounted CVV probe with respect to the calibration plate for different positions, needed for geometrical calibration.

4.4.2. Robotic Calibration

It has been explained before that the robotic arm is able to accurately know the position of the tool element at any point. From there is would be easy to know the position of the CVV probe. However the link between the physical elements and the optical coordinate system used is still missing. Apart from calibrating the position of the particles in space, the calibration of the reference frame and its distance from the tool reference frame needs to be performed. An approach to measure the distance between the tool reference frame (XYZ_{tool}) and the optical camera reference frame (XYZ_{camera}) is implemented [44]. It consist on taken images of a certain target (in this case consist of a black background with seven white points in the middle) from different aleatory views where the system is rotate in all its axis to assure

a determined position. The white points are triangulated by IPR and their positions are exported into a *Matlab* code that follows an iterative procedure to estimate at the end the origin of the optical reference frame. with respect to the tool. The error that can by embedded into this process can go up to 0.5 mm along in-plane directions while is goes to 2.5 mm on the depth direction as it is the direction with most uncertainty for the imaging system as discussed previously.

4.5. Data acquisition procedure

Once the calibration of both the CVV probe and the robotic arm have been achieved, there is one last step to follow before the experimental campaign can begin. A recording of the freestream is done to check the number of particles in the images and to see if the particles can be tracked. If it is not the case the parameters of the FSU are changed and the process is repeated until a correct situation is accomplished. Also for the first acquisition of the experiment the volume self-calibration is performed. After this process, there are several steps followed in order to acquire the desired data, following the outline below:

1. **CVV probe in place**: the CVV is positioned at the desired place to measure the flow around the DelFly.
2. **Seeding generation and visual inspection**: the HFSB are generated and live recording is used to check visually if enough or too many particles are being produced.
3. **Data acquisition**: One the seeding concentration is checked and the DelFly is flapping the images can be recorded at a rate of 471 Hz for 8,000 images at a time. When performing the free-flight experiments the triggering of the measurement was done when the DelFly seemed to be stable at the desired position for some time, which was monitored in real time.
4. **Data storage and stop of particle production**: the images needs to be stored, which takes around 2-3 min. As several measurements of the same volume need to be acquired, sometimes the seeding generator was not completely stopped but just paused to resume in a shorter time for the following measurement.

4.6. Test Matrix

The experiments performed in this project aim to quantitatively measure the wake of the DelFly flapping wings in regular flight conditions of the MAV. The cases to be studied are selected to cover almost hovering conditions to a reasonably fast forward flight conditions. The DelFly can fly at a maximum of 7 m/s but this is not the regular speed range used in the DelFly, so it is not interesting. In addition, there are also other wake measurements of the DelFly for forward conditions at different reduced frequencies [60], while this is not the case for conditions with high body pitch. It is chosen to perform experiment at freestream velocities: $U_\infty = [0.5, 1.0, 2.0]\ m/s$. When the freestream speed is defined, then the flapping frequency and the body pitch needed to achieve flight conditions for the DelFly are automatically determined. The relation between the three parameters has been extensively studied by Karasek [46]. The resultant values for the different quantities can be found in table 4.1. In this table also the reduced frequency for each configuration is computed to see how it changes significantly within the regular flight envelope of the DelFly.

Configuration	$U_\infty(m/s)$	$f_{flap}(Hz)$	$\alpha_b(°)$	$k = \pi f_{flap} c/U_\infty$	Tail
1	0.5	13	70	6.5	Yes / No
2	1.0	12	45	3.0	Yes
3	2.0	10	31	1.3	Yes / No

Table 4.1: Test matrix for first experimental campaign

The first experimental campaign is done in tethered conditions. In this way it is a possibility to define exact values for the parameters used and it is easier to measure the wake of the DelFly as it is fixed to a certain position. However in tethered conditions, the real fight conditions cannot be completely simulated. The movement of the wings of the DelFly and the periodic forces generated by them create inherent dynamic behaviour of the system and it is also subjected to vibrations. In order to

see if free flight measurements are able to be performed and to try to assess the different between the two kinds of measurements, further free-flight experiments were performed. The main objective is to recreate the same conditions tested in the first experimental campaign so that results can be compared. The experimental setup is practically identical in terms of PIV measurements, however the DelFly is not stationary anymore so the difficulty of the measurements and its post-processing increase. For the second experimental campaign, only the freestream velocity is set to a certain value, the other quantities can vary to meet this velocity. This means that the flapping frequency and the pitch of the MAV can be different from the ones of the tethered campaign. Configuration 1 has a very low velocity that cannot be accurately achieved in the OJF facility, so only configurations 2 and 3 are tested.

Configuration	$U_\infty (m/s)$	Tail
2	1.0	Yes
3	2.0	Yes

Table 4.2: Test matrix for second experimental campaign

5

Data Analysis Reduction Techniques

This chapter summarizes the variety of processes that follow the data acquisition until the final processed data to be analyzed. First, the images need to be pre-processed to remove reflections and noise from the images so the particles can be clearly tracked. Then the particle tracking algorithm can be use to find the particles along the measurement time. Then a further phase-lock averaging needs to be applied to be able to measure the flow behaviour during different phases along the flapping cycle.

5.1. Image Pre-Processing

Before the images acquired can be used in Shake-The-Box, the images need to be pre-processed by means of filters to reduce the reflections and background light. The output of the pre-processing is ideally composed of images only containing nice round particles to track. One common issue of the raw images recorded is the appearance of reflections from the object to be studied. If the reflections are too strong, the image is saturated in that region and no information from particles going through that volume can be tracked. But several filters and processes have been proposed to remove ”weak” reflections and background noise in the image. If this is not done correctly, the STB reconstruction will find false particles that will not behave physically and that will contaminate the measurement for statistical convergence.

One filter that is recently employed in Robotic Volumetric Velocimetry measurements is the third order Butterworth filter, proposed in 2014 by Sciacchitano and Scarano [70]. The main idea behind the Butterworth filter is the frequency decomposition of the intensity of laser light captured by the cameras. The high frequency domain relates to the passing of the particles, while the low frequencies represent the stationary reflections that do not change drastically in a length of frames. These low frequencies are therefore filtered out. This works perfectly when the reflections are stationary, which is usually easily achieved when the models are not moving during the experiments are being performed. This is however not the case for the DelFly, as the MAV is flapping while the flow is measured. The structure supporting the DelFly during the tethered experiments also suffers a certain level of vibrations that have an effect of the flapping motion. For the experiments performed at a lower flapping frequency (configuration 3 with flapping frequency, $f_{flap} = 10\ Hz$), the reflections move slower. This means that they cannot be removed with the regular Butterworth filter. The problem is especially present for configuration 1 (flapping frequency, $f_{flap} = 13\ Hz$). The processing of the images becomes more challenging. The way to proceed is shown in figure 5.1. A Gaussian filter of 3x3 is used to blur to a certain extent the image so the reflections generated by the DelFly and the structure can be detected by the Butterworth filter which is the following step. At last, a subtraction of the average information accounting to all frames is performed to reduce the background noise.

One thing to keep in mind when applying such powerful filtering is the fact that the more filtered the image is, the lower the amount of particles that will remain in the image and that can be tracked afterwards. So the criteria used when processing the images from the set of configurations and experimental campaigns carried out was to use mainly the Butterworth filter and only use the other processes when necessary. From the four volumes measured in the first campaign, only the first two volumes (1 and 2 from figure 4.9) have reflection problems as the other two look at the wake of the DelFly only.

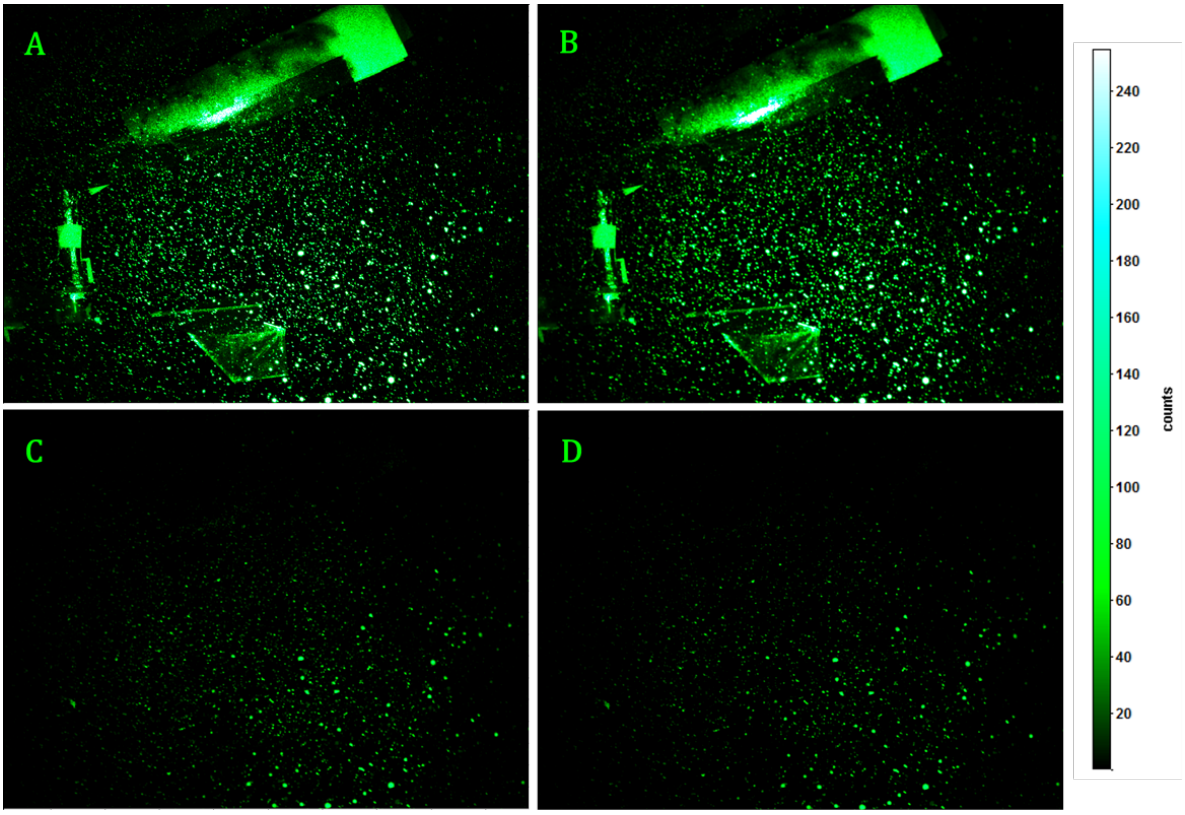

Figure 5.1: Processing steps from raw image (A) to processed image by applying a 3x3 Gaussian Smoothing filter (B), a Butterworth filter with length of 7 recordings (C) and a final subtraction of the average of all images in the measurement (D).

Comparing the images of configurations 1 and 3 in figure 5.2, it can be seen that the seeding concentration is different. As it was explained in section 4.3.1, the particles generated at low velocities ($U_\infty = 0.5\ m/s$) are large and lower in number, while for higher speeds ($U_\infty = 2\ m/s$) the particles are smaller in diameter but the number of particles produced increases. As the particles are bigger, they scatter a tremendous amount of light and this creates the effect that the particles are larger in the images that in reality. Another difference between the two configurations is the position of the DelFly with respect to the structure. The angle of attack for configuration 3 is lower ($\alpha_b = 31^o$) so the DelFly axis does not comes so close to the structure as it does for configuration 1 ($\alpha_b = 70^o$). This leads to more interference of the structure into the flow and it means a great portion of the structure been captured by the images, which of course contributes to larger reflections.

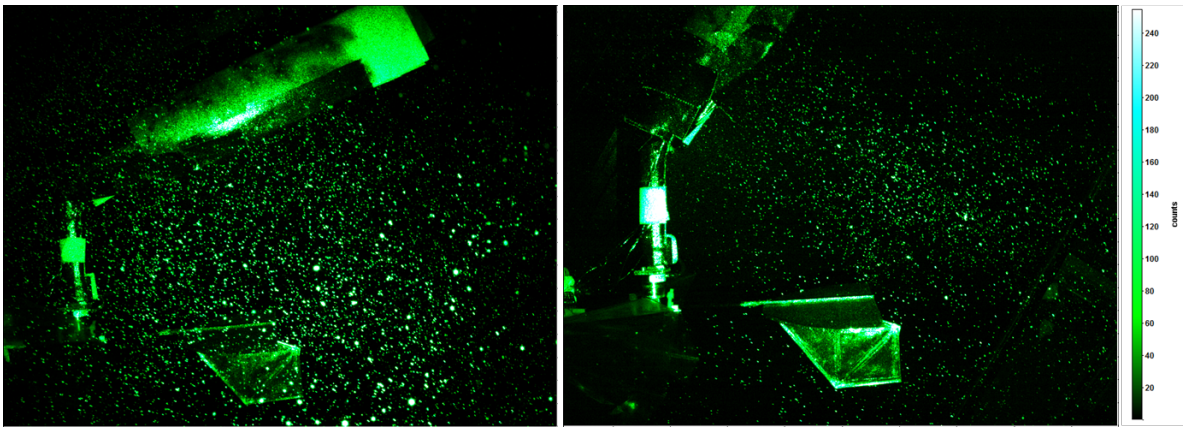

Figure 5.2: Comparison of raw images for configurations 1 (left) and 3 (right) to see the difference in seeding concentration.

Comparing the seeding concentration of the processed images on configurations 1 and 3, it is found that the ppp (particles per pixel) has a value of 0.069 and 0.087, respectively. These values are slightly higher that the optimal ppp for STB tracking algorithm which is 0.05. This does not mean that no particles are tracked, but the probability of also compute erroneous tracks increases so the information retrieve needs to be critically analyzed to avoid invalid results.

5.2. Particle tracking algorithm - STB

The pre-processed images are now ready to be processed with the STB algorithm [74] available in the DaVis version 8.4.0. Davis is the software also used for the recording and pre-processing of the images and it is a product created by *LaVision*. Before the trajectories of the particles, and therefore also their velocities, are reconstructed by Shake-The-Box, several parameters need to be tuned to perform this procedure correctly. The main objective when selecting the STB parameters is to limit the behaviour the particles can have to avoid nonphysical particle tracks and to simplify the detection and tracking of the particles so the algorithm can provide information in a shorter time. If the parameters are not set correctly, then maybe part of the flow features measured is not properly represented and the information will be lost. The STB parameters used for the two experimental campaigns are similar corresponding to the different configurations.

In figures 5.3 and 5.4, the parameters selected for each of the configurations in the first experimental campaign can be found. The first set of parameters (figure 5.3) relates to the main features of the particle tracking that should be defined. The first critical parameter is the *threshold for 2D particle detection* which defines the minimum intensity level that a particle needs to have in order to be tracked. The quantity depends of the level of noise seen in the image. For the present study it was seen how the noise is minimal and so I_{min} has been set to 5 counts. The *allowed triangulation error* is the second parameter of this set. According to Schanz et al. [74], this parameter is advised to the set within the range $0.5 - 1.5$ pixels. The triangulation error selected for these experiments is set to 1.2 pixels. And last but not least, the third parameter to take into consideration is the *maximum particle shift*. This is a key parameter that limits the maximum distance a particles can travel from one time-step to the following one. It is directly proportional to the speed of the flow. For example, in a plane in the middle of the measurement volume at a certain z-location, it can be considered that a millimeter in the physical space is equal to 4 pixels on the images. The distance travelled in pixels of a particle with freestream velocity for the different configuration will be approximately: $d_{px} = [4.25,\ 8.5,\ 17.0]\ px$. As can be seen in figure 5.3, the final maximum shift implemented for each configuration is significantly larger that the distances computed assuming particles moving with the freestream velocity. Apart from the free stream velocity, the flapping wings induce strong velocity fields that need to be taken into account. There is not a clear hypothesis beforehand to give an approximate displacement of the particles due to the flapping motion. This parameter is set by trial and error. It can be seen how the increase of displacement and therefore of flow velocity seems to go up to three time higher for the first configuration and around 2 times for configuration 3. A more detailed analysis about this acceleration will be seen when discussing the results of the measurements.

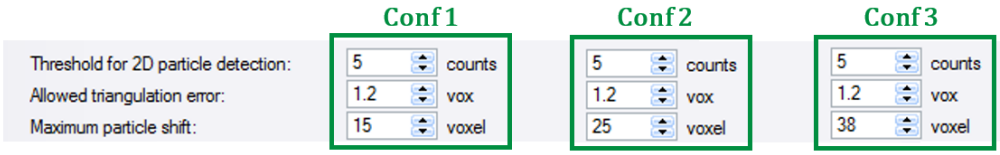

Figure 5.3: Shake the Box basic settings, Davis 8.4.0 LaVision.

Once the main STB parameters are set, more detailed tuning of the STB behaviour can be achieved with the advance settings that comprises the parameters seen in figure 5.4. The only parameter changed from one configuration to the other is the *maximum absolute change in particle shift*. This relates again to the large difference in velocity that is generated by the flapping wings. The acceleration of the particles when closed to the wings can be quite large and in order to capture this behaviour this parameter needs to be adjusted. The acceleration seems to decrease as you advance from one configuration to the next. The acceleration seen is related to the flapping frequency for each configuration which indeed is also higher for the first configuration and is lower for the other configuration in

accordance (table 4.1). The tracks that are computed from the particles are fitted to a polynomial track of second order with a track length of at least 7. This means that the particles need to be tracked in 7 consecutive time-steps to be considered a valid track that will be saved.

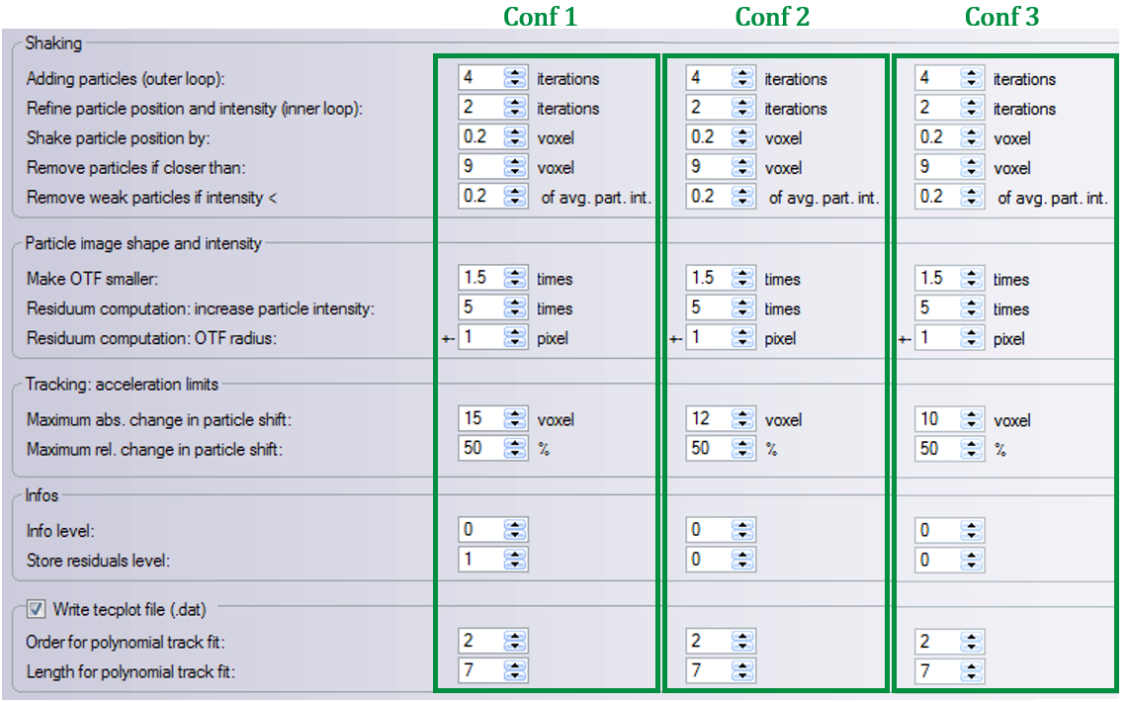

Figure 5.4: Shake the Box window of advanced settings, Davis 8.4.0 LaVision.

5.3. Grid conversion and phase-averaging procedure

The trajectories of the particles, and therefore also their velocities, are reconstructed by Shake-The-Box. The output of such processing therefore is the information of the tracks that the particles have followed though time. The number of particles captured at each time instant is usually not large enough to have good instantaneous velocity fields. Thus, a time averaging needs to be computed to improve the flow information on the volume. The results that are in a Lagrangian representation are also converted into a Eulerian one to obtain a three-dimensional grid that related to the measured volume as allows to easily plot the computed results. Once all these steps are followed, the different measuring volumes taken with the CVV probe can be combined to capture the entire measured flow field.

Due to the flapping motion of the wings, the flow is not steady, but periodic. Hence, the flow evolves through a flapping cycle, generating different vortex structures on the instroke (wings going towards each other) and the outstroke (going away from each other). With the measurement technique used, the evolution of the flow can be obtained by computing the phase-average flow field at different phases of the flapping cycle. This means that the time averaging of the data mentioned above will be performed for each time-step linked to a certain phase of the flapping cycle. Information about the wing position through time synchronized with the recording of the images becomes crucial for the success of the flow visualization. To achieve a better accuracy at each phase, the information from one time-step to the following one can be interpolated to get the information at the right time when the wings are at a specific location. This study is the first implementation of such phase-averaging process from measurements carried out with Robotic Volumetric Velocimetry.

5.3.1. Binnig process

The resulting information acquired from the tracks is unstructured. There are several reasons why it is beneficial to transform it into a structured grid. The way to compute the vector field of this structured grid is by averaging the velocities of the particles passing through each interrogation volumes, also called bins. Similar to what it is done in regular PIV, the interrogation volumes are overlapped to obtain

a higher grid resolution. The number of particles captured at each time instant, and therefore the track density in the measurement domain, is usually not large enough to achieve instantaneous velocity fields with sufficient spatial resolution to resolve the main flow characteristics. Therefore, a time averaging process needs to be applied to increase the density of particle tracks in the measurement domain. The bin size needs to be large enough to have enough particles going through the volume to achieve statistical convergence. According to Agüera et al. [3], the estimation of the uncertainty of velocity for 3D PTV data can be expressed as follows:

$$\epsilon_u = \frac{k\sigma_u}{\sqrt{N}} \tag{5.1}$$

As it could be expected, the uncertainty decreases when the number of samples (N) acquired rises. The number of samples obtained for a certain bin decreases with the third power when the side of the cubic bin is reduced. The number of tracks found is also not constant throughout the measurement volume so the number of samples of each bin will be different. And it can be expected that as the motion of the flapping wings is periodic, the samples taken are not uncorrelated with each other. In fact, due to the phase-averaging process that will be performed, the velocities will be very similar for all time instants for the same phase of the flapping cycle which will lead to convergence being achieved with a lower amount of samples. This will be further discussed in the following chapters.

5.3.2. Phase averaging procedure

Two inputs need to be given in order to be able to provide phase-averaged results. The tracks information from STB process is the first input and the second one is the information about the wing motion. It is not completely necessary to know what the exact position of the wings is, but rather what the periodic motion of it is to be able to divide the flapping cycle at an aleatory point. In the case of the data of these experiments, the phase of the wings is also known apart from the flapping frequency. In the flowchart shown in figure 5.5, the main steps followed in this process are displayed. The desired number of phases to be processed needs to be defined at the beginning, together with the binning specifications (bin size length and overlap). Each phase it treated separately and the complete process needs to be performed for each phase. The first step is to transform the information of the wing position into a time vector where the instants when the wings are at the desired phase are saved. The vectors save the instants with respect to the time-step counting from the PTV measurements to be able to interpolate later from data of one time-step to the next. Thus, it is crucial that the two equipments, 3D-PTV system and the wing position tracker, are linked together so the signal from one can be superimposed with the other.

Once this time information is obtained, the location and velocity vectors of each particles are extracted from the time-steps selected. Within this process, an interpolation is implemented to compute the velocities and positions of the particles at the exact wing position, not just at the nearest measurement point. In order to interpolate the tracks, the polynomial fit used by the STB algorithm is recomputed from the resultant particles on the track. After all the particles are localized and their velocities are know, the binning process can start. The final averaged information is saved and can be later combined with the rest of the phases. The behaviour of the flow through the flapping cycle can therefore be studied, always bearing in mind that the flow fields are averaged.

5.4. DelFly information

5.4.1. Force measurements

During the first experimental campaign, the DelFly is supported by an structure. In between the DelFly and the structure, a small balance is placed to measure the three components of forces and moments generated by the DelFly. In this way a link is obtain in between the flow structures along a flapping cycle and the force generation seen through that flapping cycle. The six-component force balance used in the experiments is a ATI Nano-17, which has a resolution of 1/160 N and the maximum forces that can be measured by it are 25 N on the X and Y directions and 35 N in the Z direction. The mechanism records the forces generated at 20 kHz. The balance measured all forces acting on the DelFly, such as gravity. In order to measure only the aerodynamic forces, the balance is referenced to zero before each measurements so the delta seen by it is the isolated effect of the flapping wing mechanism.

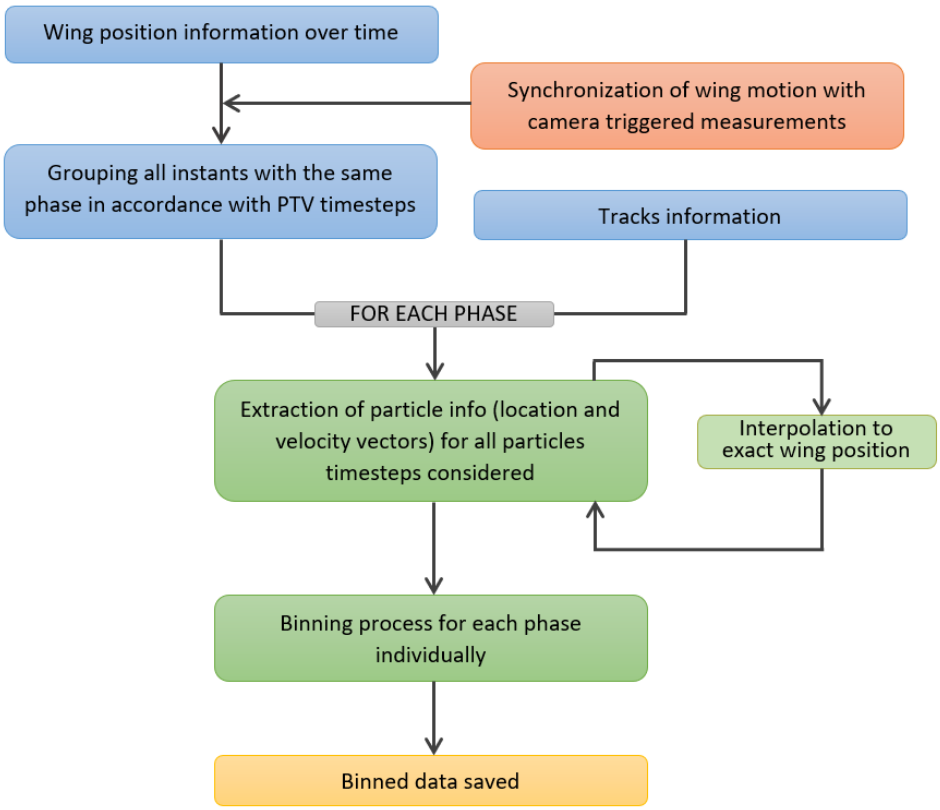

Figure 5.5: Phase average process implemented from 3D-PTV information.

5.4.2. Controlability and syncronization

The way to control the behaviour of the DelFly and the approach to synchronize the wing motion together with the PTV measurements have different strategies for the first and second experimental campaigns. Thus hereafter the topics will be presented separately for one and the other.

First experimental campaign

The DelFly flapping frequency is maintained constant by a speed controller with the help of the information obtained through the rotor pulses generated by the gear mechanisms and the Hall sensor positioned in the gear box as well. The speed controller is linked with the balance system and with the computer that controls the global behaviour of the DelFly. The computer is also linked to the recording unit of the force balance measurements.

When recording the data during the experiments, there is another signal that needs to be saved. This signal is the triggering command send to the recording cameras during the measurements. This signal is composed of small high voltage steps where each of them represent the triggering to record a new frame on each camera. From this triggering signal, the start and finishing of the PTV measurements can be correlated with the wing positions and each PTV time-step is related to a certain phase over the flapping cycles.

Second experimental campaign

In the case of the second experimental campaign, the quantities that are controlled are the three components of displacement of the body with respect to a target location. The flapping frequency and body angle will be adapted accordingly to adjust for the freestream generated on the wind tunnel. The wing motion is measured by the OptiTrack system used. The way this information can be synchronize with the PIV measurements is by means of an external triggering device that send the starting signal for the PIV measurements at the same time that is lights up several LEDs of a simple breadboard. The illumination of the small LEDs is captured by the camera system and the start time of the flow measurements is captured.

5.5. Characterization of vortex structures

Once information is finally processed, the output data files can be loaded into *Tecplot* to display the resulting flow behaviour. In order to see what vortex structures are generated by the MAV, the information should be studied. The first way to check that indeed there is some flapping behaviour is check the periodicity of the changes in velocity along the different phases. The flow should be accelerated in the body direction at some instants while in others it should not. As the DelFly will be at a certain angle of attack, this acceleration regions could be observed both in the streamwise component and in the vertical component (X and Z directions). Apart from the velocity, vorticity plots can also be obtained. This can help to understand the flow behaviour, however a region of high vorticity does not directly imply the presence of a vortex structure.

The vortex-identification technique that will be used is called Q-criterion [42, 43]. The method identifies fluid regions with vorticity, called ”eddies” by calculating the value of the second invariant of the gradient of velocity called Q which follows the expression below:

$$Q = \frac{1}{2}\left(||\Omega||^2 - ||\mathbf{S}||^2\right) \tag{5.2}$$

where $||\mathbf{S}||^2 = tr(\mathbf{S}\mathbf{S}^t)$ and $||\Omega||^2 = tr(\Omega\Omega^t)$. The first term of Q is usually referred to as the anti-symmetric part (Ω) where $\Omega_{ij} = \frac{1}{2}(u_{i,j} - u_{j,i})$, while the second one is the symmetric part ($\mathbf{S}$) where $S_{ij} = \frac{1}{2}(u_{i,j} + u_{j,i})$. The first one relates to the shear strain rate of the flow while the second one relates to the magnitude of the vorticity.

Once the vortex is located in the measuring volume, it is quite useful, especially for this application, to colour the Q-criterion iso-surfaces with the value of vorticity on the direction of the rotation of the vortex. In the case of flapping wings, courter-rotating vortices are expected to be shed by the upper and lower wings on each side and also the vortices should have opposite sign during the instroke and the outstroke.

6

Preliminary Tests

The technique to be used for the experiments of this project has never been used with moving objects that create unsteady flows. Therefore, it was reasonable to carried out a simple preliminary experiment before the actual experimental campaigns to verify that the flow can be accurately measure by Robotic Volumetric Velocimetry. The preliminary measurements provided the opportunity to implemented and check the data processing tools that had to be generated in *Matlab* in order to perform the phase-locked averaging process.

6.1. Setup and data analysis

The set-up of the experiment is quite simplified. The DelFly is placed in the middle of the HFSB stream on the OJF wind tunnel which is used as well for the second experimental campaign. The DelFly is placed in the same support structure as in the first experimental campaign, but maintaining a zero angle of attack with respect to the freestream. A picture of the experimental setup can be seen in figure 6.1. The flapping frequency of the DelFly is not controlled by a speed controller, but by a simple power input valve that restricts the power signal provided to the DelFly motor. It is therefore directly related to the flapping frequency. A calibration of such relation between input power and flapping frequency was completed before the experiments in a still air environment. It was found later that the aerodynamic forces enhance the flapping motion and therefore the resultant frequency of the measurements increased with respect to the intended one. In order to find the right flapping frequency value of the measurements after they were carried out, the streamwise velocity component after the DelFly is studied. A cyclic acceleration and deceleration pattern of the velocity should be captured on the wake of the flapping wings which should have the same frequency as the movement of the flapping wings themselves. An autocorrelation of the velocity vector on a small volume of the wake is performed to give as a result a flapping frequency of approximately 12 Hz. The freestream velocity during the experiments was set to 3 m/s, so the reduced frequency of the flapping motion is $k = 1.01$.

For the visualization of the data that will be shown in the following section, the measured volume has been divided in interrogation volumes or bins of size 30 mm with an overlap of 75% which as a result leads to a pitch of 7.5 mm. When doing the phase-lock averaging process, the time-step interpolation to get a more accurate location of the particles at a certain phase was not yet implemented at this stage of the project. This means that the results shown in this chapter have been computed by looking at the closest time-step measurement found, no interpolation was performed. The error therefore can be up to half the time difference from one measurement to the next. As the recording frequency is 471 Hz for this experiment, the maximum error that could have been introduced in the measurements is of 1.06 ms. It is taken into account that the angular velocity ($\dot{\phi}$) of the wings is described by:

$$\phi(t) = \Phi cos(\omega t) \longrightarrow \dot{\phi}(t) = -\phi_{max}\omega sin(\omega t) \tag{6.1}$$

where the angular frequency is $\omega = 2\pi f_{flap}$ and the stroke amplitude is Φ. The maximum angular velocity that can be therefore achieved with a flapping frequency of $f_{flap} = 12\ Hz$ is $\dot{\phi}_{max} = \Phi 2\pi f_{flap} = 80\ rad/s$. As a consequence, the maximum error in the stroke angle of the wings is approximately 0.085 radians or 4.8 degrees.

Figure 6.1: Experimental setup for preliminary measurements.

6.2. Previous study of wake visualization

The preliminary experiment aims to measure the vortex structures that have been already studied in 2014 by Percin et al. [60]. Percin analyzed the behaviour of the shape and interaction between the vortex structures shed by flapping wings depending on the reduced frequency. The main structures found can be seen in figure 6.2, showing two consecutive flapping cycles that start at the beginning of the instroke. Taking into account that the flow goes into the positive Z direction, four main vortex structures can be seen. The flapping cycle can be divided into instroke, where the wings of the DelFly move towards each other, and the outstroke, when they come apart. The structures seen as generated near the tip of the wings so they are called tip vortices. The tip vortices generated by the upper and the lower wings have a mirrored shape and same magnitude, but the vorticity of each has the opposite sign to the other. During the instroke, the tip vortices start far apart and they come closer as the wings do. When the wings are completely closed these vortex structures disappear and the outstroke start that generates tip vortices of the opposite sign. The tip vortices of the outstroke extend further apart from each other following the motion of the wings. The sign of the vorticity relates to the wing motion with respect to the freestream. Looking at the upper wing, when the wing is displaced downwards the local angle of attack seen by the wing is positive. This means that the lift generated by the wing is positive and, according to simple lifting line theory, the tip vortex generated will also have a positive sign. When the wing goes upwards, the angle of attack seen is negative, which means negative lift and a negative vorticity being generated. The same reasoning but in the opposite direction can be done for the lower wing. The flow structures are symmetrical with respect to one another because the angle of attack of the DelFly body is zero and so the local angle of attack of the flow seen by upper and lower wings is the same.

The PIV experiments carried out by Percin et al. were performed with the stereo-PIV technique. In order to reconstruct the wake structures in a volume, Taylor's hypothesis is used. The wake structures are assumed to travel with the freestream velocity, but this may not be a valid assumption for flapping wings. Proof of the questionable physical application of the Taylor's hypothesis in the wake of flapping wings is indeed shown by the work of Bomphrey et al. [11]. This issue is therefore the mayor source of difference between the measurements performed by Percin and the experiments done using Robotic Volumetric Velocimetry as the complete wake without any assumption is captured by the latter. However, reasonable similarities between the two experiments should be found. In this case then the Robotic Volumetric Velocimetry is validates and it can be applied as a measurement technique for the rest of the project.

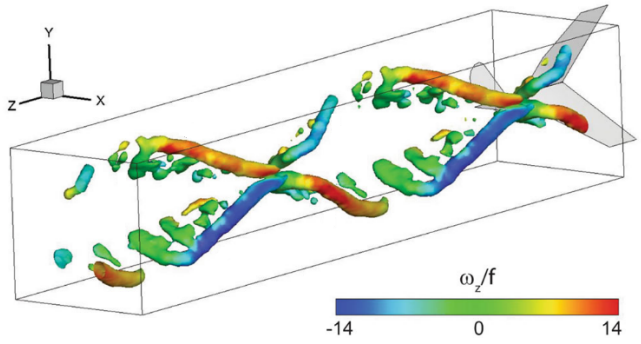

Figure 6.2: Perspective view of the wake structures visualized by isosurfaces of $Q = f_{flap}^2 = 10$ and colored by ω_x/f_{flap} for two periods of the flapping motion (flow is the positive z-direction) for the case of $k = 0.47$ ($U_\infty = 3$ m/s and $f_{flap} = 5.7$ Hz) [60].

6.3. Comparison with results of preliminary tests

To have a first view of the comparison between Percin's experiments and the preliminary results of this project, it is useful to look at the side and bottom views of the wake. The results should be compared with the same reduced frequency. Unfortunately this is not possible as there is no experiments in the literature performed at $k = 1.01$. The closes experiments ($k = 0.94$ and $k = 1.17$) will be use for the comparison. The wake structures are visualized by plotting Q-criterion isosurfaces. The value used on the preliminary measurements is $Q = 1450\ s^{-2}$ (for more details about the Q-criterion, please refer to appendix B). It needs to be pointed out that the vortex structures on the preliminary experiments are colored by $-\omega_x$ so that the signs of the vorticity agree with the ones seen in literature.

6.3.1. 2D wake topology

The side view for both sets of information can be found in figure 6.3. It can be seen how only part of the wake of the DelFly has been captured on the preliminary experiment. Only the lower side of the DelFly is properly measured. Looking at the information measured spanwise (see figure 6.4), the vortices generated by the right pairs of wings are measured, the right pairs of wings is also the one studied by Percin so the comparison can be directly performed. The tip vortices generated by the instroke and the outstroke can be clearly identified. The outstroke vortices have a round *C* shape numbered 3 and 4 by the literature shown in figure 6.3. The instroke vortex structures according to the literature should have an arrow shape. However the instroke vortices that are seen from the preliminary measurements are quite close together and they are both deflected downwards with respect to the DelFly body. Thanks to the fact that they are deflected, the vortex from the upper right wing was captured on the instroke, which is not the case during the outstroke. There is also a more clear interaction between the vortex structures themselves along the convection of the wake with the freestream. It can be seen in the left plot of figure 6.3 how the end of the vortices of the outstroke is closer to the DelFly than the beginning of the following instroke structures. This kind of behaviour could have never been seen using Taylor's hypothesis. The same happens with the deflection of the vortices downwards. The only displacement of the vortex structures allowed by Taylor's hypothesis is the displacement in the X component, on the direction of the freestream. It is safe to conclude that the wake structures are highly influenced by induced velocities generated by the vortex structures themselves and the accelerations generated by flapping wings too. Another reason for the deflection of the instroke wake structures may be due to the presence of the tail of the DelFly. The stereo-PIV measurements by Percin were performed on a plane directly after the flapping wings of the DelFly so the effect of the tail is not studied in the literature in this case. The tail can be also generating forces and therefore causing a deflection the flow. This is only a speculation as it has not been quantitatively assessed in the preliminary tests results.

Apart from the changes in the shape of the vortices, differences in the maximum strength of such structures are seen when comparing the two sets of information. The vorticity in the literature is nondimensionalized by the flapping frequency. If the same is done with the preliminary data, taken a flapping frequency of $f = 12$ Hz, it gives a nondimensionalized vorticity of $\omega_x/f_{flap} = 6.67$. This is less than half what was measured by the literature right next to the wings of the DelFly. As it can be expected, the strength of the vortex structure decreases as they are convected away from the wings.

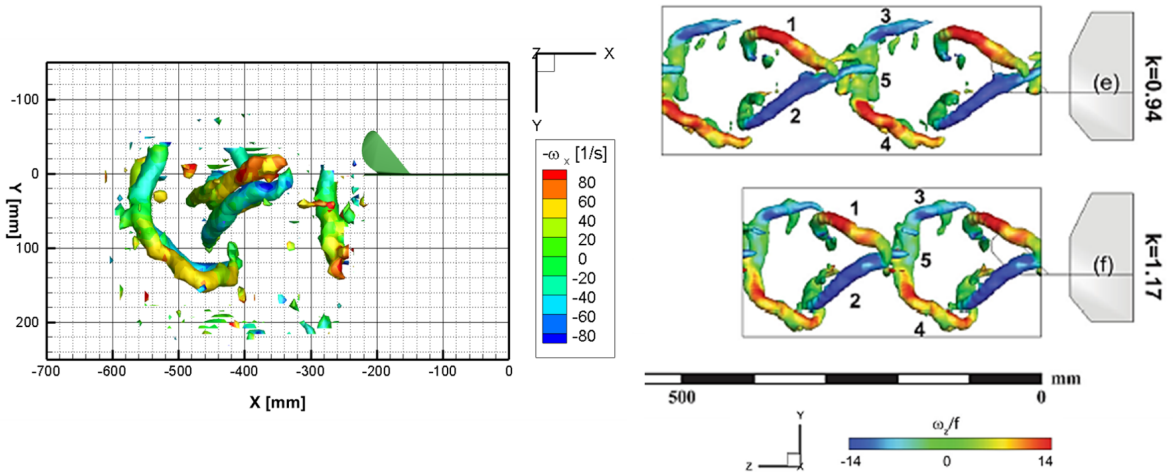

Figure 6.3: XY view of the DelFly wake structures visualized by isosurfaces of $Q = 1450\ s^{-2}$ and colored by $-\omega_x$ (left) and side view of the wake structures (right) visualized by isosurfaces of $Q/f_{flap}^2 = 15$ and colored by ω_x/f_{flap} for two periods of the flapping motion (flow is the positive z-direction) for $k = 0.94$ ($U_\infty = 2$ m/s and $f_{flap} = 7.5$ Hz) and for $k = 1.17$ ($U_\infty = 2$ m/s and $f_{flap} = 9.3$ Hz) [60].

The bottom view for both sets of information can be found in figure 6.4. The symmetry of the flow can clearly be seen in this plot between left and right sides. The vortices are seen to expand more outwards from the DelFly body on the preliminary results while they keep the same distance on the literature results. This is logical as no lateral velocity is accounted for on the wake reconstruction made by Percin.

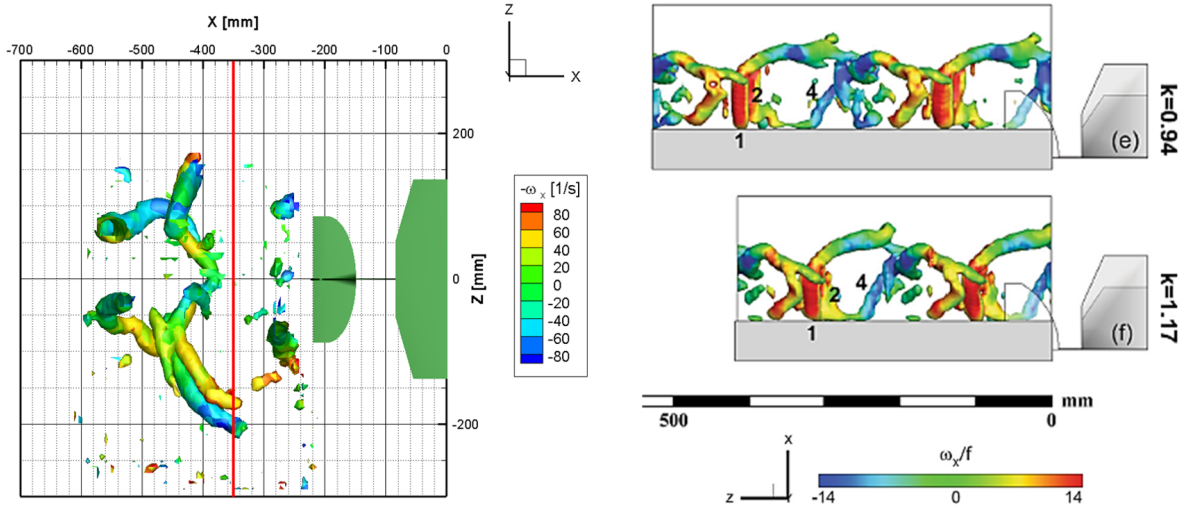

Figure 6.4: XZ view of the DelFly wake structures visualized by isosurfaces of $Q = 1450\ s^{-2}$ and colored by $-\omega_x$ (left) and bottom view of the wake structures (right) visualized by isosurfaces of $Q/f_{flap}^2 = 8$ and colored by ω_x/f_{flap} for two periods of the flapping motion (flow is the positive z-direction) for $k = 0.94$ ($U_\infty = 2$ m/s and $f_{flap} = 7.5$ Hz) and for $k = 1.17$ ($U_\infty = 2$ m/s and $f_{flap} = 9.3$ Hz) [60].

To understand more in detail the velocities induced by the wake structures and the flapping wings, figure 6.5 shows contour plots of the out-of-plane vorticity ω_x and of the velocity component on the Z direction in a spanwise oriented plane at $X = -350\ mm$ (130 mm distance from the end of the tail). The contour plots are selected to show the flow behaviour on the wake generated during the instroke, the position on the plane has been marked with a red line in figure 6.4. On the vorticity plot, shown in the left side of figure 6.5, the two vortex cores of the vortices generated by right upper and lower wings during the instroke can be easily located. The rotation direction, as discussed before, is opposite between the two. When looking at the same region on the plot on the right, an area of negative Z velocity can be

found in between the two vortices. On the other sides of the vortices the Z velocity changes direction and the air is moved in the opposite direction. This is the regular behaviour that could be expected from a 2D vortex. The magnitude of the velocity change is of the order of 0.6 m/s, which is equal to 20% of the freestream velocity. If a mean lateral velocity of $v = 0.3\ m/s$ is assumed, then the lateral displacement seen after $D = 27\ cm$ (distance between end of the wing and measuring plane) will be $d = 2.7\ cm$ ($v/U_\infty = d/D$). If the vortex is assumed to be generated at the tip of the wing, then the vortex at the measuring volume would be located at distance of 16.7 cm from the center line. This is approximately the location of the vortex structure generated by the upper wing. The one generated by the lower wing has drift even further from the DelFly body.

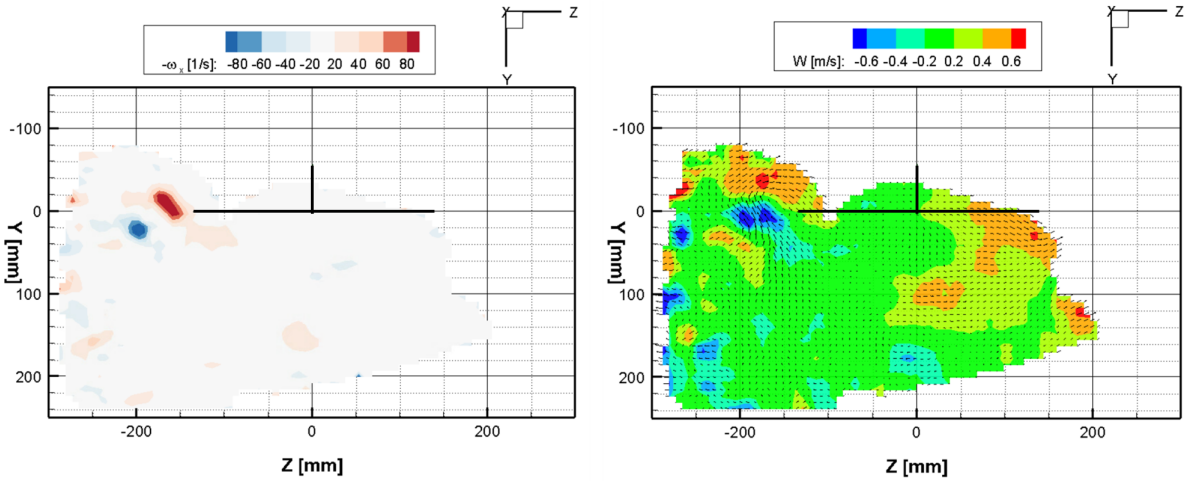

Figure 6.5: Contour plots of the x-vorticity ω_x (left) and the vertical velocity component (right) in a spanwise oriented plane at 140 mm distance from the end of the tail.

6.3.2. 3D wake topology

Looking at a three dimensional view, it is interesting to see what the measurement volume looks like and roughly what its size is. In order to visualize the space measured, it is considered that the actual measurement volume is composed of the region where more that 10 particles can be found. Even with such a small amount of particles, the vortex structures shown before can be observed. The CVV system records images in a conical volume. The conical shape can be clearly seen, concluding that the CVV probe was places on the left side of the DelFly during the experiment. The size of the volume is about 20 cm in height and width, and 30 cm in depth. If placed slightly further away for the DelFly, the complete span of the wings could have been observed.

Finally, the 3D wake structures measured in this preliminary experiment can be visualized in figure 6.7. The wake is composed by several different structures that interact closely with each other and that depend of several factors. Therefore, the wake of a flapping wing mechanism is very complex to characterize. Such spacial representation of the wake evolution can be of help towards the full understanding of flapping wing aerodynamics. From these results, the measurements performed y Robotic Volumetric Velocimetry are successfully validated. Clear wake structures are found which are also present in previous studies. From the time average information, it can be seen how the wake structures are coherently covected through space along the flapping cycle.

In figure 6.7, apart from the large vortex structures that have been discussed previously, several regions with spurious data can be detected, especially near the edges of the measurement volume. This is mainly caused by the low amount of particles that are found in such regions. The measurement performed has clearly not reached statistical convergence and this should be addressed for the two experimental campaigns done afterwards. It is decided to measure each measuring volume or cone 5 times to have enough information along all the domain. Four different cones are taken of each configuration because it has been seen that two cones are needed to see both upper and lower sides of the wake and it will be desired to acquire a larger space evolution of the vortex structures.

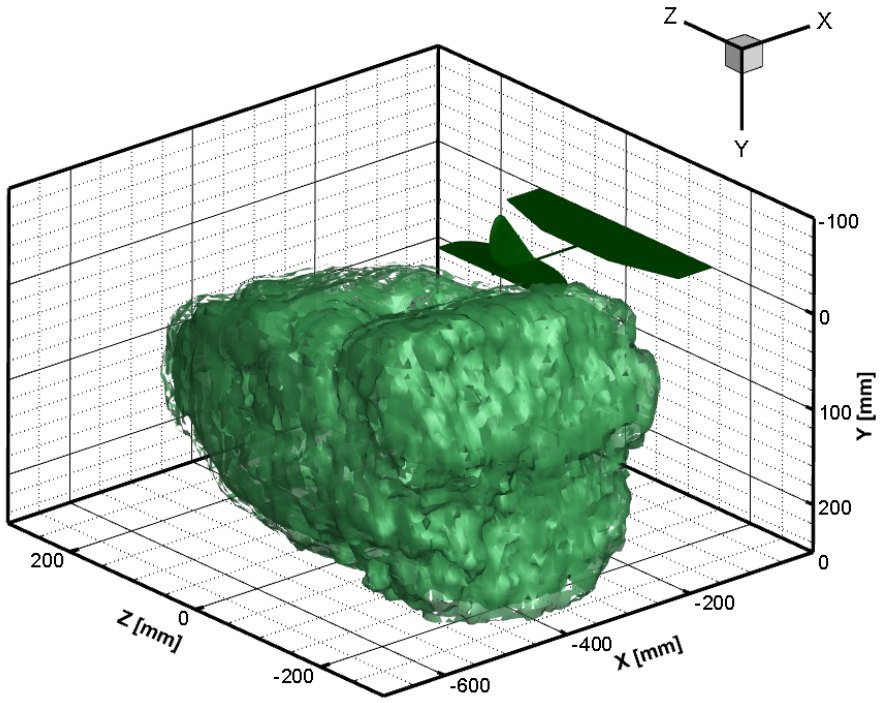

Figure 6.6: 3D view of the measurement volume acquired with the CVV prove on the preliminary experiment.

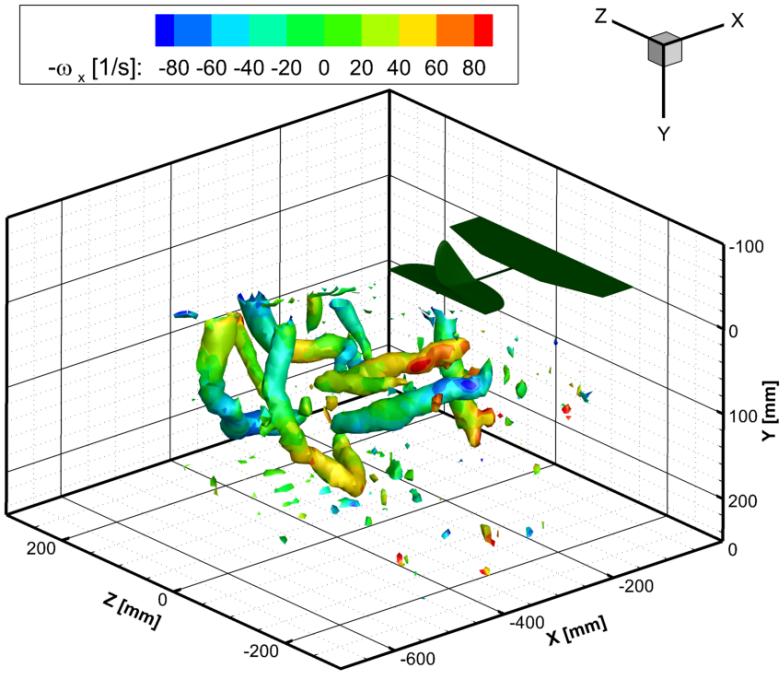

Figure 6.7: 3D view of the DelFly wake structures visualized by isosurfaces of $Q = 1450\ s^{-2}$ and colored by ω_x.

7

Results and discussion

This chapter summarizes the findings and discussions obtained from the different experiments performed, both in tethered and free-flight conditions and with and without tail. Section 7.1 describes the quality of the measurements performed. On the following section (7.2), the evolution of the vortex structures for a complete flapping cycle is explained in detailed for a certain configuration in tethered conditions. Once the main structures are presented, a further study of the effect of the reduced frequency is performed in section 7.3. In section 7.4, the differences observed in between tail-on and tail-off are exposed. Finally, a comparison between the results at similar configurations between tethered and free-flight conditions is made in section 7.5.

7.1. Measurement system performances and information

7.1.1. Final cases measured

The main parameters for each of the considered configurations, labelled from 1 to 3 for convenience, can be found in table 7.1. Three different configurations have been studied in tethered conditions with the tail of the DelFly in place. For the two extreme configurations, measurements without the tail have been also accomplished. During the free flight experiments, the configuration at the lowest speed could not be tested due to inability to generate a steady flow at such slow speeds (0.5 m/s) in the wind tunnel used. The main difference between the free-flight and tethered experiments is the change in flapping frequency that is consistently higher on the free-flight experiments.

Configuration	Experimental conditions	U_∞ [m/s]	f_{flap} [Hz]	α_b [^{o}]	$k = \pi f_{flap} c/U_\infty$	Tail
1	Tethered (TC)	0.5	13.0	70	6.5	Yes & No
2	Tethered (TC)	1.0	12.0	45	3.0	Yes
2	Free-Flight (FC)	1.0	13.0	55.4	3.3	Yes
3	Tethered (TC)	2.0	10.2	31	1.3	Yes & No
3	Free-Flight (FC)	2.0	11.4	30.1	1.4	Yes

Table 7.1: Flight parameters for each configuration and the corresponding reduced frequency

7.1.2. Phases along a flapping cycle

In order to perform the phase-lock averaging process, the phases to by studied need to be defined. It is decided to study eight phases along the flapping cycle with an equal time duration in between them. An illustration of the phases selected can be found in figure 7.1. For the calibration of the Hall sensor (see section 4.1.2), high-speed camera recordings were carried out. These recordings are useful to have an idea of the deformation of the wings. The calibration was performed in still air so the final deformation that will be seen in the DelFly wings during the experiments is probably not the same. However the main trends are valid. During the instroke, a clapping effect can be appreciated where

the leading edges of the upper and lower wings are closer to each other while the trailing edges have a certain delay on the motion and are still far apart. When looking at the downstroke, the behaviour seen is the opposite. The delay of the motion of the wing with respect to the wing leads to a peeling effect where the wings is still is contact while the leading edged are already away from each other. This is the clap-and-peel mechanism that have been already mentioned in the first chapter.

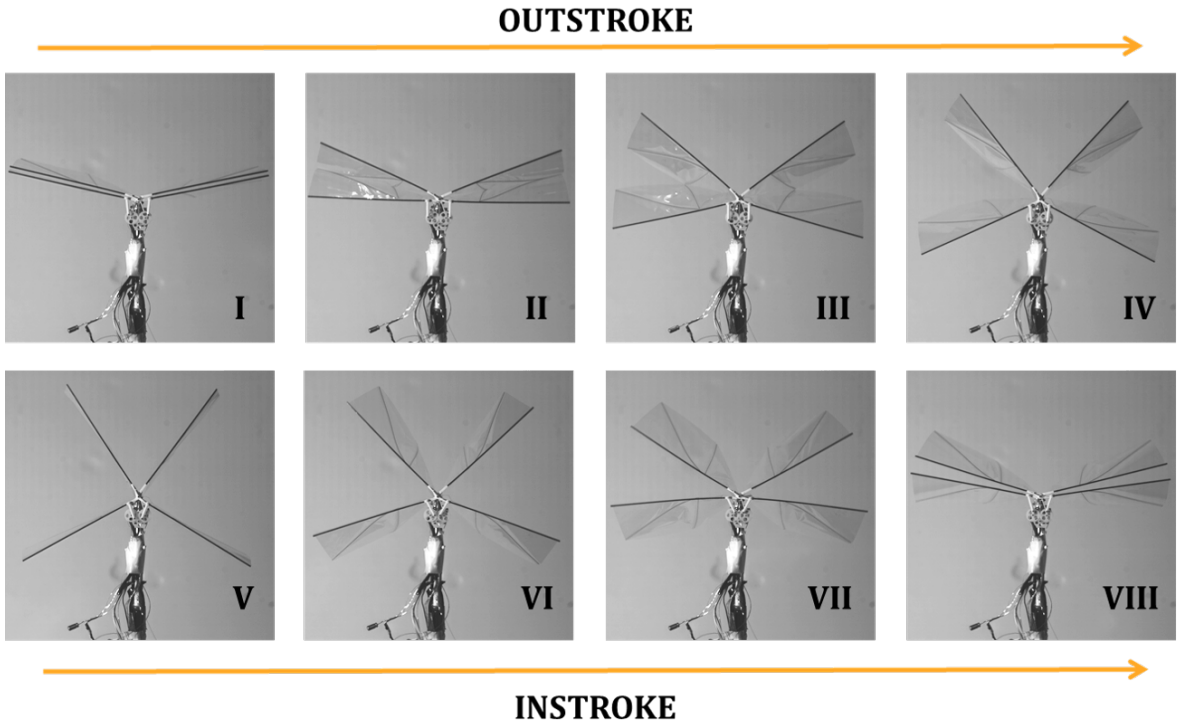

Figure 7.1: Selected phases along the flapping cycle represented by high-speed camera recordings for instroke and outstroke motions.

The flapping cycle has been divided into eight phases to show the behavior of the flow structures and their evolution over the flapping cycle. The flapping cycle is set to start when the wings are closed and the outstroke is going to start. Note, however, that this wing position is virtual with respect to the flow fields, as the flow measured is not corresponding to the position of the physical wings at that precise moment, in view of the convective delay between the wing position and the visualization plane. No direct link between the wing position and the wing deformation can be done with the wake structures show. The wing position has been deduced from the information of the change in crossflow velocity along the wingbeat. When the wings are opening, the flow should go towards the DelFly body and this needs to be visible of the flow field of the wake as well. Then the wings are closing the opposite effect is seen. In this way, a logical correlation between the wake structures and the wing phase that produced them can be found, but only on a qualitative level. As the convection of the wake structures will be different depending on the configuration, the phase number that correspond for example with the beginning of the instroke may vary when comparing one case to another. This will be an indicative of the phase lag in between different configurations.

7.1.3. Bin Size and Statistical Convergence

As explained in chapter 3, Robotic PIV measures the tracks of the particles along the measuring time and the data is stored in a Lagrangian way. To be able to translate the information into an structured grid, the average of the particle velocity going through certain interrogation volumes, called bins, are computed. The bin used in these experiments is a cube with a side length of 3 cm. The size is selected as small as possible but keeping enough particles within the bin so that statistical convergence can be achieved. Statistical convergence does not only depend on the size of the bin, but also on the acquiring time available. If data is being recorded for a longer time, then the information from more particles is

captured and statistical convergence is more easily reached. The more data recorded would therefore allow in principle to have a smaller bin size.

The convergence study performed on the experiments consists on checking the variation of the velocity on different bins as data from more timesteps is included. As the number of timesteps considered increases, the values of the velocity should become constant and at that point, statistical convergence has been reached. Three points are selected for this analysis: one located on the part of the wake that is less influenced by the DelFly so it is the closest to the freestream behaviour (point A), one placed near the tip vortex of the right side of the DelFly (point B) and one at the center of the same vortex (point C). All the points are contained in a spanwise oriented plane at 10 mm distance from the end of the tail (see figure 7.2). This analysis is performed in the wind tunnel fixed reference frame where the X-direction coincides with the freestream direction and the Y-direction aligns with the spanwise direction of the DelFly. The convergence study is performed on the mentioned three points for one phase of the flapping cycle as it is assumed that all of them should have on average the same information. It can be seen in figure 7.3 how the number of particles passing through the bin increases as more timesteps are added for the computations. Point A has considerably less particles than the other two. This can be explained by the fact that the flapping wings change the particle distribution along the wake, generating highly dense regions in between the wings where the other two points are located. Point A is also where statistical convergence is achieved much faster than on the other two because the flow is not perturbed to a great extent.

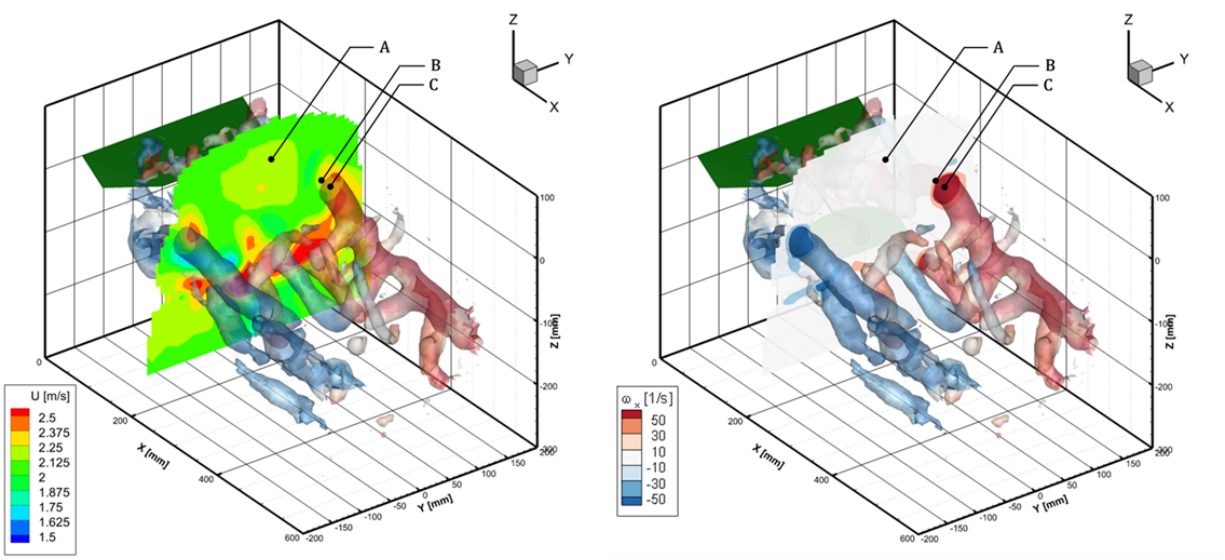

Figure 7.2: 3D view of the vortex structures measured on the wake of the DelFly on Conf 3TC. The points where convergence is studied [A (freestream), 3TC (near vortex) and C (center of vortex)] are contained in a spanwise oriented plane where the freestream is perpendicular. The slice vorticity (right) and the velocity (left) fields are shown.

The other two points are closed to the most important vortex on the wake topology which will be explained in the following section. The vortex is not completely static and the phase averaging performed will also include an inherent uncertainty on the measurements. Therefore the velocity measured will never fully converge, specially on the point located at the center of the vortex. It is considered that statistical convergence is achieved on the experiments performed as valid as possible.

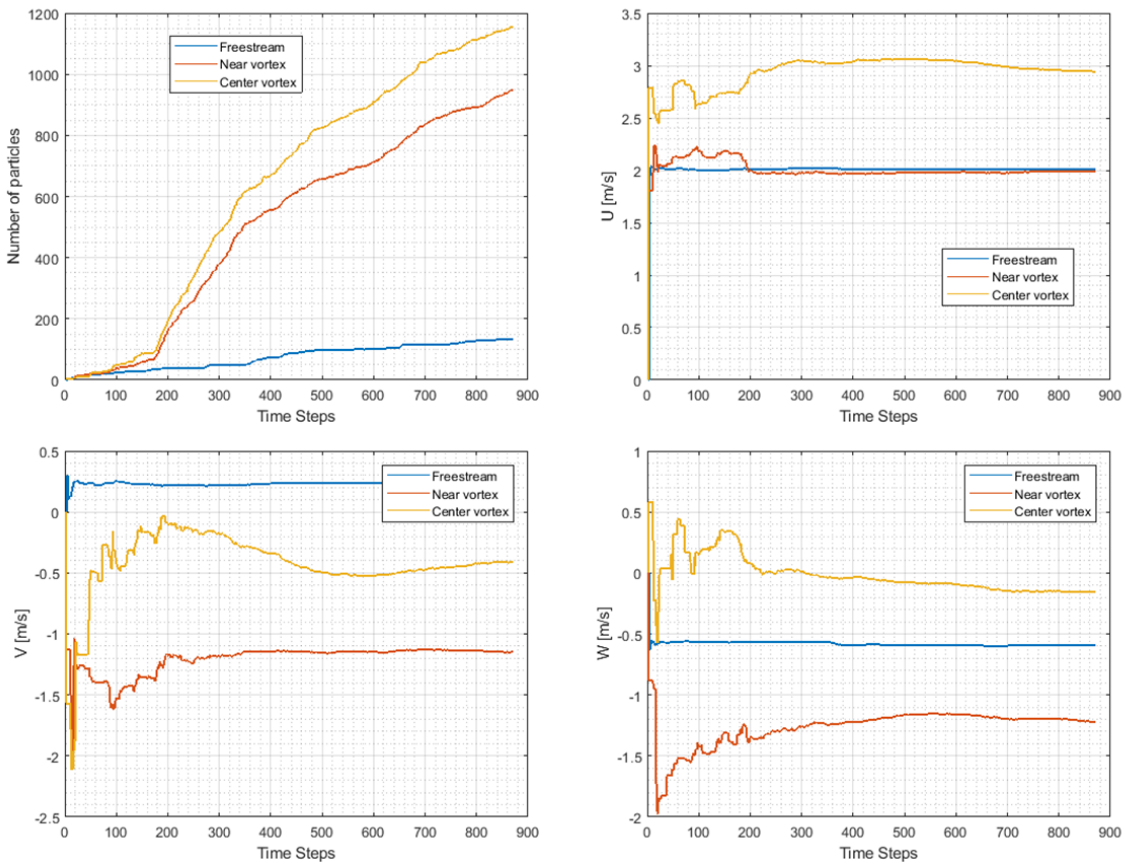

Figure 7.3: Evolution of the number of particles and velocity components for convergence study points along the number of timesteps taken into account.

7.1.4. Measurement volume

The measurement volumes taken at different location of the DelFly wake can be attached together to generate a large volume. The volume that was achieved for the experiments performed in tethered conditions is approximately $50 \times 30 \times 40\ cm^3$. This can be seen in figure 7.4. It is important to keep in mind that the figure shows the DelFly and the measurement volume in body reference frame and this is why the measurement volume is straight with respect to the direction of the DelFly body.

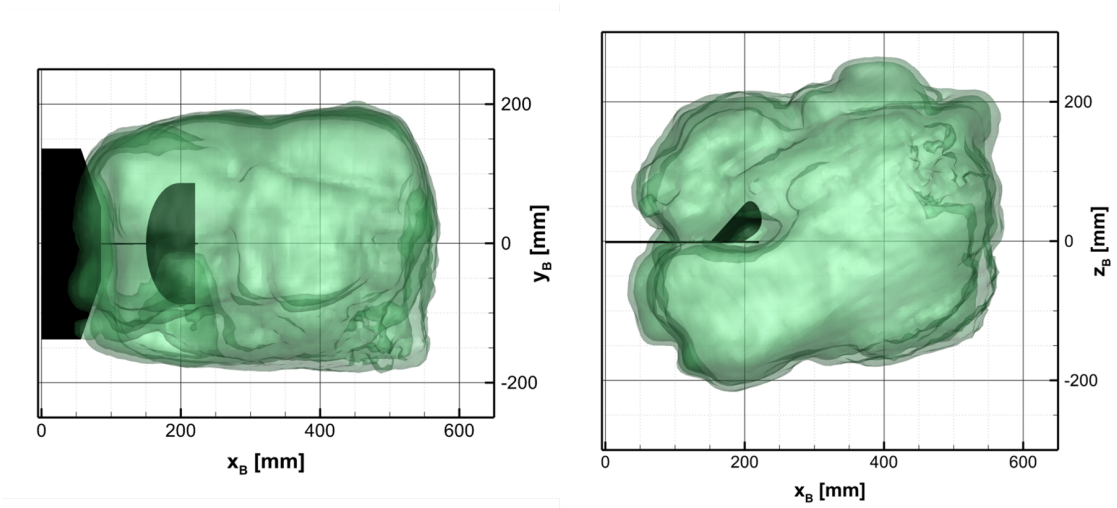

Figure 7.4: Top and side views of the measurement volume acquired with the CVV prove on the tethered experimental campaign.

The measurement volume when doing experiments in free-flight conditions is not as constant. The DelFly moves through space as it is not fixed in a certain position. The measurements performed are always related to the distance of the CVV probe to the DelFly body. This is monitored during the experiments with the camera control system to be able to overlap all the measurements performed and create an average flow field for these experiments as well as the ones done in tethered conditions. When the DelFly deviates further than 10 cm from the desired location, the measurements taken are no longer used when processing the results to avoid to large variations on the vortices captured.

7.2. General Vortex Structures Topology

The current section reports the evolution of the vortex structures through a flapping cycle. First, the velocity results are discussed in wake planes oriented perpendicular to the body axis (section 7.2.1) to explain the main features of the wake topology of the DelFly. Second, the three-dimensional topology of the wake will be presented in section 7.2.2 to analyze the interaction and evolution of the different wake structures.

7.2.1. Wake topology during a flapping cycle

From the data measured for configuration 3TC, information is extracted in a wake plane that is located 10 mm downstream of the trailing edge of the DelFly tail. All information is shown in a body reference frame, with the x-component set along the body of the DelFly and y along the spanwise direction (see figure 4.9). In all the plots, the position of the DelFly is indicated in black to relate the flow field results with the position of the wings. The flapping cycle has been divided into eight phases to show the behavior of the flow structures and their evolution over the flapping cycle. The plots are names corresponding to the approximate phase that generated the behaviour of the flow at that instant. In the setup of these experiments, the CVV system was positioned at the right-hand side of the DelFly (i.e. positive y, see figure 4.4) which leads to a better tracking of the particles on that side of the DelFly, because the particles that are closer to the laser source will scatter more light as the intensity decreases with the fourth power of the distance. At the end, having more particles tracked contributes to a higher accuracy in that measuring side.

Regarding the acceleration region, represented by the red areas of high longitudinal velocity, its evolution along the flapping cycle is presented in figure 7.5. The first phase (figure 7.5-I) of the cycle is presented when the outstroke is just starting (coinciding with the actual movement of the wings at that moment, indicating that a complete cycle is shed in between the wings and the end of the tail where the plotting plane is placed). There is no clear acceleration region in the wake of the DelFly, because the wings are closed. It is seen in figure 7.5-II that a high-velocity region has drastically increased from the previous phase due to the opening of the wings. The deformation of the wings plays a major role in this effect due to the “peeling” action (see figure 7.6).

The acceleration region keeps increasing during phases III and IV as the wings are still opening further. On phase V, when the instroke has started, the acceleration that is generated by the wings reaches its maximum, again due to the deformation of the wings and the “clapping” effect that is created as the wings move together (see figures 7.1 and 7.6). On the following phases, from VI-VIII, the acceleration region reduces its size and it is concentrated into two different regions, one near the body of the DelFly and the other near the tip of the wings. The flow at the first location follows the direction of the body while the second acceleration region has a lateral component of velocity directing the flow outward along the wings (figure 7.7). The outward velocity occurs as a consequence of the deformation of the wings. The deformation along the wing is restricted because of the presence of the stiffeners as shown in figure 2.23; this may be why the acceleration region at the end separates in two. In the most outward part of the wing, apart from the expected chordwise deformation, there is a spanwise deformation of the wing which is a probable cause of the observed acceleration of flow in the lateral direction.

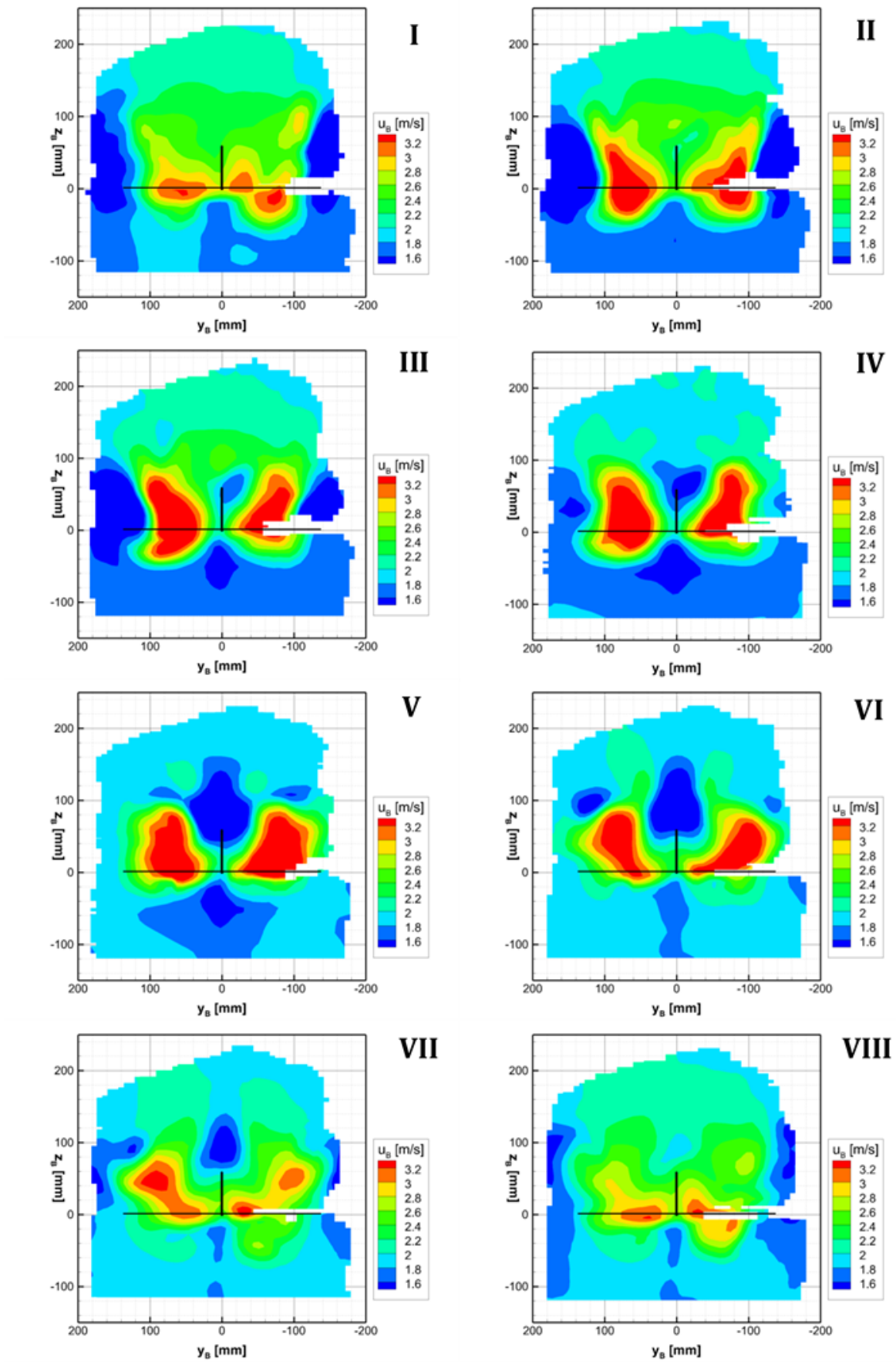

Figure 7.5: Contour plots of the velocity component on the body direction in a spanwise oriented plane at 10 mm distance from the end of the tail at 8 phases along the flapping cycle for configuration 3TC.

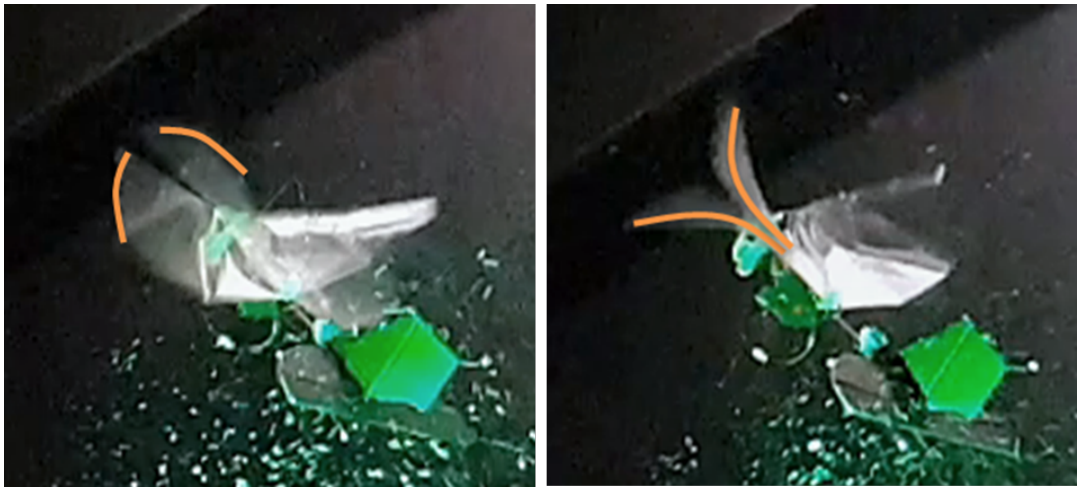

Figure 7.6: Deformation of the wings of the DelFly enhancing the clap (left) and peel (right) mechanisms.

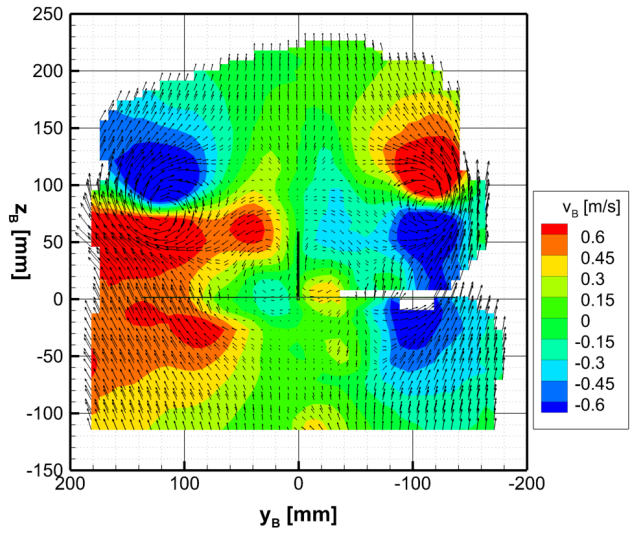

Figure 7.7: Contour plot of the lateral velocity component in a spanwise oriented plane at 10 mm distance from the end of the tail at phase VII of the flapping cycle for configuration 3TC.

Figure 7.8 displays the longitudinal vorticity (i.e. in the direction of the MAV body axis) for subsequent phases of the flapping cycle. The first observation is that there are two main counter-rotating vortices originating from the tips of the DelFly during the entire flapping cycle. According to simple lifting line theory, this implies that positive lift is generated during the entire flapping cycle, which is crucial for the MAV to provide the necessary lift in order to maintain its altitude. Lift is defined as the force generated perpendicular to the free stream, so the vertical force in an absolute reference frame. The vortices are shed by the lower pair of wings during the outstroke and by the upper wings during the instroke. This finding leads to the conclusion that the main vortices are always shed by the wing that is moving in the direction opposite to that of the freestream, when the relative velocity of the wing with respect to the flow is higher and the majority of the force is generated. When looking at the wings moving along with the flow, the velocity experienced by the wing surface is reduced significantly. Assuming that the effective rotational velocity produced by the wing is located at two thirds of the wing span (b=14 cm), it is estimated that the total velocity seen by the wing moving against the flow is more than three times larger than the one seen by the wing going in the freestream direction.

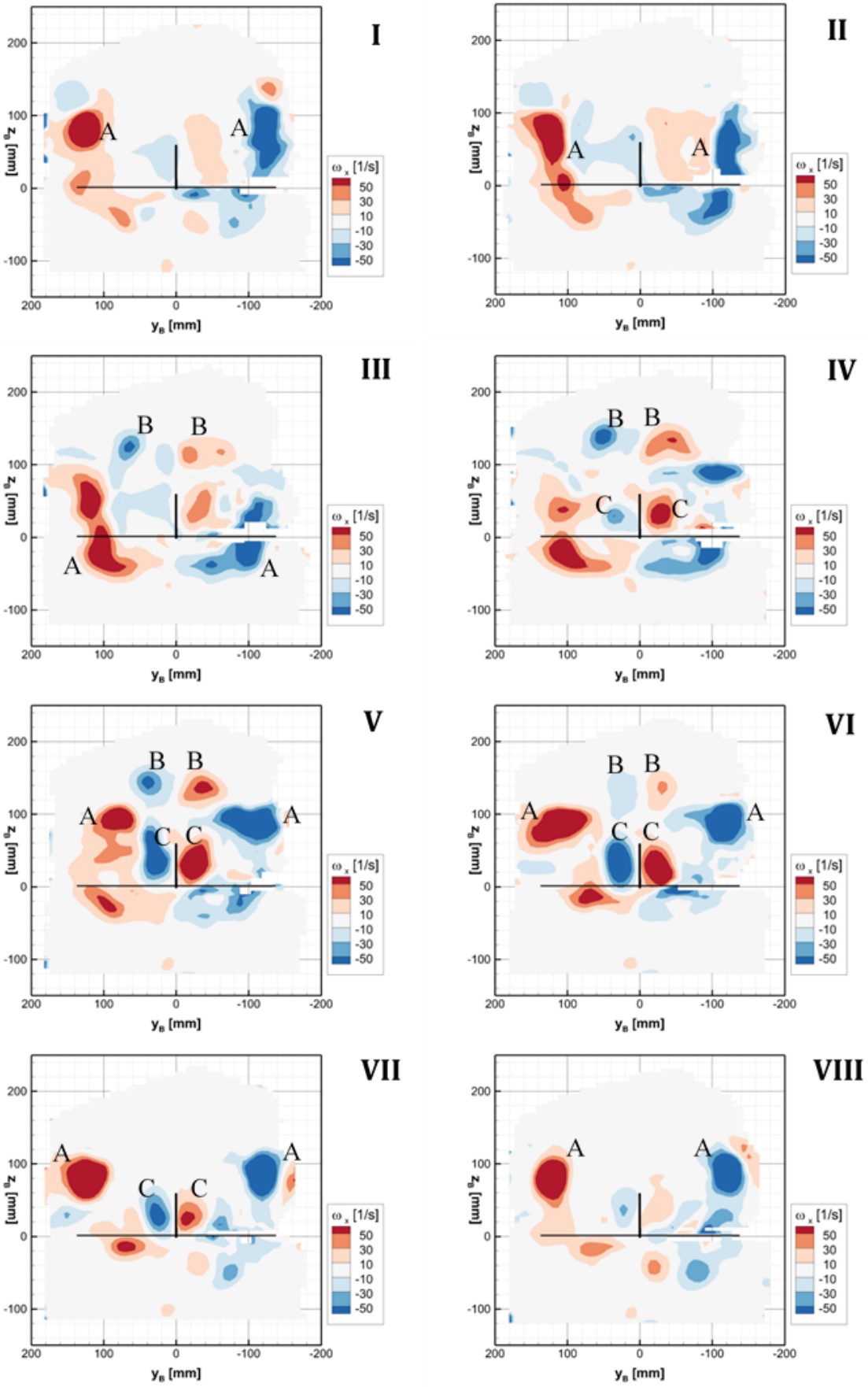

Figure 7.8: Contour plots of the out-of-plane vorticity ω_x in a spanwise oriented plane at 10 mm distance from the end of the tail at 8 phases along the flapping cycle for configuration 3TC.

Looking more in detail to the different phases, two strong counter-rotating tip vortices are retrieved in phase I of the cycle (starting of the outstroke) that are generated by the upper wings during the previous instroke. These tip vortices (wake structures A in figure 7.8) interact with the wings while they are closed and then with the tip vortices generated by the lower wings during the outstroke, resulting in a major tip vortex structure with the same sign for the entire cycle, as it can be clearly appreciated in the 3D view that will be shown in section 7.2.2. The tip vortex structure in phase II is quite elongated, as it is also the case for phase III. The shape of the tip vortices along the outstroke will be further discussed in section 7.2.2. Several smaller vortices start to appear in phase II but they are not yet defined until phase III, named B in the figure. The crossflow going over the wings from tip to root needs to be redirected once it reaches the root, generating these vortices.

In phase IV the wings are completely open and the instroke is starting. According to lifting theory, a lifting surface of finite span will generate tip and root vortices at the extremities of the surface, that are aligned with the freestream direction. This same concept can be applied to flapping wings, similar to propeller theory. In this way when the upper wings start to generate lift, a spanwise-aligned starting vortex is produced that is followed by the generation of counter-rotating tip and root vortices. From figure 7.8-IV and 7.8-V, the evolution of root and tip vortices can be confirmed (wake structures C and A respectively in figure 7.8). To be able to locate the starting vortex, contour plots of y-vorticity are analyzed. In figure 7.9 such plot for phase V is presented, where the starting vortex can be seen at the upper side of the DelFly. The vorticity in that region has a negative sign which means that positive circulation, and therefore positive lift, is being generated on the upper wings. This is the case due to the fact that circulation must be conserved over the domain. The starting vortex can only be clearly seen at the beginning of the instroke because at the beginning of the outstroke a strong interaction between the wings occurs so the change in circulation of the wings is not significant. On the lower side of figure 7.9, however, the opposite behavior is found in a large area with high positive y-vorticity. It corresponds to the ”ending” vortices shed from the lower wings when they stop producing lift. The ”ending” vortex generated by a lifting surface is indeed of opposite sign of that of the starting vortex. The area of positive y-vorticity does not mean that the lower wings have started to generate negative lift. But rather that it was generating lift and then, due to the change in the motion, no more forces were generated, Due to conservation of circulation, another vortex needs to be shed with the extra positive vorticity no longer present on the lower wings.

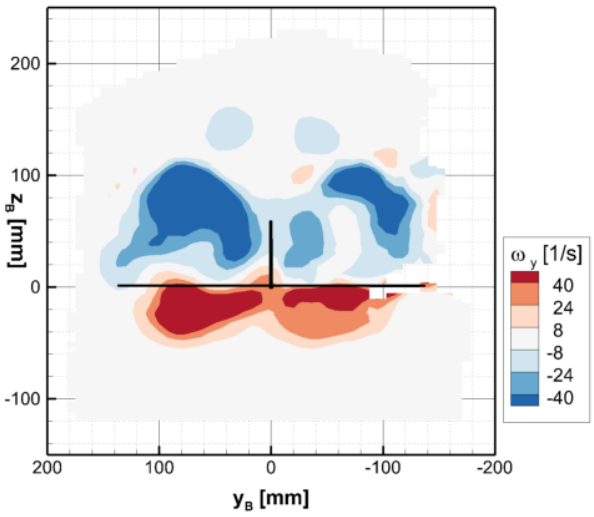

Figure 7.9: Contour plot of the on-plane vorticity ω_y in a spanwise oriented plane at 10 mm distance from the end of the tail at phase V of the flapping cycle for configuration 3TC.

In phase V the wings are completely open, which causes the crossflow along the lower wings to be maximum, hence, the secondary vortices formed on the upper part of the DelFly are enhanced. Then the peak vorticity of these vortices diminishes drastically when the wings come closer together as the flow is now directed away from the root, and towards the tips. In the same way the root vortices also experience a decrease in strength and they nearly disappear at phase VIII as the wings are ap-

proximately closed and the DelFly resembles a fixed wing vehicle. The tip vortices, where the highest rotational velocity can be found, are still maintaining their strength throughout the final phases of the cycle.

7.2.2. 3D wake topology

Considering again configuration 3TC, the vortex structures explained in the previous section are now discussed by means of their 3D representation. Note that although data is available for the full span of the wake, only the structures at one side (corresponding to positive y) are depicted to facilitate the visual interpretation. The development of the topology obtained for different phases of the cycle is sketched to give an overview of the variation of the structures while they are convected. In figure 7.11 the different vortices are identified and the distinction between instroke and outstroke is also presented. The division between instroke and outstroke has been done by visual inspection of the vortical shape in accordance to the reasoning presented in section 7.2.1, so this distinction is primarily meant as a guideline to understand the observed phenomena. It may be reminded here that the x-axis is aligned with the body axis, so the upward deflection of the wake that can be observed in the side view of figure 7.11 is the result of the body angle with respect to the freestream direction ($\alpha_b = 31^o$ in this case).

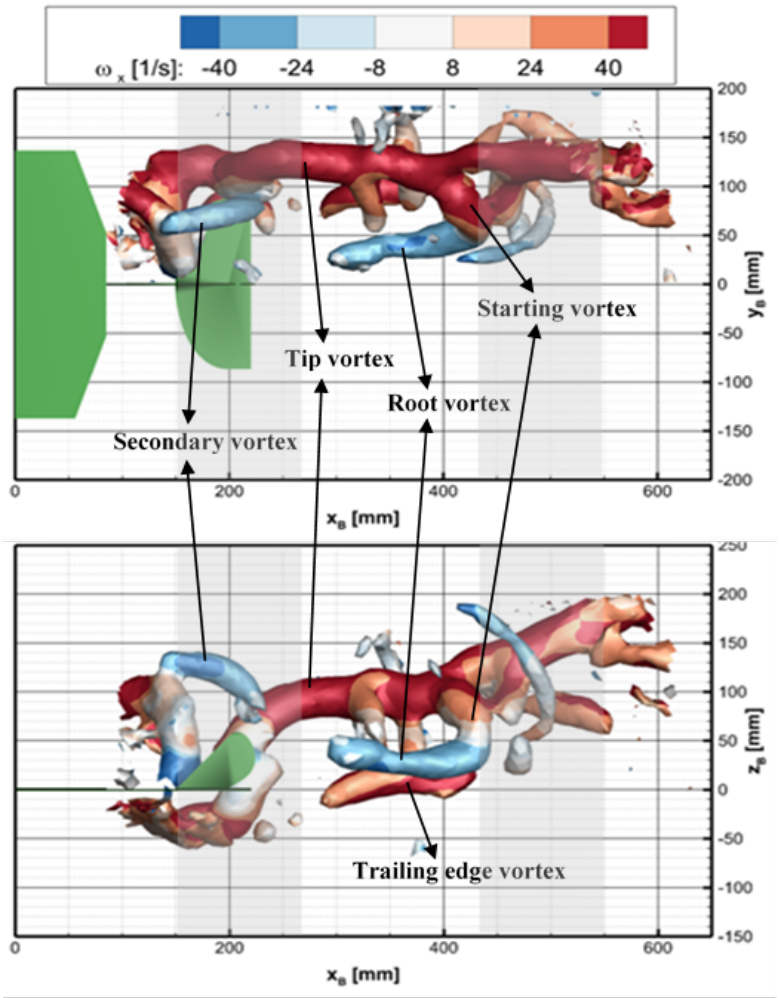

Figure 7.10: Top and side views of the wake structures of configuration 3TC, visualized by isosurfaces of $Q = 600\ s^{-2}$ and colored by ωx for phase II divided in outstroke (gray area) and instroke (white area).

The large tip vortex structures that were already explained in section 7.2.1 can be clearly seen in figure 7.11. The shape of the convected tip vortex seems to be straight with respect to the DelFly body during the instroke while it is deflected downwards during the outstroke, which was also seen in figure 7.8 on phases II and III. During the outstroke, the lower wing is the one that is generating the tip vortex, which agrees with the downward movement of the vortex. Another reason for the shape of the

vortex on the outstroke comes from the fact that the convection velocity is lower in this part of the cycle, especially in the tip area where air is being redirected towards the root. Therefore, the vortex does not travel away along the x-direction in the first stages of the outstroke. Indeed, the vortex is moved slightly towards the center of the DelFly due to the crossflow that appears. This also explains the fact that the instroke structures are longer in space than the ones generated during the outstroke (the gray area is shorter than the white area).

The wake topology is highly affected by the different convection velocities that are experienced throughout the flapping cycle in different locations around the wings (figure 7.5). This makes the analysis of the wake evolution more complex. The vortices generated by the flapping wings are not convected in the direction of the body of the DelFly, neither in the direction of the freestream. There is a combination between the freestream and the effect of the induced high-speed flow generated through the cycle. The result is a certain angle of the wake that varies as the structures travel away from the wings which means that the importance of the acceleration jet decreases and the wake convection velocity will become more uniform and closer to the freestream velocity. However, this point is not reached within the measuring volume studied and, instead, it will be assumed that over the measured region the angle of the wake is approximately constant. The value of this wake angle is computed by taking the information of the wake at two different spanwise oriented planes that are spaced in the x-direction, such that they correspond to the same phase of the flapping cycle. A correlation between the x-vorticity values of both planes gives the displacement of the vortex structures during the length of a flapping cycle. This procedure is carried out for each of the eight phases shown in section 7.2.1. The result for each phase varies, so only the correlations with a signal to noise ratio SNR>2.9 are considered. The mean angle of the wake with respect to the longitudinal body direction is established to be approximately 15 degrees, which agrees with a visual inspection looking at the side view in figure 7.11. The angle of the wake in the lateral direction is not so easily visualized. The cross correlation procedure computes an outwards movement of the wake structures with an angle of 2 degrees. The outward velocity that was presented in the previous section has an influence on the movement of the wake which slightly moves away from the center of the DelFly.

The evolution of the wake at three different phases during the flapping cycle can be seen in figure 13, where the plane location corresponding to the information depicted in section 7.2.1 is also indicated (orange line). The assumption of a constant wake angle seems to be reasonable when looking at the side views of the different phases. Starting from phase II that has been explained in detail before, phase V shows clearly the starting vortex linked to the root and tip vortices during the instroke. The secondary vortex created during the outstroke moves upwards and inwards, respectively in the side and top views. As it can only be expected, the vortex structures become more diffused as they are convected which can be clearly seen when looking at the root vortex from phase II which is not seen so clearly in phase V. The peak vorticity of all vortex structures also decreases.

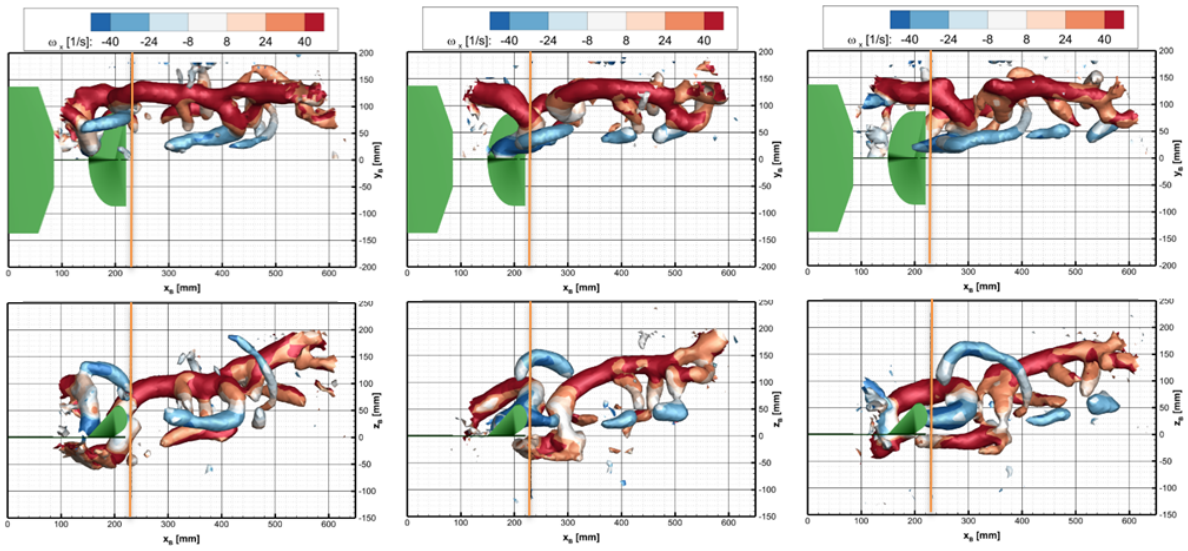

Figure 7.11: Top and side views of the wake structures visualized by isosurfaces of $Q = 600\ s^{-2}$ and colored by ω_x for phases II (left), phase V (center) and phase VII (right) of configuration 3TC.

On phase VII the vortex structures from the instroke have moved downstream and the trailing edge vortex from the lower wings is seen below the root vortex. The secondary vortex seems to interact with small vortices generated before. This interaction probably originates before this point but the reason behind this interaction has not been studied in detail.

7.3. Effect of reduced frequency

From previous studies [60], it has been concluded that the interaction between the vortices in the wake of a flapping wing motion is influenced by the reduced frequency of the system. To investigate this effect, configurations 1, 2 and 3 on tethered conditions will be compared, where the reduced frequency of configuration 3 is five times higher than the one of configuration 1 (table 7.1). The difference between the configurations are assessed both qualitatively and quantitatively.

The 3D wake topology for each configuration is presented in figure 7.12. There are large differences between the different topologies shown, but some similarities can still be observed. The major vortex structure appreciated in the configurations is the tip vortex. The tip vortex in configuration 1 is no longer a smooth structure throughout the flapping cycle, but it has a distinct shape for instroke and outstroke. During the instroke, the tip vortex and the starting vortex cannot be distinguished, forming a single oblique vortex that starts close to the root of the DelFly and moves outwards as the instroke develops. The tip vortex generated during the outstroke is shorter than for the instroke, as it was the case for configuration 3, and it follows a straighter path with respect to the body of the MAV. A second tip vortex structure generated during the instroke on the lower part of the DelFly can be seen for configuration 1. This indicates that the lower wing is producing a vertical force. However, the x-vorticity of this structure is negative, which indicates that negative lift is being generated. This can be confirmed from analyzing the y-vorticity which has positive values for the lower wing during the instroke (see figure 7.13). But in this case it is not the trailing vortex that is shed but the starting vortex of a sudden change in lift generation. The appearance of such a vortex is related to the velocity components seen by each of the wings during the cycle. Both wings will experience a velocity on the body direction due to a component of the freestream ($Vx_\infty = U_\infty cos(\alpha_b)$). On the rotational plane (Z-direction), the wings are in motion so a certain rotational velocity will be experienced on opposite direction for the pair of wings. For the purposes of this study, it is assumed a rotational velocity at two thirds of the length of the span ($b = 14cm$) and at maximum angular velocity which is equal to the flapping frequency ($Vz_{rot} = \frac{2}{3} f_{flap} b$). In addition to the rotational velocity, a second component of the freestream is also present in the rotational plane ($Vz_\infty = U_\infty sin(\alpha_b)$). In table 7.2, the resultant velocities on the Z-direction for the wing going in the same direction as the freestream and the one opposing the flow are computed. It is seen that the difference in magnitude between the wings is extremely high for configuration 3 where the wing moving with the freestream sees barely no Vz. This starts to change as configuration 1 is approached. In configuration 1, both wings see a considerable velocity of the Z direction which directly relates to the angle of attack seen by the wing which can have as an effect that both wings generate a certain lift force. The strength of the vortex on the wing going along with the freestream (lower wing) is smaller than the one measured for the tip vortex of the wing opposing the freestream (upper wing), so the resulting force generated by the DelFly is still positive. Another vortex structure that appears for configuration 1 is located on the upper part of the instroke tip vortex. This vortex is not present close to the wings, but as the wake travels downstream the vortices interact strongly with each other. The outstroke tip vortex seems to interact with the tip vortex of the following instroke. When looking at configuration 2, the wake topology is more similar to the one of configuration 3. There is a clear tip vortex and a starting vortex can be also seen. The shape however is more circular rather that straight as in the case of configuration 3, which means that configuration 2 starts to be more similar to configuration 1.

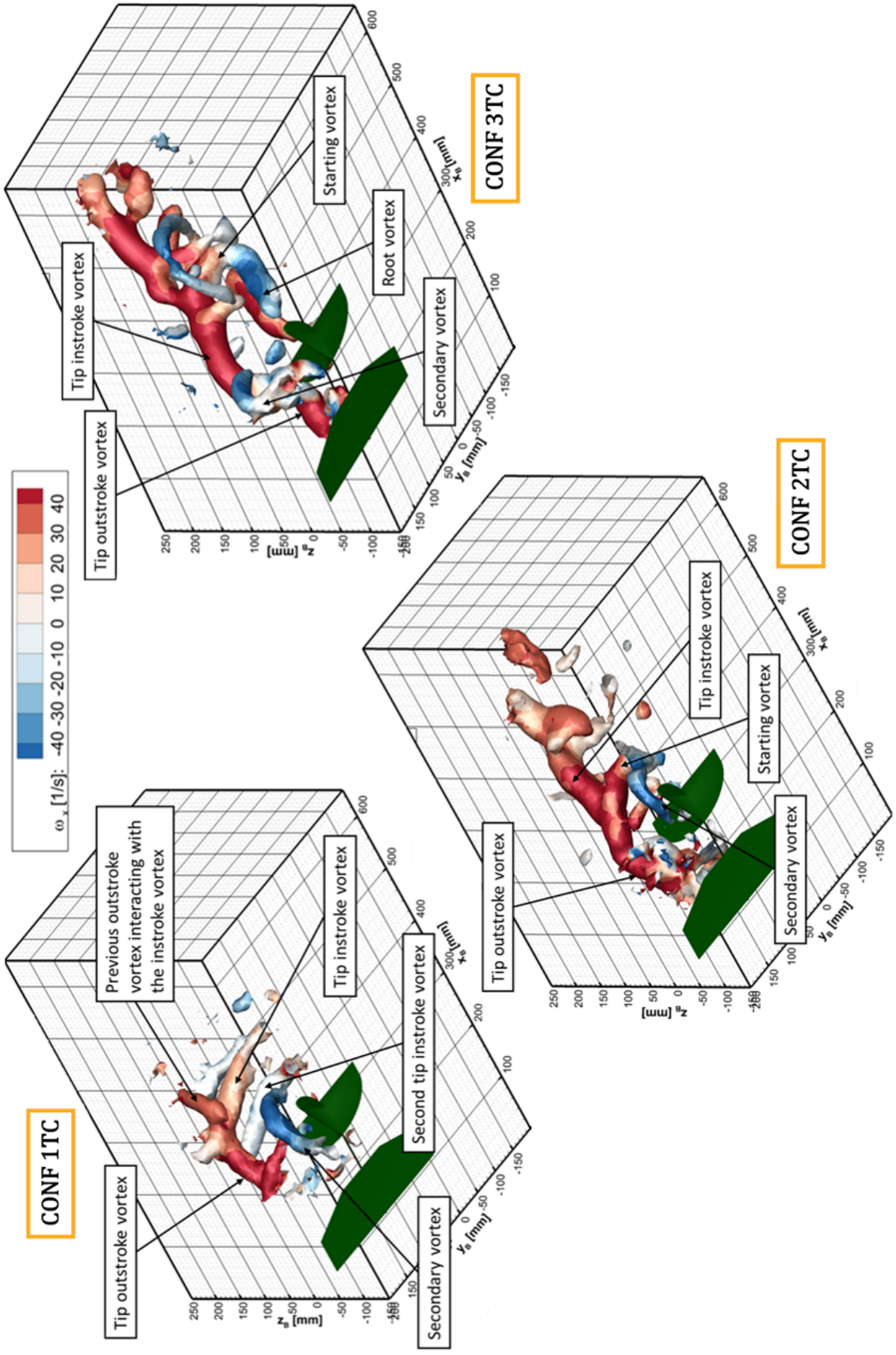

Figure 7.12: 3D view of the wake structures visualized by isosurfaces of $Q = 500\ s^{-2}$ and colored by ω_x for phases III of configuration 1TC (left), 2TC (center) and 3TC (right).

Table 7.2: Flight parameters for each configuration and the resultant wake parameters obtained.

Conf.	U_∞ $[m/s]$	f_{flap} $[Hz]$	α_b [°]	Vz_{rot} $[m/s]$	Vx_∞ $[m/s]$	Vz_∞ $[m/s]$	$\lvert Vz_{rot} + Vz_\infty \rvert$ $[m/s]$	$\lvert Vz_{rot} - Vz_\infty \rvert$ $[m/s]$
1 TC	0.5	13.0	70	1.213	0.171	0.470	1.683	0.743
2 TC	1.0	12.0	45	1.120	0.707	0.707	1.827	0.413
3 TC	2.0	10.2	31	0.952	1.714	1.030	1.982	0.078

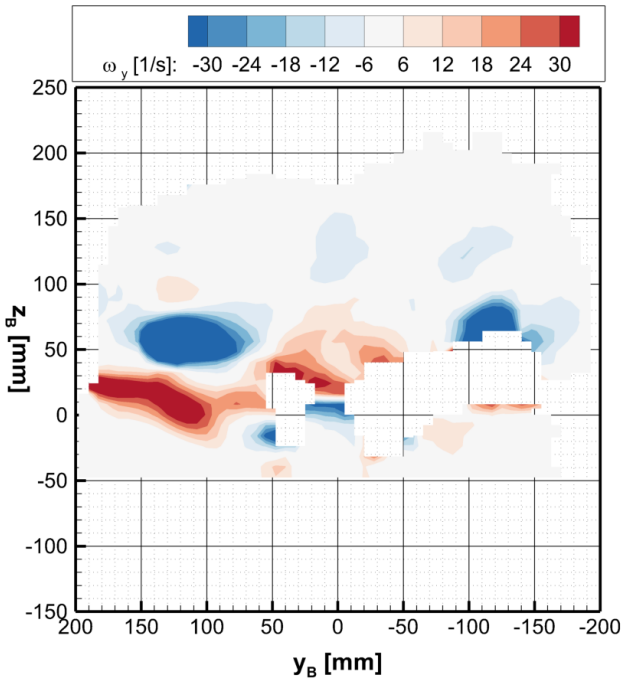

Figure 7.13: Contour plot of the on-plane vorticity ω_y in a spanwise oriented plane at 10 mm distance from the end of the tail at phase V of the flapping cycle for configuration 1TC.

No root vortex is observed neither in configuration 1 or configuration 2 for any of the wings at any phase of the flapping cycle. Due to the relatively high flapping frequency, the flow at the root of the wings is constantly changing and the dominant component is the crossflow. The root vortex is not present as it is no generated as fast as the change in wing conditions happens. As the crossflow is augmented, the secondary vortex should have a higher peak vorticity. The secondary vortex also changes length from one configuration to the other, apart from the higher peak vorticity. It is hypothesized that the reason for this finding is related to the deformation of the wings. As the flapping frequency increases, the deformation of the wings is enhanced and the phase-lag in between the leading edge and the trailing edge of the wings increases. This allows for the secondary vortex to last for a longer time as the wings do not close completely until later. The secondary vortex seems to be generated closer to the root on configurations 1 and 2 than in configuration 3 in both y- and z-direction. The fact that it is closer in the z-direction is likely due to the reduction of the free stream component so the convection of the vortices is much more influenced by the flow acceleration induced by the wings. This causes the angle of the wake with respect to the body to be smaller. However, it is difficult to give a conclusive statement on that aspect, as the wake length that could be reliably resolved reduces moving from configuration 3 to 1, for a number of reasons. Firstly, the vortex structures are weaker for the first configurations, so they fade away much faster and become more difficult to detect. An additional matter is the larger angle of the body with respect to the freestream direction, so the wake more quickly interacts with the shear layer of the open test section of the wind tunnel. Also, the high body angle brings the wings closer to the supporting structure, which may affect the flow and the measurement of possible vortices generated

by the flapping wings on the lower side of the DelFly.

To provide a more quantitative view of the differences between the two configurations, several parameters have been measured: the wake length of a flapping cycle, the maximum longitudinal velocity and the peak vorticity in x-direction. Unfortunately, the resulting values of the wake angle for configurations 1TC and 2TC were not conclusive mainly since the wake structures change rapidly which does not allow to use the technique that is used in configuration 3TC.The information has been collected in table 7.3. The wake length of a flapping cycle has been computed by determining the difference between the location of the start of the instroke which is defined as the time when the starting vortex is shed. This length is retrieved by visual means from the flow visualization results to give an approximate length, not as an exact measurement. The values of maximum velocity and vorticity are computed by selecting only a region where more that 1200 particles have been tracked on the same slice as the contour plots shown in section 7.2.1.

Table 7.3: Flight parameters for each configuration and the resultant wake parameters obtained.

Conf.	U_∞ $[m/s]$	f_{flap} $[Hz]$	α_b [°]	**Length of cycle** $[cm]$		$U_{b_{MAX}}$ $[m/s]$	$\left(\frac{U_{b_{MAX}}}{U_\infty cos(\alpha_b)}\right)$	$\omega_{X_{MAX}}$ $[1/s]$
				Measured	Taylor's hyp.	at $x_b = 23\ cm$		
1 TC	0.5	13.0	70	16	1.3	1.5	(8.6)	110
2 TC	1.0	12.0	45	18	5.9	2.7	(3.8)	140
3 TC	2.0	10.2	31	27	16.8	3.8	(2.2)	200

The value of the length of the flapping cycle following from Taylor's hypothesis has also been calculated for comparison. According to this approach the wake structures are convected at the free stream velocity. Since the DelFly is positioned at a certain angle of attack, only the free stream component directed along the x-body axis is considered in order to retrieve the wake length in x-direction. This gives a corresponding expression for the wake length as: $U_\infty cos(\alpha_b)/f_{flap}$. As seen in table 7.3, the length computed with this hypothesis is (much) shorter than the actual wake length measured, which implies that the effective convection speed is higher than that predicted by Taylor's hypothesis. For configuration 3TC, the difference between the two is approximately 38% of the measured wake length. This difference is caused by the increased convection speed resulting from the high-speed jet generated by the flapping wings, as previously discussed. The maximum velocity of the jet, $U_{b_{MAX}}$, is more than twice the free stream velocity. The difference between the wake lengths for configuration 1TC is much more dramatic, reaching a 92% difference. As it could be predicted, configuration 2TC has a difference of wake length of 67% which lies in between the other two. This proves the invalidity of Taylor's hypothesis for reduced frequency situations where the high-speed jet provides a strong flow acceleration, which occurs at higher flapping frequencies in combination with low forward velocities. From the observed wake length and the flapping frequency, an effective (average) convection velocity can be derived, which yields 2.08 m/s, 2.16 m/s and 2.75 m/s for configurations 1TC, 2TC and 3TC, respectively, indeed well in excess of the corresponding freestream velocity.

The maximum values of x-vorticity (ω_X) are found always in the tip vortex structure across all phases analyzed. The maximum value for configuration 3TC is much larger than the one of configuration 1TC as a greater velocity gradient is generated on the wings for the first one. The overall maximum value along the flapping cycle is found at the beginning of the outstroke, which corresponds to phase II for configuration 3TC, while for configuration 1TC it occurs at phase III. This indicates a probable phase lag of the wake structures generated by the flapping wigs. This phenomenon was already discussed by Percin et al. [61]. The maximum is reached when the wings are close together and coming apart from each other, which can relate to the interaction of the tip vortex from the previous instroke that combines its strength with the following vortex generated by the lower wing.

7.4. Effect of the tail

To be able to compare the flow characteristics with and without tail, experiments are performed with the same flow conditions in terms of freestream, the flapping frequency and the angle of attack of the body. The differences and similarities will be explained in the following sections. One thing to notice before going into detail on the different results is that there was a shift on the phases measured along the flapping cycle. For configuration 3TC with tail, it has been shown how, for example, phase V marks the start of the instroke. For configuration 3TC without the tail that was not the case. In fact the phases where shifted by half the cycle. This means that to compare both measurements, the comparisons have to be made by selecting for example the phase V with tail and phase I without tail.

7.4.1. Variation of velocity fields

Looking at the axial acceleration region, it is seem that the measurements without the tail have a smaller acceleration region compared to the measurements with tail. Figure 7.14 illustrates this behaviour. The acceleration region with tail (shown in the left side of the plot) seems greater than one without the tail (located on the right side). The shape of the high velocity region is similar between the different cases as the motion of the wing has not change drastically. When performing an average over the boxes seen in figure 7.14, the mean axial velocity found for the tail on case is 2.73 m/s while for the tail off case is 2.61 m/s. Even if the difference in the high velocity region between the two cases is only of approximately 4.5%.

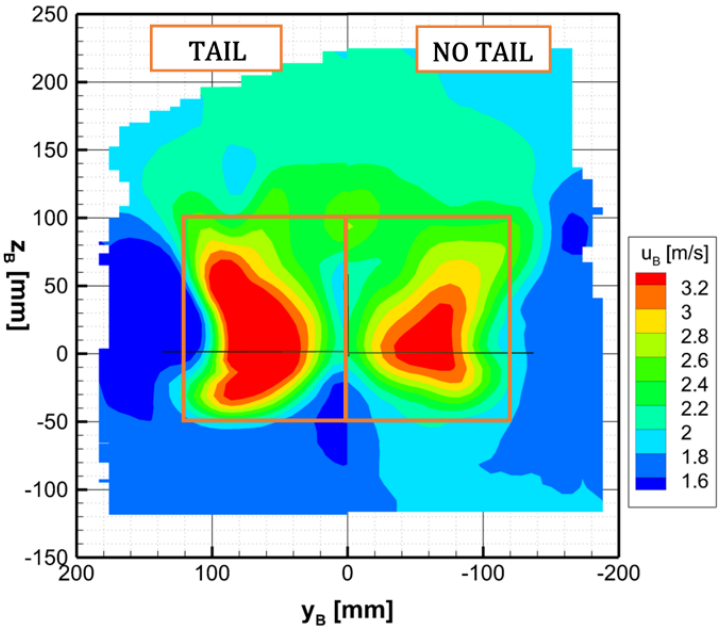

Figure 7.14: Contour plot (left side represents phase III with tail and right side represents phase VII without tail) of the axial velocity component in a spanwise oriented plane at 10 mm distance from the end of the tail of the flapping cycle for conf. 3TC

It seems that the motion was not quite symmetric for the no tail measurement as shown in figure 7.15. It is probable that any asymmetry on the force created by the wings causes a small lateral motion, which in the case of tail on is not visible as the tail keeps the DelFly stable. As stability is lower when no tail is present, a small motion on the DelFly at the end provokes an asymmetry on the flow measured.

When looking at the lateral velocity, the cross flow seen after the DelFly is also greater in the presence of a tail than without it. This seems reasonable knowing that the axial velocity follows the same trend. The flow is not only accelerated in the axial direction but it also has a lateral component. The tail works as a separating wall between the flow on one side of the DelFly and the other. The allows a velocity gradient larger that when there is no tail and the flow mixes after it passes through the wings. The higher axial velocity when the tail is present may due to this reason as well. The higher diffusion of the flow when no tail is present can account for the reduction of the acceleration region.

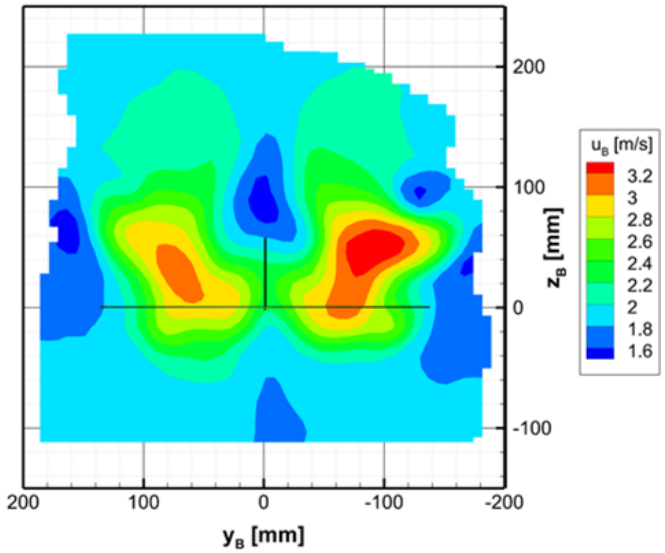

Figure 7.15: Contour plot of the axial velocity component of phase VII without tail in a spanwise oriented plane at 10 mm distance from the end of the tail of the flapping cycle for conf. 3TC

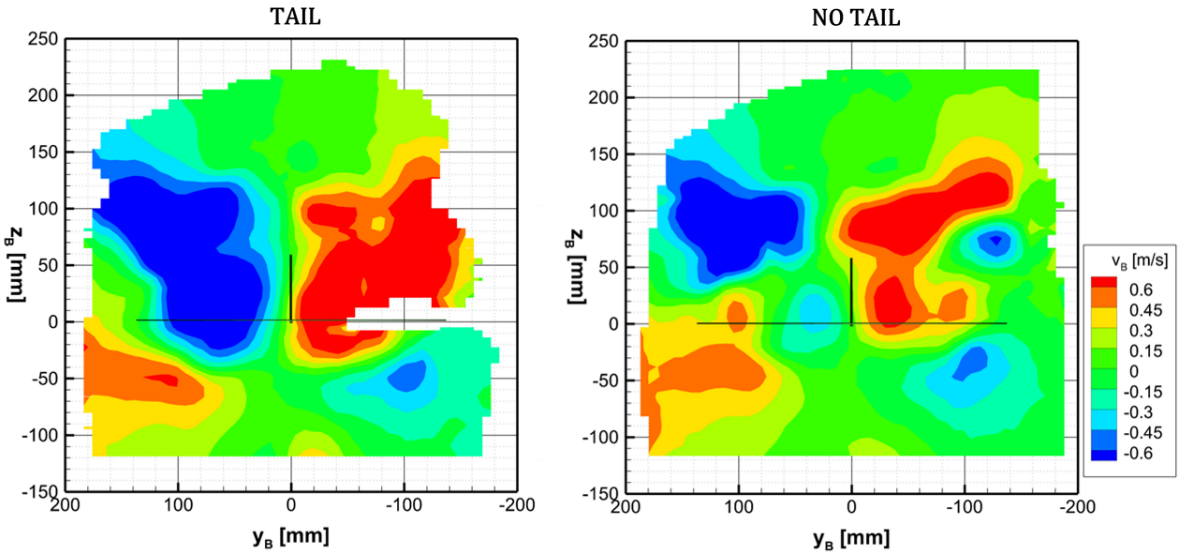

Figure 7.16: Contour plot (left side represents phase III with tail and right side represents phase VII without tail) of the lateral velocity component in a spanwise oriented plane at 10 mm distance from the end of the tail of the flapping cycle for conf. 3TC

7.4.2. Variation of shed vortices

Focusing on the vorticity field generated by the wings, the results found with and without tail are quite similar as shown in figure 7.17. There is no clear variation on the shape and peak vorticity of the tip vortices of the wings along the flapping cycle. As the tip vortex is the predominant structure on the topology, it is probable that it is not sensitive to small variations on the flow that would occur at the center of the DelFly due to the lack of a tail. However the root vortex, which is located the closest to the center of the MAV, is the one that is most significantly affected. The root vortices on each side of the DelFly is smaller when there is not tail. It follows the same reasoning as discussed when looking into the velocity fields. The two counter-rotating root vortices shed during the instroke are separated right after the wings by the tail so that each can follow its course without being influenced by the other and viceversa. When the interaction takes place however, right after the vortices are generated, the vortices start to cancel out each other and they fade more quickly. The secondary vortices seem to also become less distinct but the level of change is too small to be able to conclude the hypothesis.

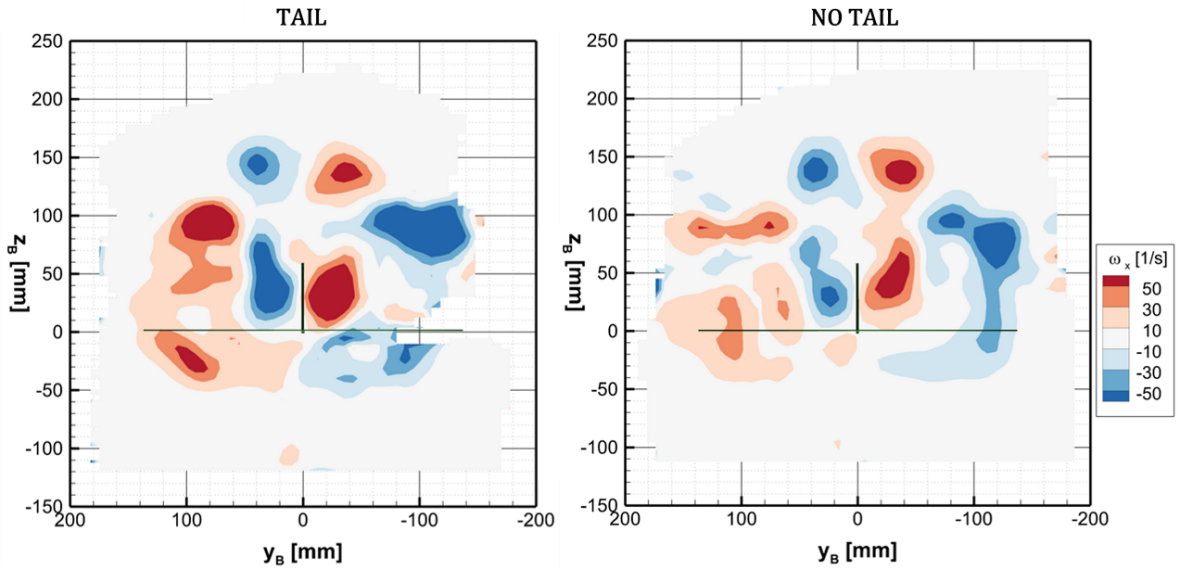

Figure 7.17: Contour plot (left side represents phase III with tail and right side represents phase VII without tail) of the vorticity component ω_x in a spanwise oriented plane at 10 mm distance from the end of the tail of the flapping cycle for conf. 3TC

Finally, the complete wake topologies can be compared with and without tail looking at figure 7.18. It can be clearly seem how the length of the cycle becomes smaller when no tail is used. This is directly related to the acceleration region present on the flow, which is smaller without the tail. The starting vortex that creates a link between the root and tip vortices is not well captured in the measurements performed without tail. Due to flow mixing, the starting vortex may have diffused much faster that in the other case.

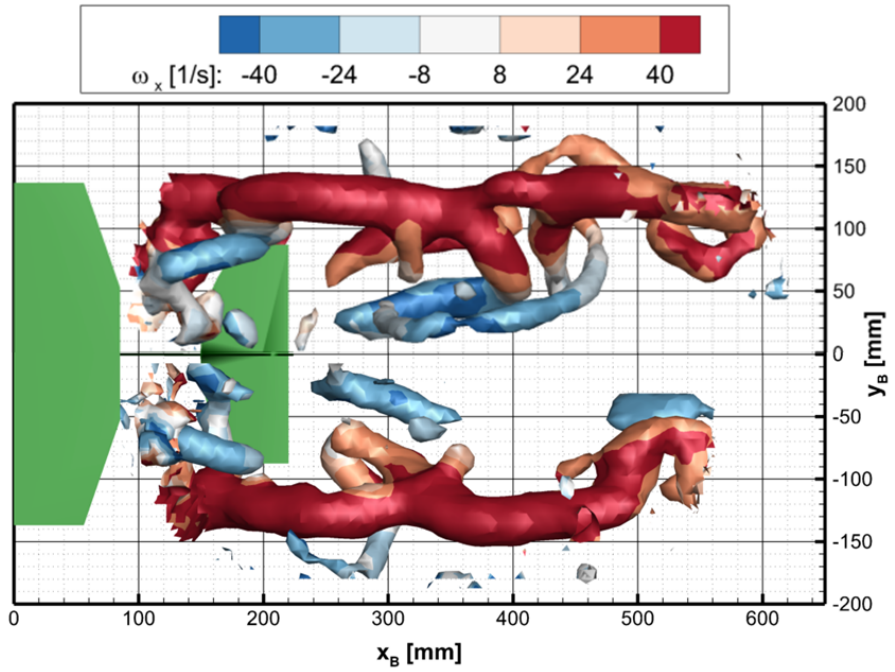

Figure 7.18: Top view of the wake structures visualized by isosurfaces of $Q = 500\ s^{-2}$ (top side represents phase V with tail and bottom side represents phase I without tail) colored by ω_x for configuration 3TC

7.5. Free-Flight vs. Tethered conditions

To finalize the analysis, a comparison between tethered and free flight experimental conditions is investigated using configurations 3TC and 3FC . The reduced frequency for both cases is very similar, albeit that the flapping frequency for case 3FC is slightly higher than for case 3TC , approximately 10% difference is found. This appears to influence the length of the wake for a flapping cycle, as it could be expected. The length of the wake is approximately 27 cm and 24 cm for configurations 3TC and 3FC respectively, as seen in figure 7.19, which is consistent with the difference in flapping frequency. The vortex structures that can be appreciated for free-flight are not captured with the same level of detail and only the main structure, the tip vortex, can be clearly seen. The root vortex is one of the structures that are not visible for configuration 3FC while there are well defined for configuration 3TC.

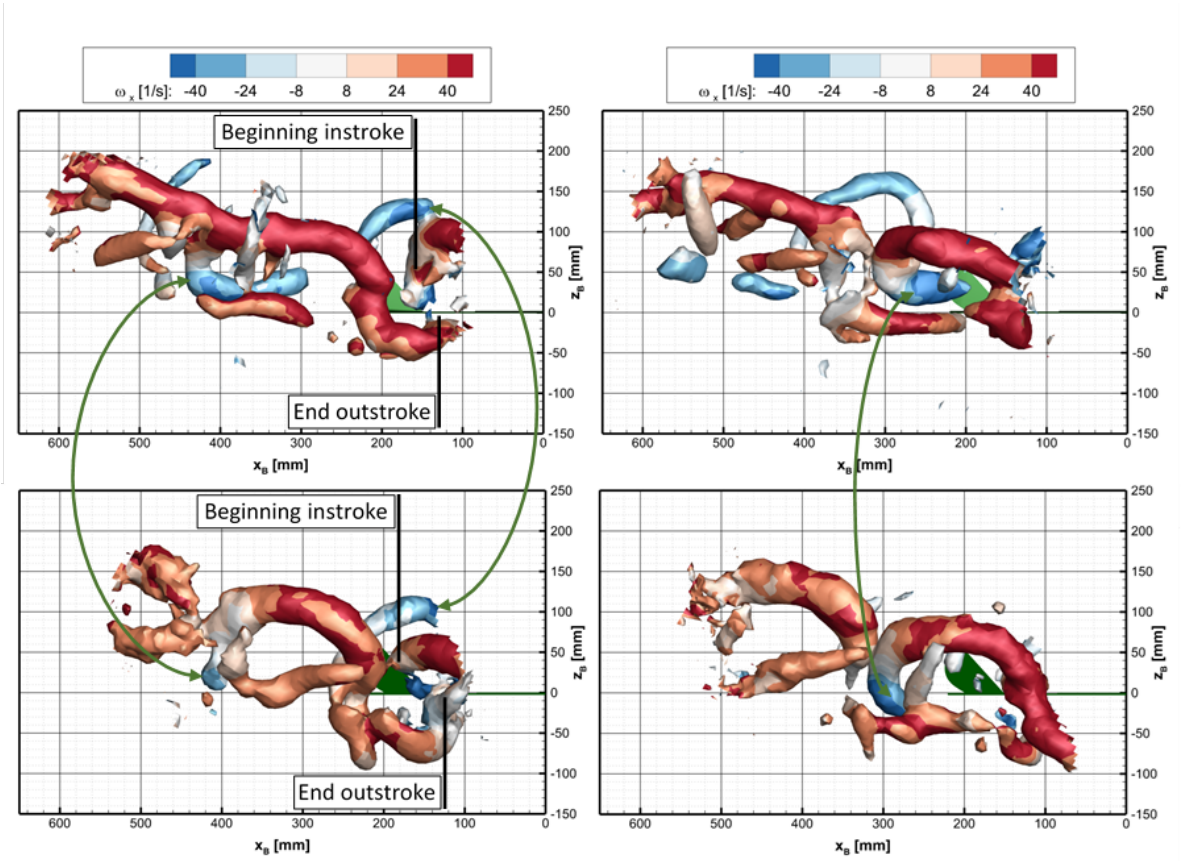

Figure 7.19: Side views of the wake structures visualized by isosurfaces of $Q = 600\ s^{-2}$ and colored by ω_X for phases II of configurations 3TC (right) and 3FC (left).

The dynamic motion of the DelFly during free-flight tests is inevitable, due to the fact that the DelFly is flying around a set point with small deviations from it. The largest deviations are found in the lateral direction which can reach a variation of 20 cm. Using the information from the flight tracking system, the position deviations are corrected for, in order to be able to process the data with the phase-lock averaging procedure. However, the motion of the DelFly, especially the lateral component which also involves the heading of the Delfly with respect to the free stream, changes the position and the orientation of the wake and to some extent the way the vortex structures are shed. This translates in the end in fluctuations of the position of the individual wake structures that causes the smaller structures to be spread out over the volume, so they are no longer detectable. The big structures are still visible but the core, as seen in figure 7.19, is larger due to this “blurring” of the vortex and the x-vorticity reached is smaller than for tethered conditions. The overall shape of the tip vortex however is still very similar to the vortex structure found in tethered conditions, indicating that the structures generated on both cases follow the same trend.

The variations in the DelFly position are the reason why for the first configuration tested in free-flight conditions (2FC) the final measurements were not showing a representative view of the wake topology of the DelFly. The vortex structures were distorted, and no clear view could be given. Apart from the motion of the DelFly, other issues that contributed to the low visibility of vortex structures are the disturbances of the flow due to the wind tunnel working at such low speeds, the blockage of the seeder and extra blockage due to foam generated as a consequence of the set of parameters used in the seeder generator. However, for configuration 3FC, interesting conclusions can be extracted in a qualitative analysis. Apart from the main tip vortex, another vortex structure with the same X vorticity (ω_x) sign as the tip vortex can be seen in figure 7.19. The vortex has a considerable peak vorticity along the instroke and then when the tip vortex is deflected downwards during the outstroke then the second vortex ceases. That second vortex is in fact the tip vortex generated on the outstroke of the previous cycle that interacts with the following tip vortex generated on the subsequent instroke. The interaction that takes place in free-flight conditions seems to be more active than in tethered conditions where the previous downstroke tip vortex does not continue until the downstroke of the succeeding cycle. The previous downstroke tip vortex also moves towards the tip vortex generated on the instroke, forming a triangular shape. The deflection of the tip vortex during the downstroke also seems to be more pronounced in free-flight conditions looking at the difference in Z coordinates in between the tip vortex during the instroke and during the end of the outstroke. In addition, it is noticed that the interaction in between one flapping cycle and the next is more significant in free-flight conditions, which may be the cause for a stronger interaction in between the tip vortices as explained before. In tethered conditions, the instroke of the following cycle starts approximately at the same time that the downstroke of the previous cycle finishes as seen in figure 7.19. In free-flight condition, the instroke starts approximately earlier at around half way thought the downstroke of the previous cycle. Last but not least, it is important to point out that even if the other vortex structures clearly seen in tether conditions are not well seen in free-flight, the beginning of such structures are still captured during the measurements.

8

Conclusions and Recommendations

On the first section of this chapter, the major findings established by the present project are briefly compiled. On the following section, some recommendations are proposed, which aim to perform new studies on the DelFly with the novel Robotic Volumetric Velocimetry technique.

8.1. Conclusions

The beginning of this project started from the hypothesis that the use of an innovative PIV technique could provide relevant information about the behaviour of the flow around a flapping wing mechanism. The main advantage of the new measurement technique, called Robotic Volumetric Velocimetry, are the capability to measure the three components of velocity within a large volume. The unique compactness of the system allows as well to measure several volumes close together which at the end can be combined into a considerable final measurement space. In order to assess the outcome of the study, the following main research objective has been formulated:

"*Investigate the flow behaviour in regular flight scenarios by means of volumetric flow measurements of a Flapping-Wing Micro Air Vehicle along its complete wake in a wind tunnel environment*"

To fulfill this main objective, the wake of the DelFly II is studied. The results from the experimental campaigns performed are the first volumetric information directly measured on the wake of this MAV. The flapping cycle is mainly divided into two phases: the instroke (the pairs of wings move towards each other) and the outstroke (the wings move away from each other). The measurements were limited to the wake of the DelFly and therefore the link between the vortex structures seen at the precise location of the wing when the structures are generated is lost. Nevertheless, a general idea of the situation of the wings can be extracted from the evolution of the lateral velocity (should go inwards during the outstroke and outwards during the instroke). Three different configurations are selected to compare the wake topologies at different conditions to observe the influence of reduce frequency. The final measurement volume achieved in tethered conditions is approximately $50 \times 30 \times 40\ cm^3$.

The 3D near wake of a FWMAV called DelFly II has been successfully captured in configurations simulating free-flight scenarios along the envelope of the MAV in forward flight, so the main objective of this project has been achieved. The wake has been experimentally investigated by means of a novel measurement technique, Robotic Volumetric Velocimetry. The first crucial objective of this study was to achieve steady and periodic velocity field along the different stages of the flapping cycle by means of a phase-averaging procedure, provided the particles information from Robotic Volumetric Velocimetry. This step has been successfully implemented. Once the complete process has been established, the main objective of this thesis can be accomplished. The goal of the present work is to characterize the flow field and the wake topology generated by the DelFly.

The main vortex structures found on the wake have been classified. The main vortex structures found are the tip vortices. The tip vortex in each side of the DelFly forms a continuous shape along the complete flapping cycle. It starts to develop at the beginning of the instroke in the upper wings and then, when the outstroke commences, the tip vortex is maintained and deflected downwards by

the lower wings. The fact that a continuous tip vortex is generated at each side indicates that the MAV is generated lift throughout the complete cycle. The tip vortex and all the other vortex structures are highly influenced by the acceleration produced by the pairs of flapping wings present on the DelFly. The acceleration creates high velocity regions on the body direction which are much higher than the freestream velocity. Therefore, the wake does not follow directly the direction of the freestream. There is an interaction between the freestream and the induced velocities from the wings so that the angle at which the wake is directed is a combination of the body direction and the direction of the freestream, which will depend of the importance of each component. The length of the wake generated during the instroke is slightly longer than the ones generated during the outstroke. This could be due to the larger acceleration of the flow being developed during the instroke. The deformation and the shape of the tip vortex will depend to a great extent on the reduced frequency. When the reduced frequency is low, the tip vortex is quite straight and aligned in the streamwise direction. When the reduce frequency becomes larger, an oblique vortex can be seen as the tip vortex cannot be clearly differentiated from the starting vortex. The starting vortex is generated at the beginning of the instroke. The upper wings start to generate a force as a consequence of a change in circulation on the wings. For circulation over the volume to be conserved, a starting vortex needs to be shed from the wing as a result. The starting vortex is predominantly generated perpendicular to the plane of symmetry of the DelFly. The close interaction between the tip vortex (streamwise direction) and the starting vortex (lateral direction) shows an oblique vortex.

Due to the deformation of the wings, additional vortex structures appear when the wings are closing together during the final part of the outstroke and the beginning of the instroke. The crossflow going from the tip to the root of the wings along the span needs to be redirected and the secondary vortices appear. The wings deformed during the outstroke creating a space that does not close until the instroke has already started, which allows the vortices to last until this gap disappears. When the reduced frequency increases, the deformation of the wings also becomes more prominent. Thus, the secondary vortices also become longer and stronger on the wake topology.

The tail of the DelFly, apart from being used for stability and maneuverability, it has been shown to enhance the preservation of the vortex structures mentioned above. The tail allows the flow to be less disturbed through that region and the vortex structures of the wake are more clearly defined.

A second big challenge on this investigation is the ability of performing measurements in free-flight conditions. The complexity of such measurements increased considerably, but meaningful results were achieved. Due to the inherent dynamic behaviour of the DelFly, only the larger and stronger vortex structures were captured. The vortex structures located closer to the center of the DelFly were not visualized correctly. The main vortex structure that was seen is the tip vortex. The topology of the tip vortex and the traces of other structures suggest a very similar topology that the one found in tethered conditions. However, a stronger interaction between the vortex structures from one flapping cycle to the next is augmented.

8.2. Recommendations

As the outcome of the present work has been successful, several path can be now taken to improve the tools and methods used as well as analyzing new configurations that given a broader understanding of the flapping wing mechanism. Considering new studies to be performed with the DelFly, a good way to achieve a better comparison between tethered and free-flight conditions would be to repeat the tethered experiments simulating exactly the conditions experienced during the free-flight tests performed during the course of this study. The ideal situation would be to carry out the experiments on the OJF to keep all the parameters identical. The OJF wind tunnel also gives the opportunity to measure a bigger volume around the DelFly due to its large cross-section. It will allow to measure a longer part of the wake which could be interesting for configurations such as number 3. To achieve information with better spatial resolutions, numerical techniques could be used such as the algorithm called VIC+ developed by Schneiders [75].

Now that the wake of the DelFly has been properly measured in 3D, the next challenge leads to the measurement of the flow behaviour before and along the wings. The major showstopper of this challenge is the intensity and variability of the reflections produced by the flapping wings when illuminated by laser light. The best way therefore to look at the flow going through the wings would be to locate the CVV probe along the body direction of the DelFly so that the surface of the wings seen by the cameras

is minimized. The camera could either be positioned in front of the wings or after. Ideally, placing them after the wings would reduce the influence that the measurement system has on the flow. Together with the flow measurements around the wings, the deformation of the DelFly wings could be studied at the same time to have the information of the structure, as well and the fluid. This would be a highly complex set-up which could lead to the two kind of measurements to be performed separately, but at the same conditions so that the results can be related. These kinds of measurements could also be used to compare with CFD simulations. For such exercise, the information for the deformation of the wing would be an input for the CFD which would later be compared to the results achieved experimentally. Another possibility to be attempted is the use of black wings instead of transparent ones. This would reduce to a certain extend the reflections generated by the wings, but it would also bring opacity so particles on the other side of the wing cannot be seen.

Together with the flow measurements, it will be of great importance to measure the forces generated by the DelFly at those conditions. This is a step towards understanding the link between the vortex structures developed and the final forces achieved by the motion of the DelFly. These kind of measurements have been performed in previous studies [18, 38, 61].

In addition, experiments in asymmetric conditions could be performed with a tethered DelFly to study the lateral behaviour of the vortex structures. A constant sideslip can be easily achieved by rotating the support structure. A rotating disk could be employed for such task. Due to the variation in between one side of the DelFly and the other, it would be beneficial to performed experiments positioning the CVV prove at each die of the MAV so that both are correctly measured. Another option is to change the DelFly arrangement so that is placed upside down (rotated 180 degrees along the body direction). When a certain angle of the body with respect to the freestream is desired, the change in the angle from one position to the other needs to be considered.

With respect to the measurement technique used, Robotic Volumetric Velocimetry, it would be interesting to develop further the data processing steps, in particular the phase-averaging performed in these measurements. To be able to perform more accurate measurement in free-flight conditions, the way the information from the DelFly position relates to the measurement volume seem by the CVV probe needs to be improved. For now, only a translation of the measurement volume to coincide with the DelFly body axis was used. But the DelFly also experiences rotations along its axes, especially in yaw (rotation around the vertical absolute axis). In that situation, the vortex structures are not shed parallel to the freestream. If this rotation is not taken into account, the topology at different instants will not match correctly. Another issue to be acknowledged is the time lag in between the position of the DelFly and the measurement of wake topology generated by the DelFly at that position. It would be beneficial to use the position of the DelFly at $t - \Delta t$ to relate it with the measurements performed at time t. The way to compute the time lag Δt is not trivial, but a first approximation can be performed with the information already analyzed.

A

Wind tunnel specifications

One of the challenges found when performing the experiments was related to the high turbulence of the flow at low speeds. The wind tunnel at such low speeds, raging from $0.5 - 2\ m/s$ for this study, are not completely reliable. In order to perform the experiments at the speed desired, previous PIV measurements were done on the free stream alone to characterize the wind tunnels at low speeds.

A.1. Wind tunnel setup for tethered experiments

The tethered experiments were performed in a low-speed wind tunnel at the Aerodynamic Laboratory of TU Delft, which has an open test section with cross-sectional dimensions of $60\ cm \times 60\ cm$ and a contraction ratio of 3.62. The contraction of the wind tunnel with this dimensions was built specifically for a set of experiments of the DelFly in 2012 [30]. The wind tunnel specifications for the new contraction were computed and the results can be seen in figure A.1.

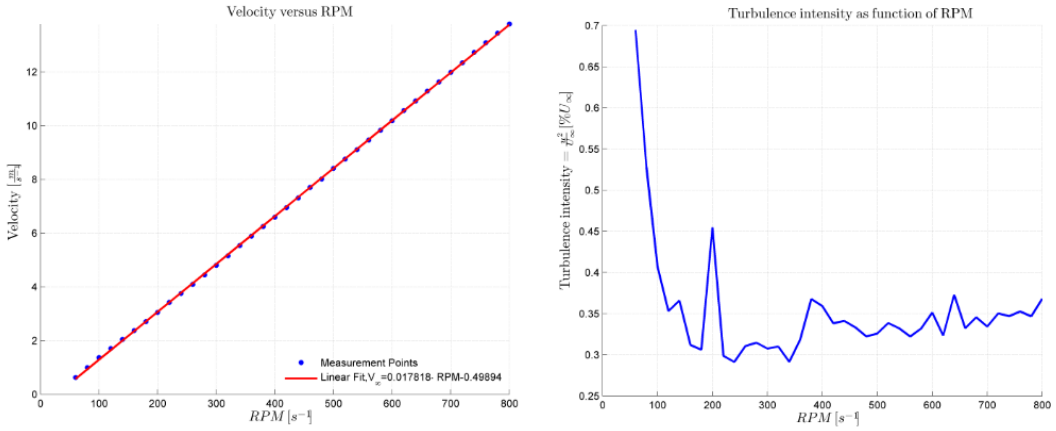

Figure A.1: Free stream velocity (left) and turbulence intensity (right) with respect to RPM [30]

However, the calibration done of the wind tunnel for the new contraction does not give a full view of the behaviour of the wind tunnel at low speeds. Therefore, several measurements of the freestream were performed at low RPM. The results have been plotted in figure A.2. Planar PIV is used for these measurements and an average over the measurement plane is computed to obtained the results. The resultant values of the measurement points can also be found on table A.1.

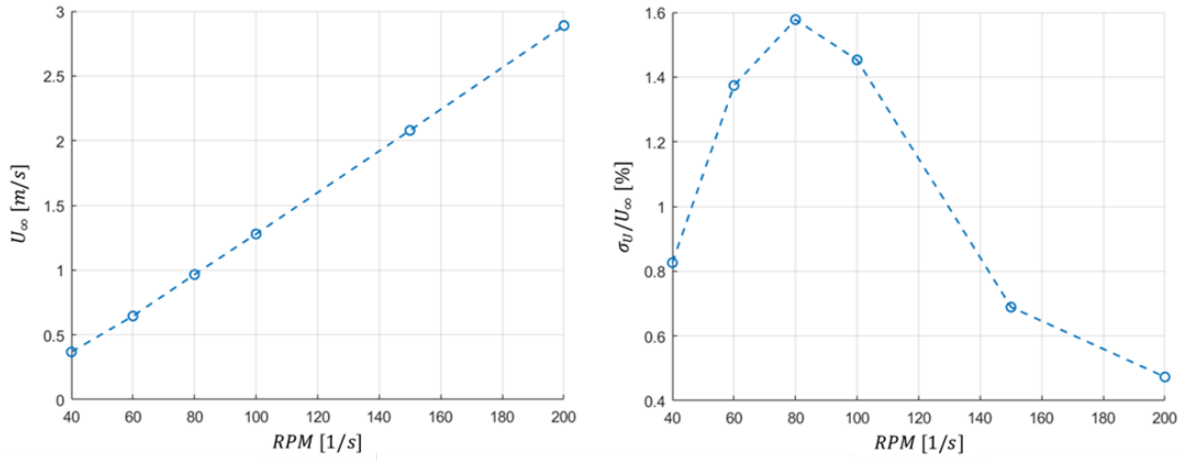

Figure A.2: Free stream velocity (left) and turbulence intensity (right) with respect to RPM at low speeds in W-tunnel

RPM [1/s]	**40**	**60**	**80**	**100**	**150**	**200**
U_∞ **[m/s]**	0.3678	0.6451	0.9657	1.2788	2.0793	2.8888
σ_U **[m/s]**	0.0030	0.0089	0.0152	0.0186	0.0143	0.0137

Table A.1: Freestream measurement results for W-tunnel at low speeds

A.2. Wind tunnel setup for free-flight experiments

The second experimental campaign was performed in the Open Jet Facility (OJF) of TU Delft, which is a relatively large-size wind tunnel with an open test section of $2.85 \times 2.85m^2$ cross section, and a contraction ratio of 3 (horizontal contraction of 1.88 and vertical one of 1.62). The test section leads to an open room that is 8 m high and it extends from 13 m until the flow goes through a cooling mesh at the end of the room and continues the cycle along the closed wind tunnel. The cooling mesh was not used for the experiments. The fan is powered by an electrical motor reaching 500 kW which allows a maximum free stream of 35 m/s. The free stream measurement equipment embedded in the wind tunnel is not reliable at speed lower than 5 m/s. As the flight speeds desired are significantly lower, measurements of the free stream need to be measured to compute the relation with fan rpm and the nominal turbulence intensity of the flow. The results can be found both in figure A.3 and in table 4.2.

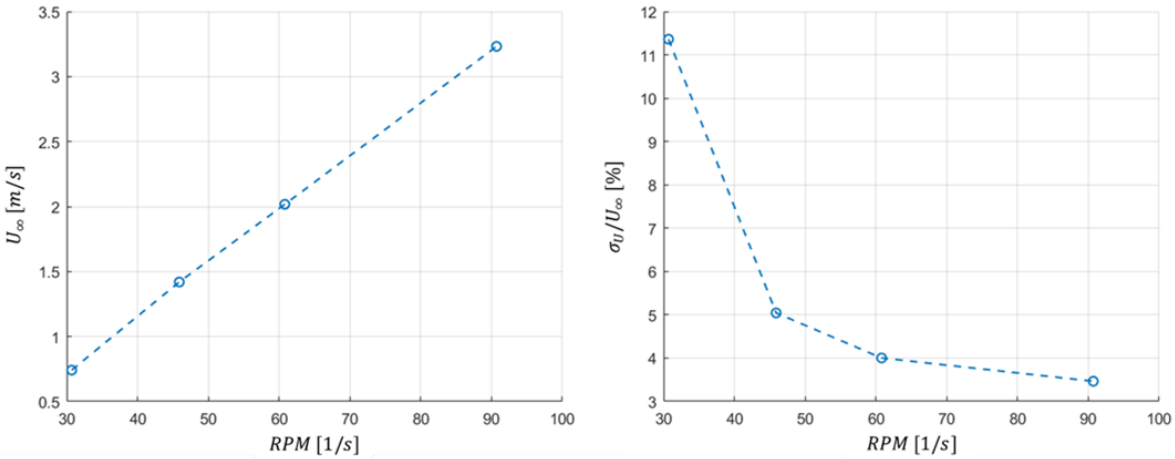

Figure A.3: Free stream velocity (left) and turbulence intensity (right) with respect to RPM at low speeds in OFJ

RPM [1/s]	**30.7**	**45.9**	**60.8**	**90.7**
U_∞ **[m/s]**	0.7418	1.4194	2.0174	3.2320
σ_U **[m/s]**	0.0843	0.0716	0.0808	0.1120

Table A.2: Freestream measurement results for W-tunnel at low speeds

B

Additional plots of the wake topology

Due to the large quantity of information that was recorded during this study, it was not possible to show the evolution of all the different quantities for all configurations analyzed. Once the evolution of velocity and vorticity was explained on one configuration, the comparison between different configurations was focused on the 3D wake topology, not going into detail about the 2D information available. You can find such information here where the plot from configuration 3 are available. The results from configuration 3TC with tail can be clearly compared to configuration 3TC without tail in section B.1. On section B.2, the analogy between tethered and free-flight conditions can be found.

B.1. Effect of presence of the tail

The phases of the measurements with tail do not match the ones without tail due to a phase lag in this case of half a cycle. This is the reason behind the numbering of the phases. The plots show the evolution of the velocity field on the direction of the body along the flapping cycle, as well as the development of vorticity on the out of plane out-of-plane direction.

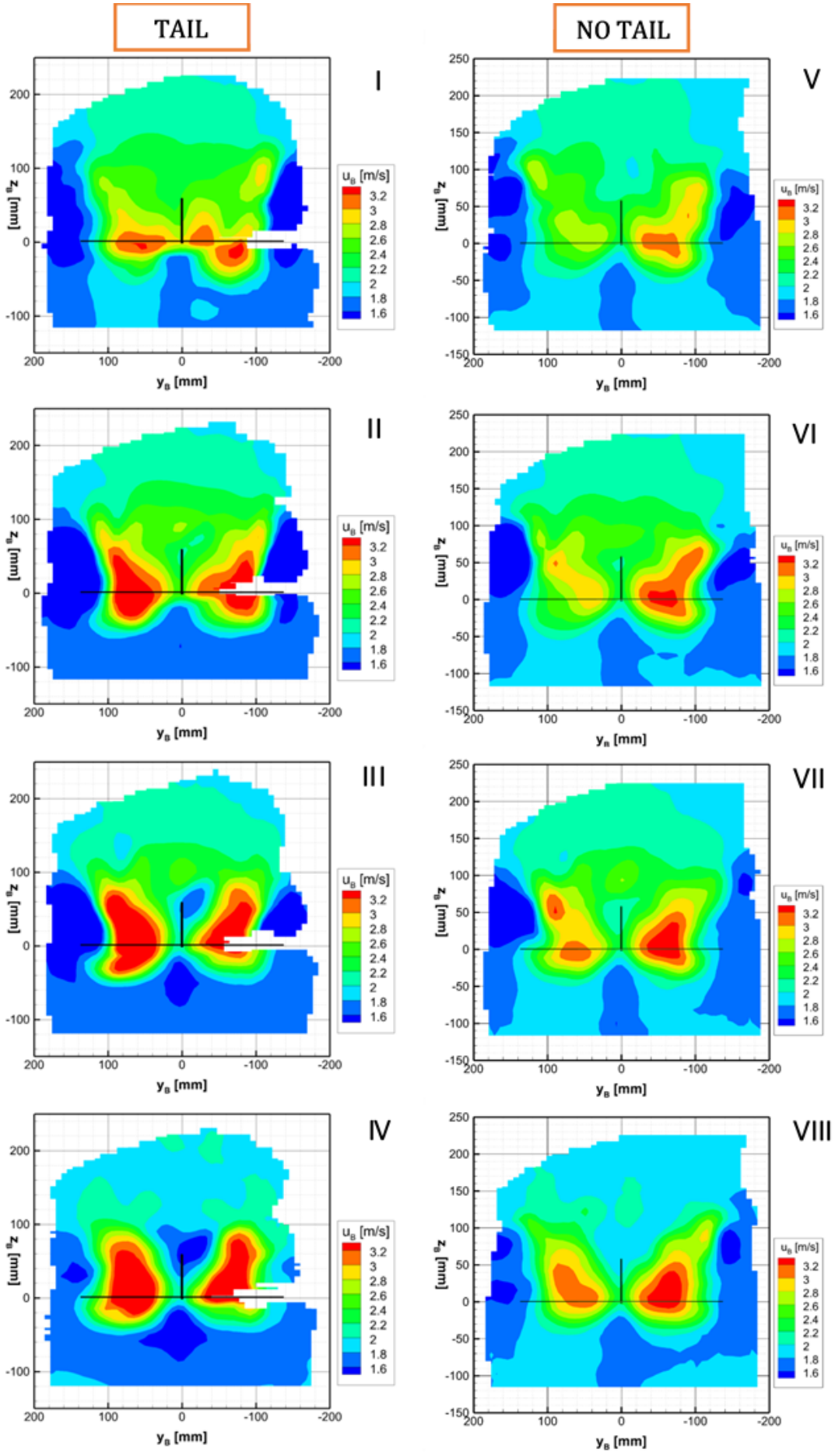

Figure B.1: Contour plots of the velocity component on the body direction in a spanwise oriented plane at 10 mm distance from the end of the tail at phases 1-4 for configuration 3TC with tail and phases 5-8 for configuration 3TC without tail.

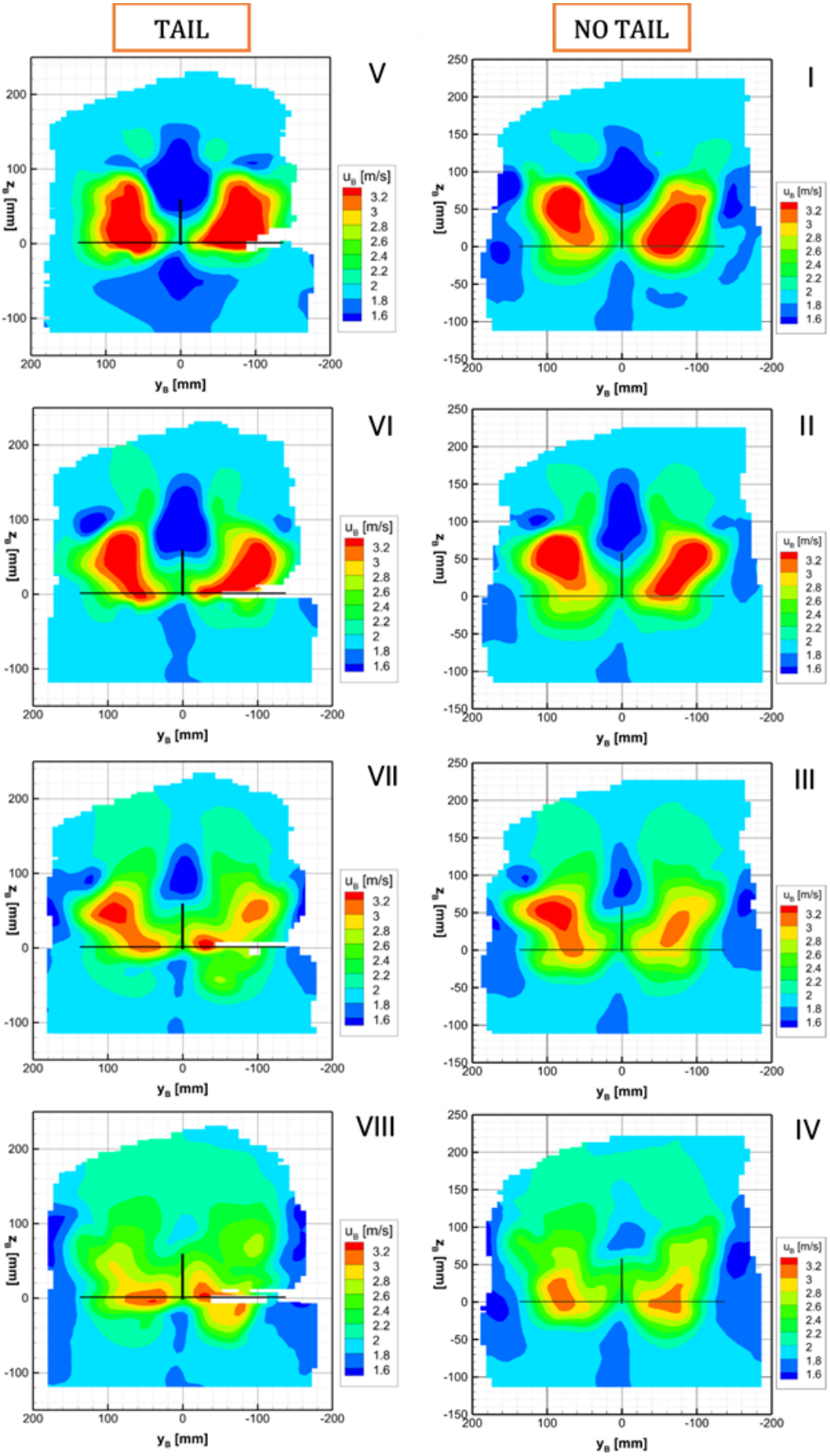

Figure B.2: Contour plots of the velocity component on the body direction in a spanwise oriented plane at 10 mm distance from the end of the tail at phases 5-8 for configuration 3TC with tail and phases 1-4 for configuration 3TC without tail.

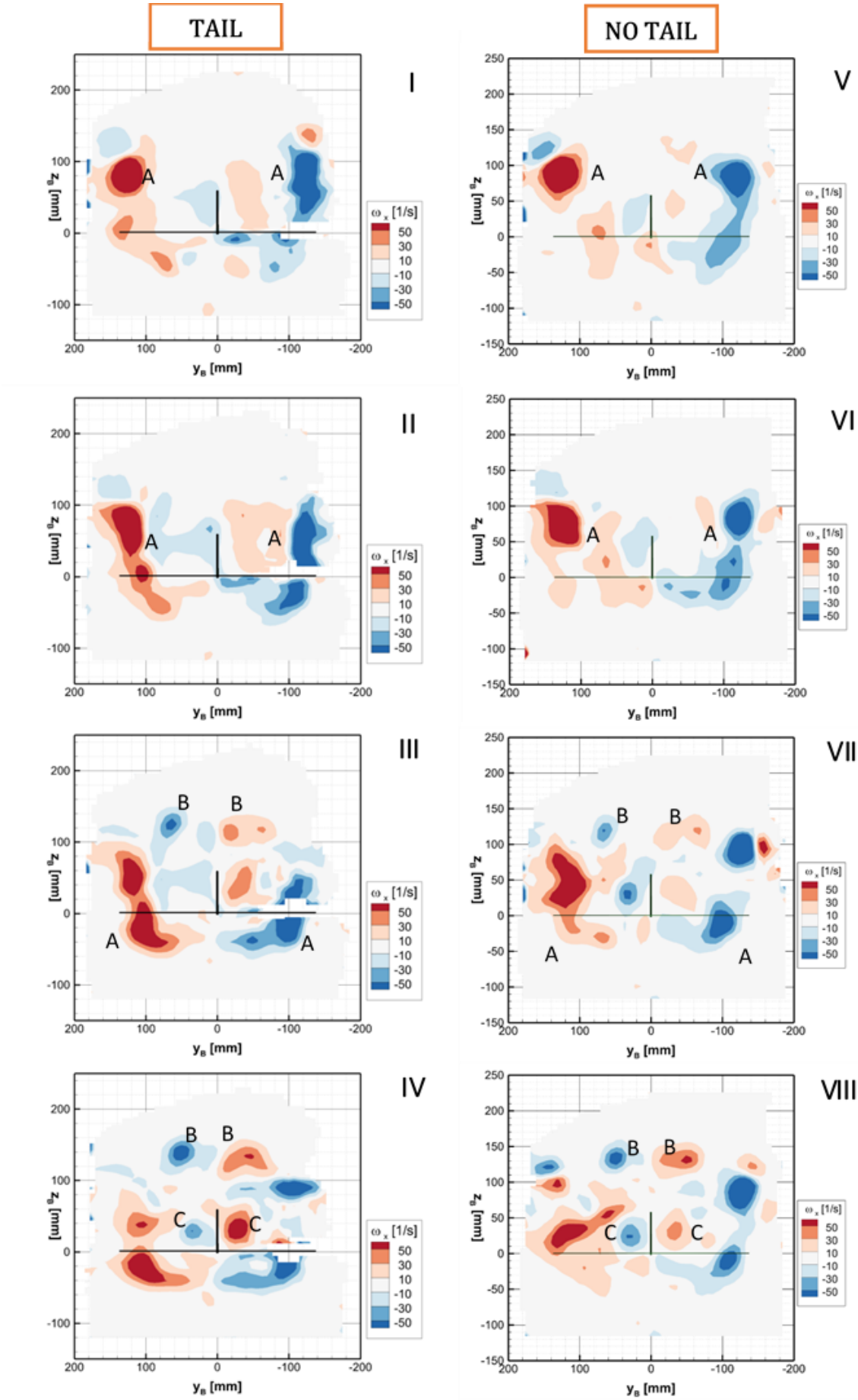

Figure B.3: Contour plots of the out-of-plane vorticity ω_x in a spanwise oriented plane at 10 mm distance from the end of the tail at phases 1-4 for configuration 3TC with tail and phases 5-8 for configuration 3TC without tail.

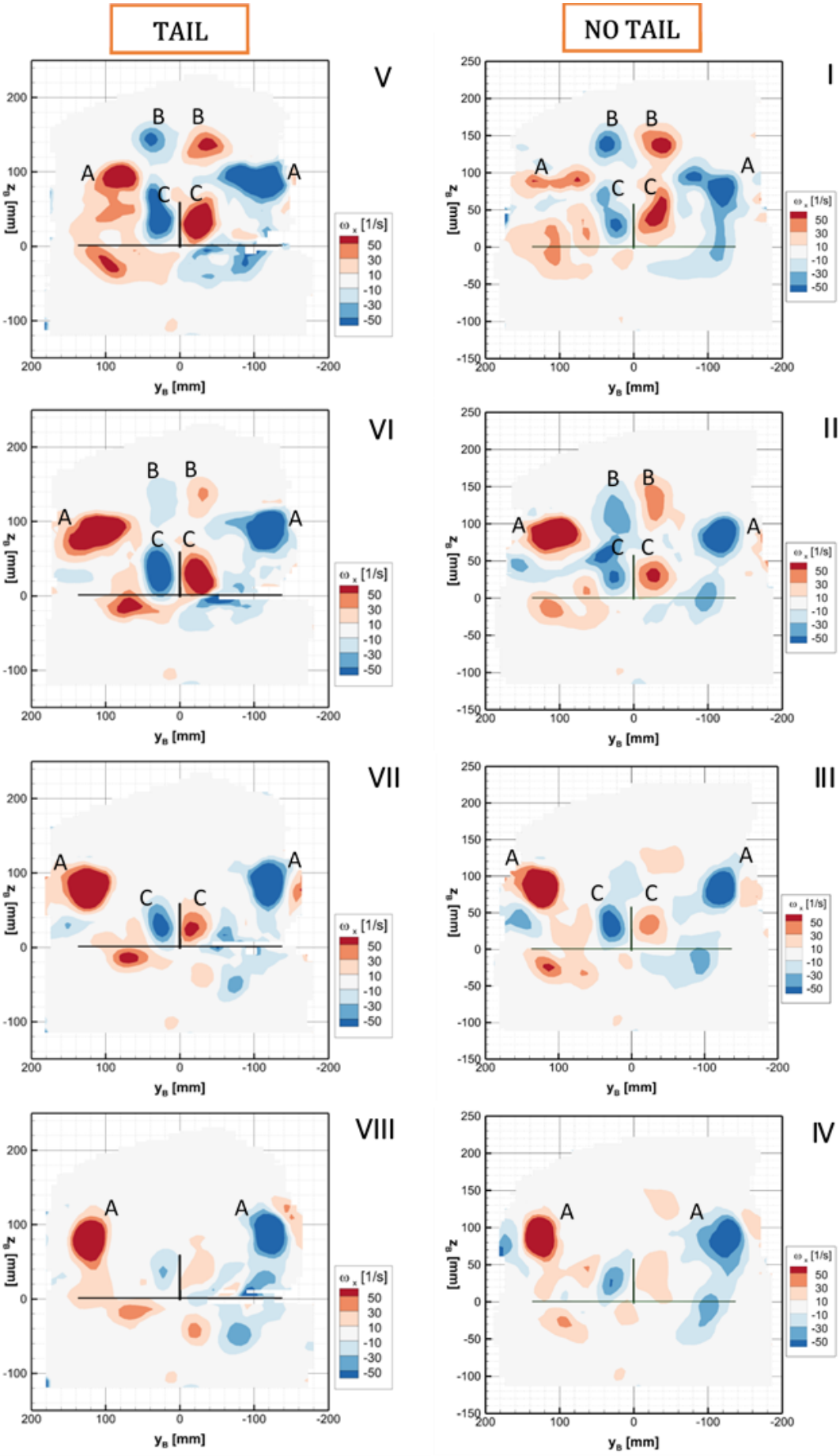

Figure B.4: Contour plots of the out-of-plane vorticity ω_x in a spanwise oriented plane at 10 mm distance from the end of the tail at phases 5-8 for configuration 3TC with tail and phases 1-4 for configuration 3TC without tail.

B.2. Effect of free flight conditions

The phases of the measurements in tethered conditions do not match the ones in free-flight conditions due to a phase lag in this case of quarter of a cycle. This is the reason behind the numbering of the phases. The plots show the evolution of the velocity field on the direction of the body along the flapping cycle, as well as the development of vorticity on the out of plane out-of-plane direction.

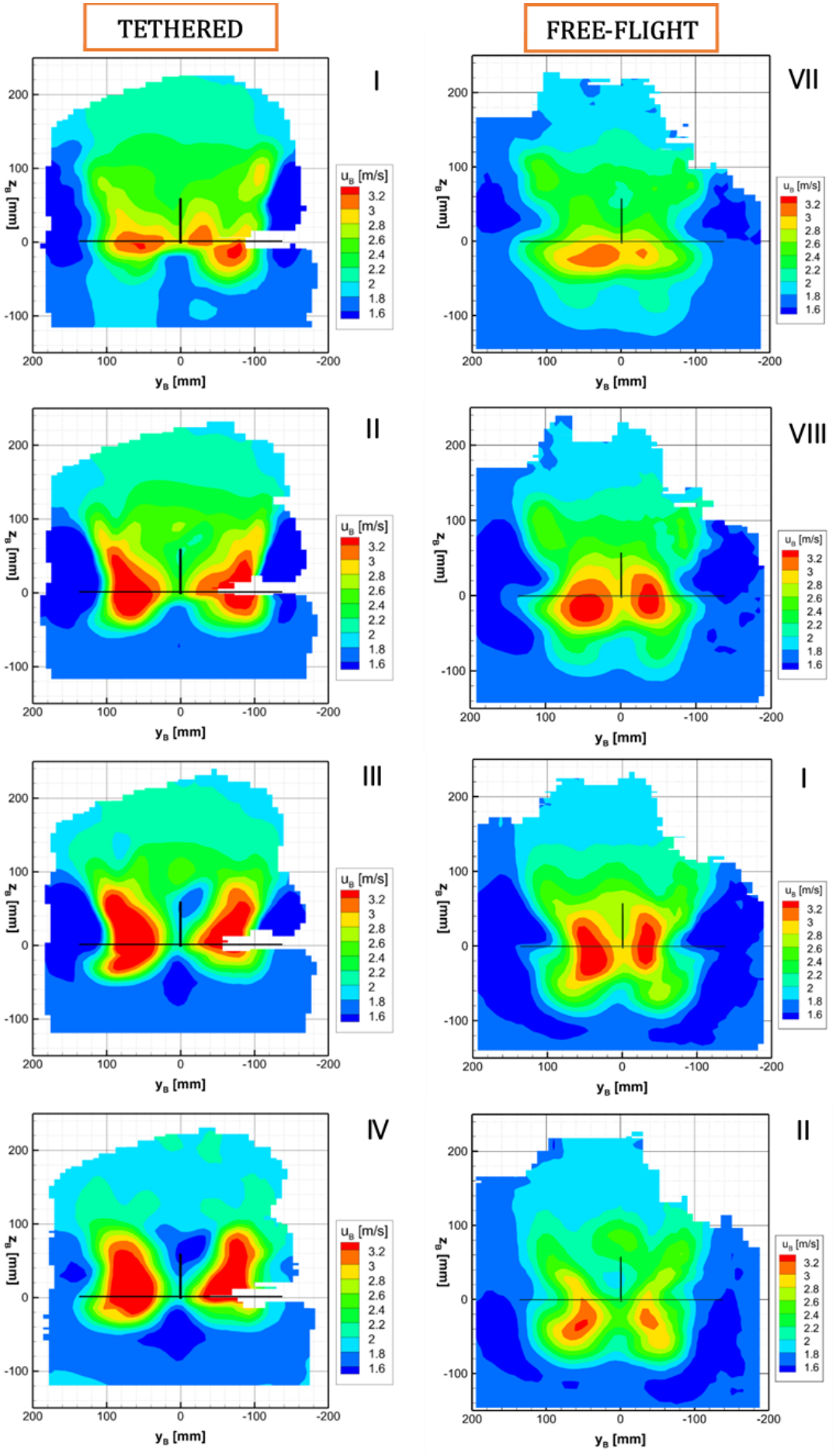

Figure B.5: Contour plots of the velocity component on the body direction in a spanwise oriented plane at 10 mm distance from the end of the tail at phases 1-4 for configuration 3TC and phases 7-2 for configuration 3FC.

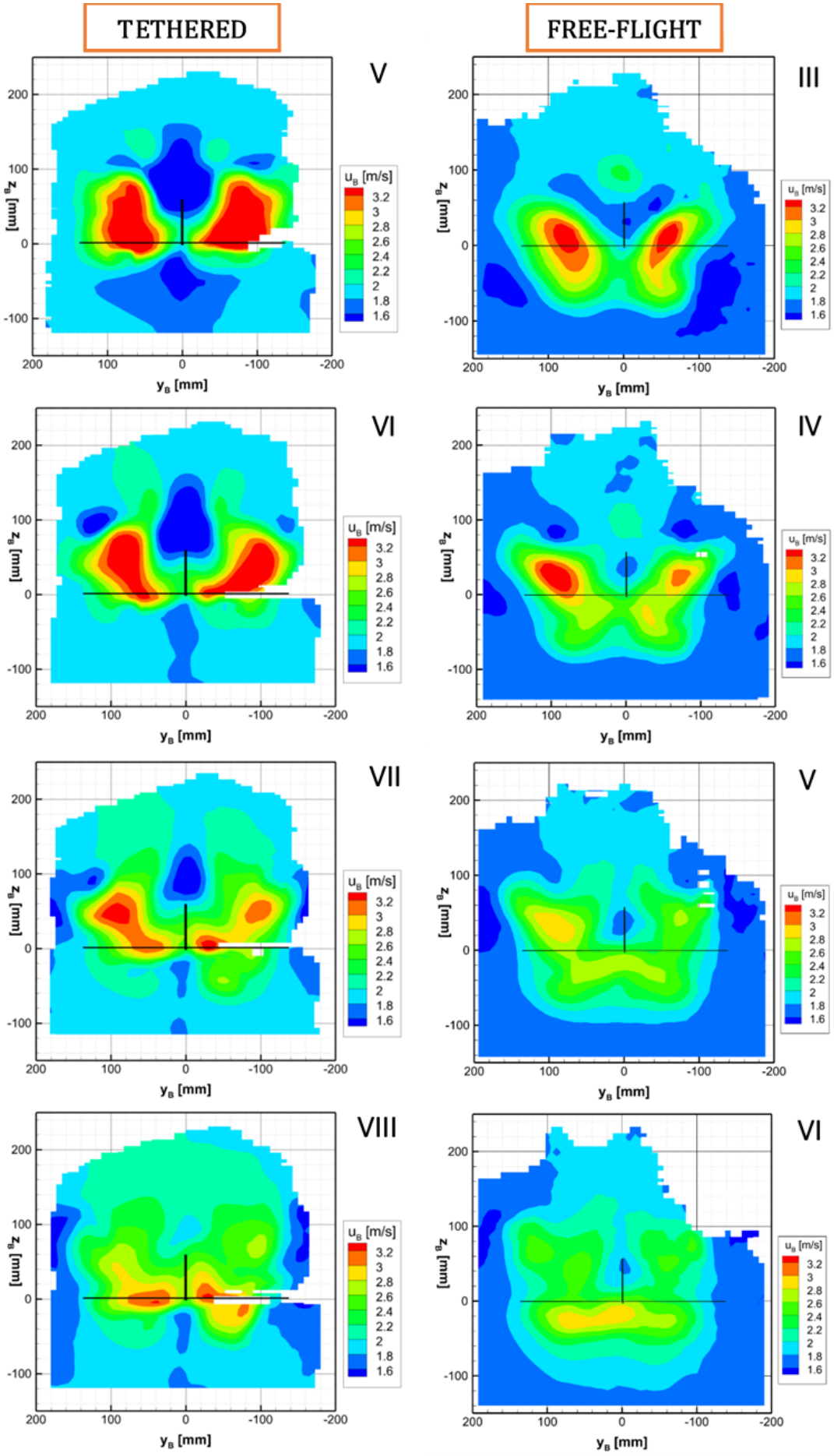

Figure B.6: Contour plots of the velocity component on the body direction in a spanwise oriented plane at 10 mm distance from the end of the tail at phases 5-8 for configuration 3TC and phases 3-6 for configuration 3FC.

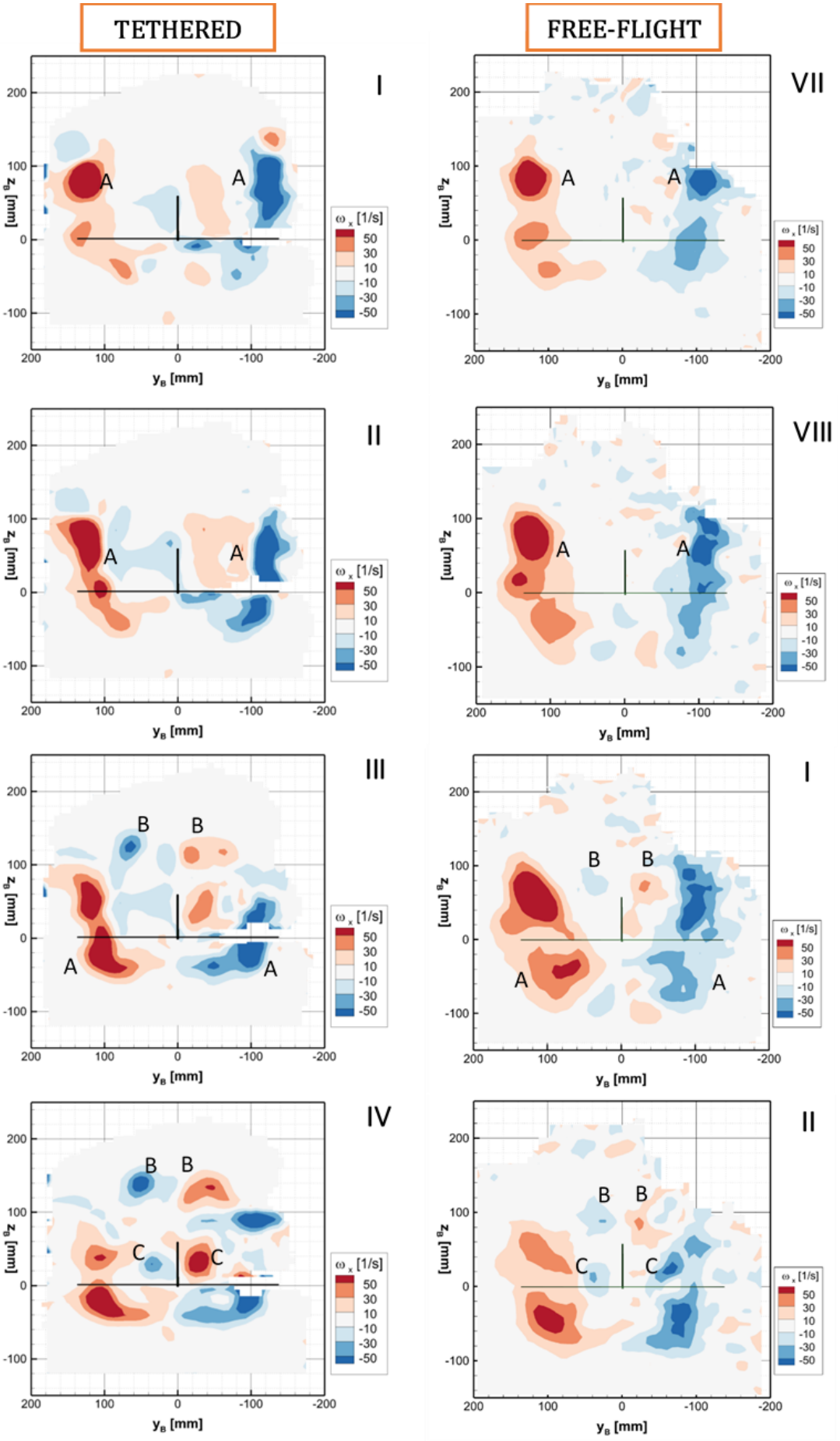

Figure B.7: Contour plots of the out-of-plane vorticity ω_x in a spanwise oriented plane at 10 mm distance from the end of the tail at phases 1-4 for configuration 3TC and phases 7-2 for configuration 3FC.

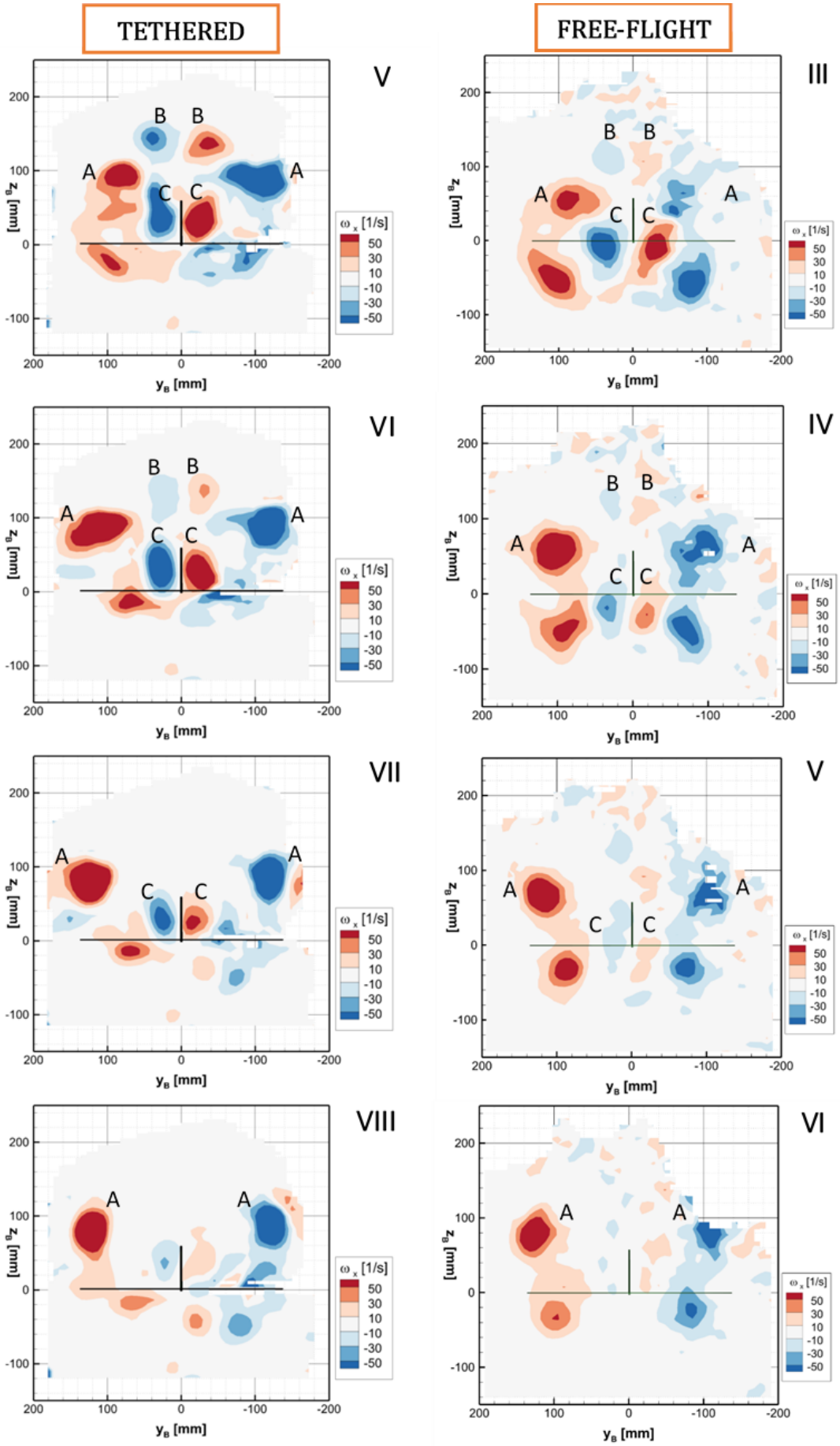

Figure B.8: Contour plots of the out-of-plane vorticity ω_x in a spanwise oriented plane at 10 mm distance from the end of the tail at phases 5-8 for configuration 3TC and phases 3-6 for configuration 3FC.

Bibliography

[1] Ronald J Adrian. Scattering particle characteristics and their effect on pulsed laser measurements of fluid flow: speckle velocimetry vs particle image velocimetry. *Applied Optics*, 23(11): 1690–1691, 1984. doi: 10.1364/AO.23.001690. URL http://ao.osa.org/abstract.cfm?URI=ao-23-11-1690.

[2] Ronald J Adrian, C Meinhart, and C Tomkins. Vortex organisation in the outer region of the turbulent boundary layer. *Journal of Fluid Mechanics*, 422:1–54, 2000. doi: https://doi.org/10.1017/S0022112000001580.

[3] Nereida Agüera, Gioacchino Cafiero, Tommaso Astarita, and Stefano Discetti. Ensemble 3D PTV for high resolution turbulent statistics. *Measurement Science and Technology*, 27(12), 2016. ISSN 13616501. doi: 10.1088/0957-0233/27/12/124011.

[4] S. F. Armanini, J. V. Caetano, G. C.H.E.De Croon, C. C.De Visser, and M. Mulder. Quasi-steady aerodynamic model of clap-and-fling flapping MAV and validation using free-flight data. *Bioinspiration and Biomimetics*, 11(4), 2016. ISSN 17483190. doi: 10.1088/1748-3190/11/4/046002.

[5] J. M. Birch. Force production and flow structure of the leading edge vortex on flapping wings at high and low Reynolds numbers. *Journal of Experimental Biology*, 207(7):1063–1072, 2004. ISSN 0022-0949. doi: 10.1242/jeb.00848. URL http://jeb.biologists.org/cgi/doi/10.1242/jeb.00848.

[6] James M Birch and Michael H Dickinson. Spanwise flow and the attachment of the leading-edge vortex on insect wings. *Nature*, 412:729, aug 2001. URL http://dx.doi.org/10.1038/35089071http://10.0.4.14/35089071.

[7] Felipe Bohorquez and Darryll Pines. Hover Performance of Rotor Blades at Low Reynolds Numbers for Rotary Wing Micro Air Vehicles. In *2nd AIAA "Unmanned Unlimited" Conf. and Workshop & Exhibit*, Infotech@Aerospace Conferences. American Institute of Aeronautics and Astronautics, sep 2003. doi: doi:10.2514/6.2003-6655. URL https://doi.org/10.2514/6.2003-6655.

[8] R. J. Bomphrey. The aerodynamics of Manduca sexta: digital particle image velocimetry analysis of the leading-edge vortex. *Journal of Experimental Biology*, 208(6):1079–1094, 2005. ISSN 0022-0949. doi: 10.1242/jeb.01471. URL http://jeb.biologists.org/cgi/doi/10.1242/jeb.01471.

[9] R. J Bomphrey, G. K Taylor, N. J Lawson, and A. L.R Thomas. Digital particle image velocimetry measurements of the downwash distribution of a desert locust Schistocerca gregaria. *Journal of The Royal Society Interface*, 3(7):311–317, 2006. ISSN 1742-5689. doi: 10.1098/rsif.2005.0090. URL http://rsif.royalsocietypublishing.org/cgi/doi/10.1098/rsif.2005.0090.

[10] Richard J. Bomphrey, Nicholas J. Lawson, Graham K. Taylor, and Adrian L R Thomas. Application of digital particle image velocimetry to insect aerodynamics: Measurement of the leading-edge vortex and near wake of a Hawkmoth. *Experiments in Fluids*, 40(4):546–554, 2006. ISSN 07234864. doi: 10.1007/s00348-005-0094-5.

[11] Richard J. Bomphrey, Per Henningsson, Dirk Michaelis, and David Hollis. Tomographic particle image velocimetry of desert locust wakes: Instantaneous volumes combine to reveal hidden vortex elements and rapid wake deformation. *Journal of the Royal Society Interface*, 9 (77):3378–3386, 2012. ISSN 17425662. doi: 10.1098/rsif.2012.0418. URL http://rsif.royalsocietypublishing.org/cgi/doi/10.1098/rsif.2012.0418.

[12] Frank M Bos, Bas W van Oudheusden, and Hester Bijl. Radial basis function based mesh deformation applied to simulation of flow around flapping wings. *Computers & Fluids*, 79:167–177, 2013. ISSN 0045-7930. doi: https://doi.org/10.1016/j.compfluid.2013.02.004. URL http://www.sciencedirect.com/science/article/pii/S0045793013000583.

[13] Xiaodong Tian Breuer, Jose Iriarte-Diaz, Kevin Middleton, Ricardo Galvao, Emily Israeli, Abigail Roemer, Allyce Sullivan, Arnold Song, Sharon Swartz, and Kenneth. Direct measurements of the kinematics and dynamics of bat flight. *Bioinspiration & Biomimetics*, 1(4):S10, 2006. ISSN 1748-3190. URL http://stacks.iop.org/1748-3190/1/i=4/a=S02.

[14] Giuseppe Carlo Alp Caridi, Daniele Ragni, Andrea Sciacchitano, and Fulvio Scarano. HFSB-seeding for large-scale tomographic PIV in wind tunnels. *Experiments in Fluids*, 57(12), 2016. ISSN 07234864. doi: 10.1007/s00348-016-2277-7.

[15] Giuseppe Carlo Alp Caridi, Andrea Sciacchitano, and Fulvio Scarano. Helium-filled soap bubbles for vortex core velocimetry. *Experiments in Fluids*, 58(9):1–12, 2017. ISSN 07234864. doi: 10.1007/s00348-017-2415-x.

[16] Huai-yu CHENG, Xin-ping LONG, Bin JI, Ye ZHU, and Jia-jian ZHOU. Numerical investigation of unsteady cavitating turbulent flows around twisted hydrofoil from the Lagrangian viewpoint. *Journal of Hydrodynamics, Ser. B*, 28(4):709–712, 2016. ISSN 1001-6058. doi: https://doi.org/10.1016/S1001-6058(16)60674-1. URL http://www.sciencedirect.com/science/article/pii/S1001605816606741.

[17] Pakpong Chirarattananon, Kevin Y. Ma, and Robert J. Wood. Single-loop control and trajectory following of a flapping-wing microrobot. *Proceedings - IEEE International Conference on Robotics and Automation*, pages 37–44, 2014. ISSN 10504729. doi: 10.1109/ICRA.2014.6906587.

[18] KME De Clercq and R De Kat. Flow visualization and force measurements on a hovering flapping-wing MAV'DelFly II'. *Proc. 39th AIAA Fluid …*, (June):1–10, 2009. doi: 10.2514/6.2009-4035. URL http://arc.aiaa.org/doi/pdf/10.2514/6.2009-4035.

[19] Torbjørn Cunis and Dr-Ing Dieter Moormann Dr-Ing Norbert Siepenkötter dr Guido CHE de Croon. Precise Position Control of a Flapping-wing Micro Air Vehicle in a Wind-tunnel. 2016.

[20] G.C.H.E. de Croon, K.M.E. de Clercq, R. Ruijsink, B. Remes, and C. de Wagter. Design, Aerodynamics, and Vision-Based Control of the DelFly. *International Journal of Micro Air Vehicles*, 1(2):71–97, 2009. ISSN 1756-8293. doi: 10.1260/175682909789498288. URL http://journals.sagepub.com/doi/10.1260/175682909789498288.

[21] G.C.H.E. de Croon, M Perçin, B.D.W. Remes, R Ruijsink, and C De Wagter. *The DelFly*. 2016. ISBN 978-94-017-9207-3. doi: 10.1007/978-94-017-9208-0. URL http://link.springer.com/10.1007/978-94-017-9208-0.

[22] Alejandro Del and Estal Herrero. *Experimental Aerodynamics of Flapping Wings Aerodynamics of the DelFly II*. PhD thesis, 2017.

[23] Coen Den berg and Charles P Ellington. The vortex wake of a 'hovering'model hawkmoth. *Philosophical Transactions of the Royal Society of London. Series B: Biological Sciences*, 352(1351): 317–328, 1997. ISSN 0962-8436.

[24] S. Deng. *Aerodynamics of flapping-wing Micro-Air-Vehicle: An integrated experimental and numerical study*. PhD thesis, 2016. URL http://repository.tudelft.nl/view/ir/uuid{%}3Ab1abe278-bb42-481b-bc5b-7af53424bc75/.

[25] S Deng, M Percin, B W van Oudheusden, H Bijl, B Remes, and T Xiao. Numerical Simulation of a Flexible X-Wing Flapping-Wing Micro Air Vehicle. *AIAA Journal*, 55(7):2295–2306, may 2017. ISSN 0001-1452. doi: 10.2514/1.J054816. URL https://doi.org/10.2514/1.J054816.

[26] Shuanghou Deng, Tianhang Xiao, Bas van Oudheusden, and Hester Bijl. Numerical Investigation on the Propulsive Performance of Biplane Counter-Flapping Wings. *International Journal of Micro Air Vehicles*, 7(4):431–439, 2015. ISSN 1756-8293. doi: 10.1260/1756-8293.7.4.431. URL http://journals.sagepub.com/doi/10.1260/1756-8293.7.4.431.

[27] Shuanghou Deng, Mustafa Percin, and Bas van Oudheusden. Experimental Investigation of Aerodynamics of Flapping-Wing Micro-Air-Vehicle by Force and Flow-Field Measurements. *AIAA Journal*, 54(2):588–602, 2016. ISSN 0001-1452. doi: 10.2514/1.J054403. URL http://arc.aiaa.org/doi/10.2514/1.J054403.

[28] Michael H. Dickinson and Karl Götz. Unsteady aerodynamic performance of model wings at low reynolds numbers. *J. exp. Biol.*, 174:45–64, 1993. ISSN 0022-0949. doi: 10.1242/jeb.00739.

[29] Michael H Dickinson, Fritz-Olaf Lehmann, and Sanjay P Sane. Wing Rotation and the Aerodynamics Basis of Insect Flight. *Science*, 284(1999):1954–1960, 1999. ISSN 00368075. doi: 10.1126/science.284.5422.1954. URL http://www.sciencemag.org/cgi/doi/10.1126/science.284.5422.1954.

[30] H E Eisma. Flow visualization in the wake of flapping-wing MAV 'DelFly II' in forward flight. pages 1–12 BT – Online Publication, 2012. URL http://dx.doi.org/10.2514/6.2012-2664.

[31] C. P. Ellington. The aerodynamics of hovering insect flight. IV. Aerodynamic mechanisms. *Philosophical Transactions of the Royal Society of London. B, Biological Sciences*, 305(1122):79 LP – 113, feb 1984. URL http://rstb.royalsocietypublishing.org/content/305/1122/79.abstract.

[32] Charles P Ellington, Coen van den Berg, Alexander P Willmott, and Adrian L R Thomas. Leading-edge vortices in insect flight. *Nature*, 384:626, dec 1996. URL http://dx.doi.org/10.1038/384626a0http://10.0.4.14/384626a0.

[33] G. E. Elsinga, F. Scarano, B. Wieneke, and B. W. Van Oudheusden. Tomographic particle image velocimetry. *Experiments in Fluids*, 41(6):933–947, 2006. ISSN 07234864. doi: 10.1007/s00348-006-0212-z.

[34] D Engler Faleiros, Marthijn Tuinstra, A Sciacchitano, and F Scarano. Generation and control of helium-filled soap bubbles for large-scale PIV. In *LXLASER2018: 19th International Symposium on the Application of Laser and Imaging Techniques to Fluid Mechanics*, 2018.

[35] Daniel J Garmann, Miguel R Visbal, and Paul D Orkwis. Three-dimensional flow structure and aerodynamic loading on a revolving wing. *Physics of Fluids*, 25(3):34101, 2013.

[36] D Giaquinta. Masters Thesis: The Flow Topology of the Ahmed Body in Cross-Wind. 2018.

[37] M Groen. PIV and force measurements on the flapping-wing MAV DelFly II. *MS thesis*, (December 2010), 2010. URL http://scholar.google.com/scholar?hl=en{&}btnG=Search{&}q=intitle:PIV+and+force+measurements+on+the+flapping-wing+MAV+DelFly+II{#}0.

[38] Mark Groen, Bart Bruggeman, Hester Bijl Mark Groen, Bart Bruggeman, Bart Remes, Rick Ruijsink, Bas van Oudheusden, and Bart Remes. Improving flight performance of the flapping wing MAV DelFly II. *Int. Micro Air Vehicle …*, 2010.

[39] Eric Gutierrez, Daniel B. Quinn, Diana D. Chin, and David Lentink. Lift calculations based on accepted wake models for animal flight are inconsistent and sensitive to vortex dynamics. *Bioinspiration and Biomimetics*, 12(1):1–15, 2017. ISSN 17483190. doi: 10.1088/1748-3190/12/1/016004. URL http://dx.doi.org/10.1088/1748-3190/12/1/016004.

[40] Per Henningsson, Dirk Michaelis, Toshiyuki Nakata, Daniel Schanz, Reinhard Geisler, Andreas Schröder, and Richard J. Bomphrey. The complex aerodynamic footprint of desert locusts revealed by large-volume tomographic particle image velocimetry. *Journal of the Royal Society Interface*, 12(108), 2015. ISSN 17425662. doi: 10.1098/rsif.2015.0119.

[41] Gabor T Herman and Arnold Lent. Iterative reconstruction algorithms. *Computers in biology and medicine*, 6(4):273–294, 1976.

[42] J C R Hunt, A A Wray, and P Moin. Eddies, streams, and convergence zones in turbulent flows. *Center for Turbulence Research Report. Proceedings of the 1988 Summer Program*, (89N24555), 1988.

[43] Jinhee Jeong and Fazle Hussain. On the identification of a vortex. *Fluid Mechanics*, 285:69–94, 1995. doi: 10.1017/S0022112095000462.

[44] Constantin Jux. *Robotic Volumetric Particle Tracking Velocimetry by Coaxial Imaging and Illumination*. PhD thesis, TU Delft, 2017.

[45] Constantin Jux, Andrea Sciacchitano, Jan F.G. Schneiders, and Fulvio Scarano. Robotic volumetric PIV of a full-scale cyclist. *Experiments in Fluids*, 59(4), 2018. ISSN 07234864. doi: 10.1007/s00348-018-2524-1.

[46] Matěj Karásek, Andries J. Koopmans, Sophie F. Armanini, Bart D.W. Remes, and Guido C.H.E. De Croon. Free flight force estimation of a 23.5 g flapping wing MAV using an on-board IMU. In *IEEE International Conference on Intelligent Robots and Systems*, 2016. ISBN 9781509037629. doi: 10.1109/IROS.2016.7759729.

[47] Matěj Karásek, Mustafa Percin, Torbjørn Cunis, Bas W. van Oudheusden, Christophe De Wagter, Bart D. W. Remes, and Guido C. H. E. de Croon. First free-flight flow visualisation of a flapping-wing robot. 2016. URL http://arxiv.org/abs/1612.07645.

[48] Matthew Keennon, Karl Klingebiel, and Henry Won. Development of the Nano Hummingbird: A Tailless Flapping Wing Micro Air Vehicle. In *50th AIAA Aerospace Sciences Meeting including the New Horizons Forum and Aerospace Exposition*, Aerospace Sciences Meetings. American Institute of Aeronautics and Astronautics, jan 2012. doi: doi:10.2514/6.2012-588. URL https://doi.org/10.2514/6.2012-588.

[49] F.-O. Lehmann. The aerodynamic effects of wing-wing interaction in flapping insect wings. *Journal of Experimental Biology*, 208(16):3075–3092, 2005. ISSN 0022-0949. doi: 10.1242/jeb.01744. URL http://jeb.biologists.org/cgi/doi/10.1242/jeb.01744.

[50] D. Lentink and M. H. Dickinson. Rotational accelerations stabilize leading edge vortices on revolving fly wings. *Journal of Experimental Biology*, 212(16):2705–2719, 2009. ISSN 0022-0949. doi: 10.1242/jeb.022269. URL http://jeb.biologists.org/cgi/doi/10.1242/jeb.022269.

[51] L. E.M. Lignarolo, D. Ragni, C. Krishnaswami, Q. Chen, C. J. Simão Ferreira, and G. J.W. van Bussel. Experimental analysis of the wake of a horizontal-axis wind-turbine model. *Renewable Energy*, 70:31–46, 2014. ISSN 09601481. doi: 10.1016/j.renene.2014.01.020. URL http://dx.doi.org/10.1016/j.renene.2014.01.020.

[52] H. G. Maas, A. Gruen, and D. Papantoniou. Particle tracking velocimetry in three-dimensional flows - Part 1. Photogrammetric determination of particle coordinates. *Experiments in Fluids*, 15 (2):133–146, 1993. ISSN 07234864. doi: 10.1007/BF00190953.

[53] Antoine Magnan. *Le vol des insectes*. Hermann, 1934.

[54] James H Marden. Maximum lift production during takeoff in flying animals. *Journal of Experimental Biology*, 130(1):235–238, 1987. ISSN 0022-0949. URL http://jeb.biologists.org/content/130/1/235.

[55] Roland Meynart. Instantaneous velocity field measurements in unsteady gas flow by speckle velocimetry. *Applied Optics*, 22(4):535–540, 1983. doi: 10.1364/AO.22.000535. URL http://ao.osa.org/abstract.cfm?URI=ao-22-4-535.

[56] M Moriche. A numerical study on the aerodynamic forces and the wake stability of flapping flight at low Reynolds number. 2017.

[57] Thomas J Mueller. *Fixed and flapping wing aerodynamics for micro air vehicle applications*. American Institute of Aeronautics and Astronautics, 2001.

[58] Florian T Muijres, L Christoffer Johansson, York Winter, and Anders Hedenström. Leading edge vortices in lesser long-nosed bats occurring at slow but not fast flight speeds. *Bioinspiration & Biomimetics*, 9(2):25006, 2014. URL http://stacks.iop.org/1748-3190/9/i=2/a=025006.

[59] T. Nakata, H. Liu, Y. Tanaka, N. Nishihashi, X. Wang, and A. Sato. Aerodynamics of a bio-inspired flexible flapping-wing micro air vehicle. *Bioinspiration and Biomimetics*, 6(4), 2011. ISSN 17483182. doi: 10.1088/1748-3182/6/4/045002.

[60] M. Percin, B. W. van Oudheusden, H. E. Eisma, and B. D.W. Remes. Three-dimensional vortex wake structure of a flapping-wing micro aerial vehicle in forward flight configuration. *Experiments in Fluids*, 2014. ISSN 07234864. doi: 10.1007/s00348-014-1806-5.

[61] M. Percin, B. W.Van Oudheusden, G. C.H.E.D. Croon, and B. Remes. Force generation and wing deformation characteristics of a flapping-wing micro air vehicle 'DelFly II' in hovering flight. *Bioinspiration and Biomimetics*, 11(3), 2016. ISSN 17483190. doi: 10.1088/1748-3190/11/3/036014.

[62] Mustafa Percin. *Aerodynamic Mechanisms of Flapping Flight*. PhD thesis, TU Delft, 2015.

[63] Francisco Pereira, Heinrich Stüer, Emilio C. Graft, and Morteza Gharib. Two-frame 3D particle tracking. *Measurement Science and Technology*, 17(7):1680–1692, 2006. ISSN 13616501. doi: 10.1088/0957-0233/17/7/006.

[64] Markus Raffel, C E Willert, S T Wereley, and Jürgen Kompenhans. *Particle Image Velocimetry*, volume 79. 2007. ISBN 9783540723073. doi: 10.1007/978-3-540-72308-0.

[65] J M V Rayner. A vortex theory of animal flight. Part 1. The vortex wake of a hovering animal. *Journal of Fluid Mechanics*, 91(4):697–730, 1979. doi: 10.1017/S0022112079000410.

[66] S. P. Sane. The aerodynamics of insect flight. *Journal of Experimental Biology*, 206(23):4191–4208, 2003. ISSN 0022-0949. doi: 10.1242/jeb.00663. URL http://jeb.biologists.org/cgi/doi/10.1242/jeb.00663.

[67] S. P. Sane. Induced airflow in flying insects II. Measurement of induced flow. *Journal of Experimental Biology*, 209(1):43–56, 2006. ISSN 0022-0949. doi: 10.1242/jeb.01958. URL http://jeb.biologists.org/cgi/doi/10.1242/jeb.01958.

[68] Sanjay P Sane and Michael H Dickinson. the Control of Flight Force By a Flapping Wing : Lift and Drag Production. *Journal of Experimental Biology*, 2626(15):2607–2626, 2001. ISSN 0022-0949, 1477-9145. doi: 10.1111/J.1365-3032.1978.TB00148.X. URL http://jeb.biologists.org/content/204/15/2607{%}5Cnhttp://jeb.biologists.org/content/204/15/2607.abstract{%}5Cnhttp://jeb.biologists.org/content/204/15/2607.full.pdf{%}5Cnhttp://www.ncbi.nlm.nih.gov/pubmed/11533111.

[69] Edoardo Saredi. Extending the velocity range of Robotic Volumetric PIV. 2018.

[70] Andrea Sciacchitano Scarano and Fulvio. Elimination of PIV light reflections via a temporal high pass filter. *Measurement Science and Technology*, 25(8):84009, 2014. ISSN 0957-0233. URL http://stacks.iop.org/0957-0233/25/i=8/a=084009.

[71] F. Scarano. Tomographic PIV: Principles and practice. *Measurement Science and Technology*, 24(1), 2013. ISSN 13616501. doi: 10.1088/0957-0233/24/1/012001.

[72] Fulvio Scarano, Sina Ghaemi, Giuseppe Carlo Alp Caridi, Johannes Bosbach, Uwe Dierksheide, and Andrea Sciacchitano. On the use of helium-filled soap bubbles for large-scale tomographic PIV in wind tunnel experiments. *Experiments in Fluids*, 56(2), 2015. ISSN 07234864. doi: 10.1007/s00348-015-1909-7.

[73] D Schanz, S Gesemann, A Schröder, and B Wienecke. Particle Reconstruction with Optical Transfer Functions Applied to Tomo-PIV-Experiments. In *New Results in Numerical and Experimental Fluid Mechanics VIII*, pages 623–631. Springer, 2013.

[74] Daniel Schanz, Sebastian Gesemann, and Andreas Schröder. Shake-The-Box: Lagrangian particle tracking at high particle image densities. *Experiments in Fluids*, 57(5):70, may 2016. ISSN 0723-4864. doi: 10.1007/s00348-016-2157-1. URL http://link.springer.com/10.1007/s00348-016-2157-1.

[75] Jan Schneiders. *Bridging PIV spatial and temporal resolution using governing equations and development of the coaxial volumetric velocimeter*. PhD thesis, 2017.

[76] Constantin Jux & Andrea Sciacchitano Schneiders, Jan F. G. , Fulvio Scarano. Coaxial Volumetric Velocimetry. *Measurement Science and Technology*, pages 0–24, 2018.

[77] Xue-ming Shao, Ding-yi Pan, Jian Deng, and Zhao-sheng Yu. Numerical Studies on the Propulsion and Wake Structures of Finite-Span Flapping Wings with Different Aspect Ratios. *Journal of Hydrodynamics*, 22(2):147–154, 2010. ISSN 1878-0342. doi: 10.1016/S1001-6058(09)60040-8. URL https://doi.org/10.1016/S1001-6058(09)60040-8.

[78] G. R. Spedding. A family of vortex wakes generated by a thrush nightingale in free flight in a wind tunnel over its entire natural range of flight speeds. *Journal of Experimental Biology*, 206(14):2313–2344, 2003. ISSN 0022-0949. doi: 10.1242/jeb.00423. URL http://jeb.biologists.org/cgi/doi/10.1242/jeb.00423.

[79] Alexander Spoelstra, Wouter Terra, and Andrea Sciacchitano. The Ring of Fire for in-Field Sport Aerodynamic. 2018. ISSN 2504-3900. doi: 10.3390/proceedings2060221.

[80] R. B. Srygley and A. L.R. Thomas. Unconventional lift-generating mechanisms in free-flying butterflies. *Nature*, 420(6916):660–664, 2002. ISSN 00280836. doi: 10.1038/nature01223.

[81] James R Usherwood and Charles P Ellington. The aerodynamics of revolving wings I. Model hawkmoth wings. *The Journal of experimental biology*, 205(Pt 11):1547–1564, 2002. ISSN 0022-0949.

[82] B Wieneke. Volume self-calibration for 3D particle image velocimetry. *Experiments in Fluids*, 45(4):549–556, 2008. ISSN 1432-1114. doi: 10.1007/s00348-008-0521-5. URL https://doi.org/10.1007/s00348-008-0521-5.

[83] Bernhard Wieneke. Iterative reconstruction of volumetric particle distribution. *Measurement Science and Technology*, 24(2):24008, 2013. ISSN 0957-0233. URL http://stacks.iop.org/0957-0233/24/i=2/a=024008.